Fermilab

FERMILAB-THESIS-1999-24

UNIVERSITY OF OKLAHOMA

GRADUATE COLLEGE

Measurement of the Angular Distribution of Electrons from W Boson Decays at DØ

A Dissertation

SUBMITTED TO THE GRADUATE FACULTY

In partial fulfillment of the requirements
for the degree of

Doctor of Philosophy

by

GEORG STEINBRÜCK

Norman, Oklahoma
1999

Measurement of the Angular Distribution of Electrons from W Boson Decays at DØ

A Dissertation APPROVED FOR THE
DEPARTMENT OF PHYSICS AND ASTRONOMY

BY

Phillip Gutierrez

George Kalbfleisch

Ron Kantowski

Sheena Murphy

James Hawthorne

Acknowledgments

This dissertation is a cumulative effort of many years of research conducted by a large number of people. I would like to thank everyone who has contributed to this work in some fashion. First and foremost, I want to thank my advisor, Professor Phil Gutierrez, for his continuous support and interest in this analysis and in my work as a graduate student at the University of Oklahoma. His expertise and guidance were greatly appreciated as he helped to get me started on many projects that needed the initial input by someone experienced in high energy physics.

At DØ, I would like to thank the members of the WZQCD group under the strong leadership of Cecilia Gerber for their continuous support. Without the help of Cecilia and Miguel Mostafa, who is working on the W p_T analysis, this analysis would not have been completed by now. Darien Wood deserves recognition for proposing this analysis and for answering many questions I had along the way.

Next I would like to thank all teachers who have helped me to understand physics and who are part of the reason I am here now. In chronological order these are my two high school teachers, Herr Krüger and Herr Lameck who taught math and physics to me and were an important factor in my decision to study physics. Then I would like to mention the professors at the University of Heidelberg from whom I learned basic and advanced physics. Specially Professor zu Putlitz (experimental physics), Professor Wegner (theoretical mechanics and statistical mechanics) and Professor Freitag (functions theory) deserve recognition for their well structured and interesting lectures. I would also like to thank my friends in Heidelberg: Markus, Georg, Jörg and Burkhard. We had a lot of fun together solving physics problems and just hanging out.

While the lectures in Germany were sometimes crowded and somewhat anony-

mous, I had the opportunity to experience a very different style of teaching at the University of Oklahoma. Small classes provided the opportunity for intense interaction between students and professors. All of the classes I took in Oklahoma were very inspiring. Thanks to Professors Jack Cohn (general relativity), Dave Kaplan (particle physics I), Ron Kantowski (quantum field theory), Phil Gutierrez (particle physics II), and Jeff Purinton (Aristotelean and Platonic philosophy). I also had the opportunity to get my first teaching experience as a teaching assistant under Professor George Kalbfleisch in a two semester electronics lab. This was an especially interesting task since I had to learn electronics while teaching it.

Maybe the greatest thanks should go to my family. My wife Trish has always supported my career as a physicist with all the difficulties it brings with it. Thanks also to my beautiful children Lili and Evi, who bring so much fun and excitement into our lives.

I am very grateful to my parents for their love and support over the years. You have always supported my dreams in life! Thanks to my brothers Andreas and Christian for our good childhood memories. I would also like to thank our friends Magdalena and Tom for lots of great dinners and conversations we enjoyed together. Finally, my in-laws deserve thanks for making me part of their loving family and introducing me to the United States.

To Trish,

Lili and Evi

Contents

List of Tables

List of Figures

Abstract of the Dissertation

Measurement of the Angular Distribution of Electrons from W Boson Decays at DØ

by

Georg Steinbrück

Doctor of Philosophy

in

Physics

The University of Oklahoma

1999

We present a measurement of the electron angular distribution parameter α_2 in $W \to e\nu$ events using data collected by the DØ detector during the 1994–1995 Tevatron run. We compare our results with next-to-leading order perturbative QCD, which predicts an angular distribution of $(1 \pm \alpha_1 \cos\theta^* + \alpha_2 \cos^2\theta^*)$, where θ^* is the angle between the charged lepton and the antiproton in the Collins-Soper frame. In the presence of QCD corrections, the parameters α_1 and α_2 become functions of p_T^W, the W boson transverse momentum. We present the first measurement of α_2 as a function of p_T^W. This measurement is of importance, because it provides a test of next-to-leading order QCD corrections which are a non-negligible contribution to the W mass measurement.

Chapter 1

The Standard Model of High Energy Physics

Our physical world is governed by four fundamental forces: Gravitation, the electromagnetic force, the weak force and the strong force. High energy physics is concerned with the last three of these forces; gravitation is so much weaker than the other three that it has no influence on subatomic processes and can be excluded from the following discussion. Moreover, a quantum theory of gravitation has yet to be developed. The proposed quantum particle of gravitation, the graviton, has never been detected. For mass limits on the graviton see [1].

What we call now the Standard Model of High Energy Physics consists of the three distinct quantum theories, Quantum Electrodynamics (QED), the theory of weak interactions, and Quantum Chromodynamics (QCD) as the theory of strong interactions. QED and the weak force have been combined into electroweak theory. The predictions made by electroweak calculations have been verified by experiments up to high levels of precision. QCD on the other hand has not successfully been unified with the theory of electroweak interactions for the following

reason: As we will discuss later in this chapter, electroweak theory starts from two broken symmetries represented by the groups $SU(2)_{left}$ and $U(1)_Y$ (Y stands for hypercharge). The process of symmetry breaking predicts the existence of the W bosons, the Z boson, and the photon. A linear combination of the above two symmetry groups, $U(1)_{EM}$ is found to be unbroken which corresponds to the photon. No larger symmetry group has been found that combines QCD with electroweak theory and makes correct predictions about the existence of gluons without introducing unwanted particles.

QCD calculations are in general more complicated than electroweak calculations due to the increasing strength of the strong force with distance which prohibits the use of perturbative techniques at low energies. Other techniques such as resummation have to be used in low energy QCD calculations to deal with singularities. Through resummation [2, 3], logarithmically divergent terms that are proportional to $\alpha_s \ln(Q^2/p_T^2)$ are avoided by reordering the perturbative series.

QCD is different from electroweak theory in that the carriers of the strong force, gluons and quarks, cannot exist isolated in nature. Gluons and quarks carry a quantum number associated with what is called color. Quarks can be green, red, or blue while antiquarks are antigreen, antired, or antiblue. The fact that color corresponds to the strong charge has two implications: There are three types of strong charge compared to only one for QED; and color has to be conserved at each vertex. If a red quark radiates a gluon and becomes a green quark, the difference has to be carried by the gluon, which then becomes red and antigreen. It is a prediction of QCD that all free particles in nature are colorless. This can be achieved in two ways: red+green+blue gives white, while a color and its anticolor also add up to white, which is the case in mesons. If a colored particle like a quark is emitted in an interaction, it immediately causes a spray of other particles to be created in order to shield its color. This process it called hadronization and the collimated spray of particles is called a hadronic jet.

1.1 Symmetry groups

An interesting feature of the three quantum field theories that make up the Standard Model of high energy physics is their relationship to symmetry groups: Each theory is based on an underlying local gauge symmetry. A gauge transformation is a transformation of the quantum fields [1] at hand that leaves the Lagrangian invariant. The Lagrangian operator is (in most cases) the difference between kinetic and potential energy of a system. A gauge transformation is called local if it varies with time and space as opposed to a global transformation that is the same everywhere. To illustrate what such a transformation looks like consider the simplest case, the Schrödinger equation for a charged particle in an electromagnetic field:

$$[(1/2m)(-i\boldsymbol{\nabla} - q\boldsymbol{A})^2 + qV]\psi = i\partial\psi/\partial t \tag{1.1}$$

where V is the electric potential, $\boldsymbol{A}$ is the vector potential, and ϕ is the electromagnetic field. The Schrödinger equation is gauge invariant under the combined transformation:

$$\begin{aligned} \boldsymbol{A} \rightarrow \boldsymbol{A}' &= \boldsymbol{A} + \boldsymbol{\nabla}\chi \\ V \rightarrow V' &= V - \partial\chi/\partial t \\ \phi \rightarrow \phi' &= \exp(iq\chi\phi)\cdot\phi \end{aligned} \tag{1.2}$$

Here, the theory is invariant under a gauge transformation with gauge field $\chi \equiv \chi(x,t)$ and consequently there is no unique solution to the Schrödinger equation but a set of solutions that differ only by a gauge field.

In the Standard Model, these gauge transformations are slightly more complicated but the principle is the same. While in the case of the Schrödinger equation the gauge transformation is represented by a single gauge factor, the

[1] Gauge transformations also exist in classical electrodynamics and are not specific to quantum fields.

transformations in the standard model are represented by matrices of various dimensions as seen below. The combined underlying symmetry group here is $SU(3)_C \bigotimes SU(2)_L \bigotimes U(1)_Y$. $SU(3)_C$ is the symmetry group of the strong interaction. Mathematically, it is represented by special unitary[2] 3×3 matrices. The 'C' indicates that the charge of strong interaction is called color. $SU(2)_L \bigotimes U(1)_Y$ is the combined symmetry group for electroweak interactions. $SU(2)_L$ stands for the left-handed character of electroweak interactions while $U(1)_Y$ indicates one dimensional unitary matrices associated with what is called the Yukawa term of the interaction which corresponds to the weak hypercharge [3]. Each of the three symmetry groups corresponds to a distinct kind of transformation. While the transformation represented by $U(1)$ matrices is a simple gauge transformation as described in the example above, the other two are represented by two and three dimensional matrices. It is important to note that it is not the case that $SU(2)_L$ is the transformation group behind weak interactions and $U(1)_Y$ the one describing electromagnetic interactions. Both the Z boson as mediator of the weak force, and the mediator of the electromagnetic force, the photon, are linear combinations of terms that come from both groups as described in section 1.4.

Why are these symmetry properties important? By demanding that the Lagrangian of a theory be symmetric under a local gauge transformation, additional terms have to be included in the Lagrangian. It is exactly these additional terms or gauge fields that then introduce particle interactions. The quanta of these fields, the gauge bosons, are the mediators of the respective forces.

[2]A unitary matrix has the property that its inverse is equal to it transpose conjugate, $U^{-1} = (U^T)^*$. A special unitary matrix is a unitary matrix with determinant + 1.

[3]Weak hypercharge is defined through the Gell-Mann-Nishijima relation $eQ = e(t_3 + y/2)$ where Q is the electric charge in units of e of the t_3 member of the weak isomultiplet. With this definition, the lepton doublets have $y = -1$, while the quark doublets have $y = 1/3$.

1.2 The particles

Before we describe the various kinds of interactions in more detail, we will give an overview of all elementary particles. In quantum field theory, the fields obey specific equations (the Dirac equation in the case of relativistic spin 1/2 particles like electrons). The solutions to these equations are interpreted as particles. Two types of particles can be distinguished on the basis of their statistical properties: Fermions are half-integer spin particles that obey the Pauli exclusion principle, which says that two particles with all quantum numbers identical cannot exist at the same time in the same place. Bosons, on the other hand, are integer spin particles, which implies that they are governed by Bose-Einstein statistics. For bosons the Pauli exclusion principle does not apply and many particles can occupy the same quantum state.

Elementary particles can further be divided into three classes: Quarks (spin 1/2), leptons (spin 1/2) , and gauge bosons (spin 1). Quarks and leptons can each be divided into three families of isospin doublets (See figure 1.1). The up-like quarks all have charge 2/3, while the down-like quarks have charge $-1/3$. The three charged leptons, the e,μ, and the τ have charge -1 while the neutrinos are electrically neutral. For each of the six quarks and six leptons, there exists an antiparticle with all quantum numbers negated.

$$\begin{pmatrix} u \\ d \end{pmatrix} \begin{pmatrix} c \\ s \end{pmatrix} \begin{pmatrix} t \\ b \end{pmatrix} \qquad \begin{pmatrix} e \\ \nu_e \end{pmatrix} \begin{pmatrix} \mu \\ \nu_\mu \end{pmatrix} \begin{pmatrix} \tau \\ \nu_\tau \end{pmatrix}$$

Figure 1.1: Quark and lepton doublets.

In addition to quarks and leptons, the standard model includes mediator particles of the various forces. In the case of the electromagnetic force, these are the gauge bosons: The W boson (W_+, W_-), the Z boson (Z_0), and the photon (γ).

QCD predicts eight spin-1 particles, the gluons. The Standard Model also predicts the existence of the Higgs boson which through a process call spontaneous symmetry breaking creates masses for the various particles. The Higgs boson is the only standard model particle which has not been observed yet. It is a major challenge for the next generation of collider experiments to find or exclude the Higgs boson. All standard model particles and their properties are summarized in table 1.1 [1].

1.3 Electroweak interactions

In the previous section it was briefly mentioned that electroweak theory is the direct product of two symmetry groups, $SU(2)_L$, and $U(1)_Y$. In the following section we will explain what consequences arise from the principle of gauge invariance in the case of electroweak interactions and how this relates to the carriers of this force, the gauge bosons. For a good description of electroweak theory as a gauge theory see [4].

Local gauge invariance of the electroweak Lagrangian under $SU(2)_L$, and $U(1)_Y$ transformations has to be insured. These two transformations can be written as:

$$\begin{pmatrix} \nu_e \\ e^- \end{pmatrix}_L \rightarrow \begin{pmatrix} \nu_e \\ e^- \end{pmatrix}'_L = \exp(i\boldsymbol{\alpha} \cdot \tau/2) \begin{pmatrix} \nu_e \\ e^- \end{pmatrix}_L \tag{1.3}$$

and

$$\Phi \rightarrow \Phi' = \exp(i\delta)\Phi \tag{1.4}$$

where Φ is the hypercharge field corresponding to $U(1)_Y$. Gauge invariance is introduced by replacing the regular partial derivative in the Dirac equation by generalized derivatives of the form:

$$\partial^\mu \rightarrow \hat{D}^\mu = \partial^\mu + ig\boldsymbol{\tau} \cdot \hat{W}^\mu + i(g'/2)y\hat{B}^\mu \tag{1.5}$$

Particle	Charge	Mass (GeV/c^2)	Interactions
		Leptons	
Electron (e)	-1	5.11×10^{-4}	EM, Weak
Electron Neutrino(ν_e)	0	$< 5.1 \times 10^{-9}$	Weak
Muon (μ)	-1	0.1057	EM, Weak
Muon Neutrino(ν_μ)	-1	$< 2.7 \times 10^{-4}$	Weak
Tau (τ)	-1	1.771	EM, Weak
Tau Neutrino(ν_τ)	-1	< 0.031	Weak
		Quarks	
Up(u)	$+2/3$	≈ 0.005	EM, Weak, Color
Down(d)	$-1/3$	≈ 0.010	EM, Weak, Color
Charm(c)	$2/3$	≈ 1.30	EM, Weak, Color
Strange(s)	$-1/3$	≈ 0.20	EM, Weak, Color
Top(t)	$2/3$	174.3 ± 5.1	EM, Weak, Color
Bottom(b)	$-1/3$	≈ 4.3	EM, Weak, Color
		Bosons	
Photon (γ)	0	0	EM
W boson ($W^\pm$)	±1	80.22	Weak (Charged)
Z boson (Z^0)	0	91.187	Weak (Neutral Current)
Gluon (G)	0	0	Color

Table 1.1: The fundamental particles of the Standard Model.

where g and g' are the weak charges of the $SU(2)_L$ and $U(1)_Y$ fields, $\hat{W}^\mu$ are the three $SU(2)_L$ gauge fields, and $\hat{B}^\mu$ is the hypercharge gauge field. $\boldsymbol{t}^{(t)}$ are the generators of weak isospin and y is the weak hypercharge. In the case of left-handed leptons we have $t = 1/2$ and $y = -1$ which leads to:

$$\partial^\mu \rightarrow \hat{D}^\mu = \partial^\mu + ig\frac{\boldsymbol{\tau} \cdot \hat{W}^\mu}{2} + \frac{ig'y}{2}\hat{B}^\mu \tag{1.6}$$

For right-handed leptons with $t = 0$ and $y = -2$ we get:

$$\partial^\mu \rightarrow \hat{D}^\mu = \partial^\mu - ig'y\hat{B}^\mu \tag{1.7}$$

indicating that the isospin field does not couple to right handed leptons. Inserting equation 1.6 into the Dirac equation

$$(i\ \partial\!\!\!/ - m)\psi = 0 \tag{1.8}$$

with $\not{a} = \gamma^\mu a_\mu$ and the Dirac matrices γ_μ leads to the following interaction term:

$$-ig[\bar{\hat{l}}_e(\boldsymbol{\tau}/2)\gamma_\mu \hat{l}_e] \cdot \hat{W}^\mu \tag{1.9}$$

where $\hat{l}$ and $\bar{\hat{l}}$ are the left-handed electron type doublet and its conjugate, respectively. To understand how equation 1.9 leads to a useful quantity in calculating an observable like a cross section, we introduce three $SU(2)_L$ polarization vectors ω^a:

$$\hat{\mathbf{W}}^\mu = \omega^a W^\mu \tag{1.10}$$

Then the interaction described by equation 1.9 is summarized by

$$(\frac{\boldsymbol{\tau}}{2}) \cdot \boldsymbol{\omega} \tag{1.11}$$

which can be rewritten as

$$\frac{1}{2^{1/2}}(\tau_+ \frac{\omega^1 - i\omega^2}{2^{1/2}} + \tau_- \frac{\omega^1 + i\omega^2}{2^{1/2}}) + \frac{\tau_3}{2}\omega^3 \tag{1.12}$$

where the linear combinations $\tau_\pm = (\tau^1 \pm \tau^2)/2$ have been introduced. $\tau_\pm$ are the raising and lowering operators for the isodoublets. τ_+ for example picks out transitions like $e^- \rightarrow \nu_e$ in which a W^+ is absorbed or a W^- emitted. The combination $\omega^- = (\frac{\omega^1 - i\omega^2}{2^{1/2}})$ creates a W^- or destroys a W^+. Finally, it follows that the $e \rightarrow \nu_e + W^-$ vertex is:

$$-\frac{ig}{2^{1/2}}\overline{u}(\nu)\gamma_\mu\frac{1-\gamma_5}{2}u(e) \tag{1.13}$$

where $\overline{u}(\nu)$ and $u(e)$ are the Dirac spinors associated with the electron and neutrino. This example shows how the principle of local gauge invariance introduces additional terms which appear in the Dirac equation. These terms are responsible for interactions which becomes transparent when written in terms of lowering and raising operators that reveal the interaction vertex. The vertex derived above contains the combination of γ-matrices, $(1-\gamma_5)$. This combination can be shown to pick out the left handed component of a spinor; since $\gamma_\mu\gamma_5$ transforms as an axial vector under Lorentz transformations and γ_μ transforms as a vector, these kind of interactions are called $(V-A)$ interactions. Right-handed couplings $(V+A)$ are absent from charged-current electroweak interactions. Since these interactions are a sum of equal amounts of vector and axial vector couplings, $(V-A)$ as opposed to $(V-\epsilon A)$, these interactions are maximal parity violating.

1.4 The Higgs Mechanism

In this section we will briefly illustrate how the gauge bosons obtain masses through spontaneous symmetry breaking or the Higgs mechanism. The fields for the gauge bosons will be the mass eigenstates of the theory. To start, consider the full electroweak Lagrangian:

$$\mathcal{L} = \mathcal{L}_g + \mathcal{L}_f + \mathcal{L}_s + \mathcal{L}_{f-s} \tag{1.14}$$

where the four parts are defined as follows:

$$\mathcal{L}_g = -\frac{1}{4}G_i^{\mu\nu}G_{\mu\nu}^i - \frac{1}{4}F^{\mu\nu}F_{\mu\nu} \tag{1.15}$$

which contains only gauge fields with:

$$G_{\mu\nu}^i = \partial_\mu W_\nu^i - \partial_\nu W_\mu^i - g\epsilon_{ijk}W_\mu^j W_\nu^k \tag{1.16}$$

and

$$F^{\mu\nu} = \partial_\mu B_\nu - \partial_\nu B_\mu \tag{1.17}$$

The next term contains the Fermion couplings:

$$\mathcal{L}_f = i\overline{u}_R\gamma^\mu D'_\mu u_R + i\overline{\chi}_L\gamma^\mu D_\mu \chi_L \tag{1.18}$$

where the generalized derivatives are:

$$D_\mu = \partial_\mu + i\frac{g'}{2}B_\mu y \tag{1.19}$$

and

$$D'_\mu = \partial_\mu + i\frac{g'}{2}B_\mu y + i\frac{g}{2}W_\mu \tag{1.20}$$

$\chi_L = \begin{pmatrix} u_\nu \\ u_l \end{pmatrix}$ is the chiral doublet for left handed leptons. The symmetry breaking occurs when a doublet of scalar fields $\begin{pmatrix} \Phi^+ \\ \Phi^0 \end{pmatrix}$ is added which leads to the following piece of the Lagrangian:

$$\mathcal{L}_s = (D^\mu\Phi)^\dagger(D_\mu\Phi) - \mu^2(\Phi^\dagger\Phi) - \lambda(\Phi^\dagger\Phi)^2 \tag{1.21}$$

In addition, we also mention the term that couples the scalar fields to the Fermions:

$$\mathcal{L}_{s-f} = -G[\overline{u}_R\Phi^\dagger\chi_L + \overline{\chi}_L\Phi u_R] \tag{1.22}$$

This is the term that generates the fermion masses. The fermions in the unbroken Lagrangian are chiral states (massless), it is the Higgs mechanism that gives them

mass. With the above definitions, we will now show how a particular choice for the vacuum expectation value for the scalar doublet will break both the $SU(2)_L$ and $U(1)_Y$ symmetries while leaving the $U(1)_{EM}$ symmetry intact. Choose

$$\langle \Phi_O \rangle = \begin{pmatrix} 0 \\ v/\sqrt{2} \end{pmatrix} \tag{1.23}$$

where v is the radial minimum of the Higgs potential. To say that the symmetry is broken is equivalent to the statement that

$$e^{i\alpha\mathcal{G}} \langle \Phi_O \rangle \neq \langle \Phi_O \rangle \tag{1.24}$$

which holds true for the generators $\mathcal{G}$ of the symmetry groups $SU(2)_L$ or $U(1)_Y$. For the linear combination that produces the generator for $U(1)_E M$,

$$\frac{1}{2}(\tau_3 + Y) \tag{1.25}$$

it can be shown that the symmetry is preserved.

What are the implications of this broken symmetry? To see how each broken symmetry corresponds to a massive particle, the field is expanded about the new vacuum with expansion parameter η which corresponds to the radial offset from the minimum of the Higgs field:

$$\Phi = \begin{pmatrix} 0 \\ (v+\eta)/\sqrt{2} \end{pmatrix} e^{\frac{i\boldsymbol{\xi}\cdot\boldsymbol{\tau}}{2v}} \tag{1.26}$$

With this expansion the relevant piece of the Lagrangian can be written as:

$$\mathcal{L}_s = \frac{1}{2}(\partial^\mu \eta)(\partial_\mu \eta) - \frac{1}{2} m_\eta^2 \eta^2 + \frac{1}{2} m_W^2 (|W_\mu^+|^2 + |W_\mu^-|^2) + \frac{1}{2} m_Z^2 |Z_\mu^0|^2 + interaction\ terms \tag{1.27}$$

where the masses come out to be:

$$m_W = \frac{gv}{2} = \left(\frac{\pi\alpha}{\sqrt{2}G_F}\right)^{1/2} \frac{1}{\sin\theta_W} \qquad m_Z = m_W \sqrt{\frac{g^2 + g'^2}{g^2}} = \frac{m_W}{\cos\theta_W} \tag{1.28}$$

where G_F is the Fermi constant, $\alpha = \frac{e^2}{4\pi} \approx (137^{-1})$ is the fine structure constant and θ_W is the Weinberg angle. The fields are

$$W_\mu^\pm = \frac{1}{\sqrt{2}}(W_\mu^1 \pm iW_\mu^2) \qquad\qquad Z_\mu^0 = \frac{-g'B_\mu + gW_\mu^3}{\sqrt{g^2 + g'^2}} \tag{1.29}$$

Finally an additional field that is orthogonal to the Z^0 field is defined as

$$A_\mu = \frac{gB_\mu + g'W_\mu^3}{\sqrt{g^2 + g'^2}} \tag{1.30}$$

$W_\mu^\pm$ and Z_μ^0 are the fields for the massive gauge bosons $W^\pm$, and Z, respectively. A_μ is the photon field which is absent from the piece of the Lagrangian that involves the Higgs field because the photon is massless. The term for the Z boson and the photon field show that they are linear combinations of the $SU(2)_L$ and the $U(1)_Y$ field. That is to say that the mass eigenstates are not the same as the eigenstates of the initial symmetry groups. Equation 1.28 shows that the masses of the Z boson and the W boson are related:

$$\cos\theta_W = \sqrt{\frac{g^2}{g^2 + g'^2}} = 0.226 \tag{1.31}$$

is called the Weinberg angle.

The scalar Lagrangian 1.27 contains one last term, $m_\eta^2\eta^2$. This corresponds to the massive scalar Higgs boson with mass

$$m_\eta = \sqrt{-2\mu^2} \tag{1.32}$$

The Higgs boson is the only standard model particle that has not been detected yet. It is a major task for the next generation collider experiments to find the Higgs boson.

1.5 QCD as a gauge theory

In this section we will describe the gauge theory behind Quantum Chromodynamics (QCD) and its basic differences with electroweak theory. The running strong

coupling constant will be discussed which is the reason that perturbation theory can be used at high energies in QCD. A good summary of QCD as a gauge theory and the Standard Model in general can be found in [5].

To motivate the introduction of the additional degree of freedom in QCD called color, consider that hadrons come in two and three quark bound-states called mesons and baryons, respectively. Mesons contain a quark and an antiquark while baryons contain three quarks. The following problem was noticed with certain baryons like the Δ^{++} and the Ω^- which have three identical quarks in the ground state: The mass spectra for baryons indicated that their wave functions have to be symmetrical under interchange of quarks, e.g. $q_a \leftrightarrow q_b$. But since baryons contain three spin 1/2 particles, they are Fermions and therefore Fermi statistics would be violated if the three quarks were identical. If an additional quantum number, arbitrarily called color, is introduced with the wave-function being totally anti-symmetric under exchange of two color indices, the problem is solved.

Another observation leading to three quark colors might be even more convincing since it involves a measurable quantity: Consider the ratio R of cross sections for the processes $e^+e^- \rightarrow \mathit{hadrons}$ and $e^+e^- \rightarrow \mu^+\mu^-$:

$$R = \frac{\sigma(e^+e^- \rightarrow \mathit{hadrons})}{\sigma(e^+e^- \rightarrow \mu^+\mu^-)} \tag{1.33}$$

In the parton model, this ratio is simply proportional to the sum of the individual quark couplings to the photon:

$$R = \sum_a e_a^2 \tag{1.34}$$

where a runs over all quark types that contribute. For five [4] quarks u, d, s, c, b with respective charges $\frac{2}{3}$, $-\frac{1}{3}$, $-\frac{1}{3}$, $-\frac{2}{3}$, $-\frac{1}{3}$ this yields $R = \frac{11}{9}$. If the sum is extended over three quark colors, however, the result is $R_{color} = \frac{11}{3}$ which is in fact preferred by experimental observation [6].

[4] Assuming that the measurement is performed below the threshold for $t\bar{t}$ production.

The symmetry group that describes transformations in color space is $SU(3)$. The choice of this group ensures that all hadron states are color-singlets, i.e. they are invariant under the action of the group.

To understand how the choice of $SU(3)_{color}$ leads to the desired properties of QCD, namely the existence of eight massless gluons that carry color, consider the free fermion Lagrangian for one quark field of a given flavor:

$$\mathcal{L} = \overline{\psi}(i\ \partial\!\!\!/ - m)\psi = \overline{\psi}^1(i\ \partial\!\!\!/ - m)\psi^1 + \overline{\psi}^2(i\ \partial\!\!\!/ - m)\psi^2 + \overline{\psi}^3(i\ \partial\!\!\!/ - m)\psi^3 \qquad (1.35)$$

where ψ is a column vector of which each colored component is a Dirac spinor, $\psi^T = (\psi^{1^T}, \psi^{2^T}, \psi^{3^T})$, and ψ belongs to the triplet representation of SU(3). A local gauge transformation can then be written as:

$$\mathcal{U} = e^{ig_c \sum_a \alpha_a(x) T_a} \qquad (1.36)$$

where the T_a's are the eight 3×3 matrix generators of the group, corresponding to eight gluons, and the $\alpha_a(x)$ are eight arbitrary real parameters that depend on space-time. Mathematically, the T_a's are traceless, hermitian matrices that satisfy the algebra $[T_a, T_b] = if_{abc}T_c$ where f is totally antisymmetric and real. With the above transformation, an infinitesimal gauge transformation of the fields and their derivatives can be written as :

$$\delta\psi = ig_c\alpha_a T^a\psi \qquad \delta\partial_\mu\psi = ig_c\alpha_a T^a\partial_\mu\psi + ig_c(\partial_\mu\alpha_a)T^a\psi \qquad (1.37)$$

where g_c is the color charge for QCD in analogy to the electric charge in QED. But the above Lagrangian is initially not gauge invariant since its variation is non-zero:

$$\delta\mathcal{L} = \overline{\psi}\{-g_c(\partial_\mu\alpha_a)T^a\gamma^\mu\}\psi \qquad (1.38)$$

Gauge invariance can be restored by introducing eight vector fields $A^b_\mu(x)$ transforming as

$$\delta A^c_\mu = \partial_\mu\alpha^c - f^{cab}\alpha^a A^b_\mu \qquad (1.39)$$

Now consider the lagrangian density

$$\mathcal{L} = \overline{\psi}(i(\partial_\mu - ig_c A^b_\mu(x)T^b)\gamma^\mu - m)\psi \qquad b = 1, ..., 8 \tag{1.40}$$

With the antisymmetric field-strength tensor

$$F^a_{\mu\nu} = \partial_\mu A^a_\nu - \partial_\nu A^a_\mu + g_c f^{abc} A^b_\mu A^c_\nu \tag{1.41}$$

the QCD Lagrangian, by analogy with the QED Lagrangian, finally becomes

$$\mathcal{L}_{QCD} = -\frac{1}{4}F^a_{\mu\nu}F^{a\mu\nu} + \overline{\psi}(i(\partial_\mu - igA^b_\mu T^b)\gamma^\mu - m)\psi \tag{1.42}$$

Note that gauge invariance excludes mass terms of the form $m_A^2 A^a_\mu A^{a\mu}$ so that the eight gauge bosons, the gluons, are massless and initially induce long range forces.

At this point it should be remarked why $SU(3)$ was chosen and not $U(3)$ which would also satisfy the antisymmetry of the baryonic wave function we started with. The additional degree of freedom in $U(3)$ would manifest itself in a ninth massless gauge boson that would be a color singlet. But this would induce long distance interactions which are absent from QCD.

Although both the photon and the gluons are massless gauge bosons, the forces they transmit are quite different in range. The reason for this lies in the fact that gluons carry color and belong to the triplet representation of $SU(3)$. Intuitively, the reason for the short range of the strong force can be understood in the following way: We have already mentioned that all particles that occur in nature are color singlets which results in the fact that quarks cannot exist isolated: This is called confinement. Color singlets, however, can only couple to color singlets. Since in SU(3), a color singlet gluon is absent, gluons cannot directly couple to hadrons. This is why the strong forces we observe are short-range despite the fact that massless particles lead to interactions of infinite range.

Another difference between QCD and QED is that there are gluon self-couplings: Three and four gluon vertices are possible while photons cannot directly couple

to each other. Mathematically, the self coupling terms come from the non-abelian nature of QCD which leads to terms linear in f^{abc} in equation 1.41 which then result in terms proportional to g_c and g_c^2 in the Lagrangian 1.42. An important consequence of these terms is the appearance of higher order loop diagrams that justify the application of perturbation theory in QCD.

However, as a consequence of the point-like structure of the fields in QCD (as in QED), "ultraviolet" divergences are encountered at high energies when higher order diagrams are calculated. These can be dealt with through a process called renormalization: All the parameters in the Lagrangian are redefined by fixing their values at some arbitrary point in momentum space. In terms of renormalized parameters, the perturbative series then assumes finite parameters. The matrix element for quark-quark scattering, for example, in the one loop approximation has then essentially the same form as the zeroth-order approximation.

$$|\mathcal{M}^{q_1 q_2 \to q_1' q_2'}|^2 \equiv \alpha_s(q^2)|\overline{u}(q_2')\gamma_\mu u(q_2)\frac{1}{q^2}\overline{u}(q_1')\gamma^\mu u(q_1)|^2 \tag{1.43}$$

where u is the quark-spinor and $\overline{u} = u^\dagger\gamma^0$. The divergent terms are swept into the coupling constant:

$$\alpha_s(q^2) = \frac{\alpha_s(\mu_0^2)}{1 + \frac{(11N_C - 2N_F)}{12\pi}\alpha_s(\mu_0^2)\ln\left(\frac{-q^2}{\mu_0^2}\right)} \tag{1.44}$$

where $N_C = 3$ is the number of colors and N_F is the number of active flavors. $\alpha_s(\mu_0^2)$ is the coupling constant at an arbitrary energy scale μ_0 and the new running coupling constant $\alpha_s(q^2)$ now depends on the momentum scale q^2 of the process. Since for QCD $(11N_C - 2N_F)$ is always positive, the coupling constant decreases with increasing energy and vanishes at asymptotically high energies or small distances: This is called asymptotic freedom and is the reason for the fact that at large energies as present at a modern hadron collider such as the Fermilab Tevatron (with center-of-mass energy 1.8 TeV) the interacting quarks can be treated as free particles.

Asymptotic freedom itself is not enough, however, to allow perturbative techniques to be applicable at large energies. A crucial feature of QCD is contained in the "factorization scheme" that states that the interaction between hadrons at large energies can be factorized into a non-perturbative piece that contains the information about the distribution of partons (quarks and gluons) inside the hadron and a perturbative piece which describes the interaction of essentially free partons at small distances. In Eq. 1.45, the non-pertubative factors are represented by $F_i(x_1, M)$ and $F_j(x_2, M)$, which are called parton distribution functions (PDF's). The perturbative piece of the observable is represented by $\hat{\sigma}_{ij}$.

$$d\sigma^{p\overline{p}\to X} = \sum_{i,j} \int dx_1 dx_2 F_i(x_1, M) F_j(x_2, M) \hat{\sigma}_{ij} \tag{1.45}$$

Cross section calculations performed in Monte Carlo programs are done by combining a specific parton distribution function with a theoretical calculation. In the case of this analysis a perturbative calculation is used for large transverse momenta of the W boson whereas the low transverse momentum region is described by a resummed calculation since perturbative techniques break down here.

Although strong interactions are, like electroweak theory, well described by a quantum field theory and its underlying symmetry group $SU(3)_{color}$, there are some important differences that complicate QCD calculations. Since the strong coupling constant is large at small energies, perturbative techniques break down here. Other methods like resummation techniques or lattice gauge theories have to be applied. These calculations are in general mathematically more difficult to perform and approximations have to be made which consequently make QCD calculations not as accurate as electroweak calculations, which have been verified by experiments to stunning levels of precision.

Ultimatively the goal of high energy physics is to combine all forces into one unifying theory. Theoretical models called Grand Unified Theories (GUT) exist that combine all three forces into one at a very large energy scale($\approx 10^{15}$ GeV).

Unfortunately, an energy this large can never be probed in a collider experiment.

Chapter 2

Angular Distribution Theory

An interesting feature of this analysis is that the underlying theoretical calculations are a combination of two theories: The theory of Electroweak Interactions and Quantum Chromodynamics (QCD). At tree-level in p-$\overline{p}$-collisions, a W boson is created through an s-channel process as shown in figure 2.1. This diagram dominates for events in which the W boson has very small transverse momentum. This purely electroweak process is determined by the $(V-A)$ character of electroweak interactions and leads to a rather simple angular dependence of the cross section:

$$\frac{d\sigma}{d(\cos\theta^*)} \propto (1 \pm \cos\theta^*)^2 \tag{2.1}$$

where $\cos\theta^*$ is the polar angle of the decay lepton in the W rest frame.

However, if the W boson is created with some transverse momentum, higher order effects become important. The transverse momentum is carried by a gluon- or quark jet and t-channel processes as in figure 2.2 contribute to the cross section. The additional gluon or quark alters the helicity-state of the W boson.

In general, a system with spins can be written in terms of nine helicity amplitudes for the various contributing processes as shown in equation 2.2. The functional form of the corresponding coefficients depends on the interaction theory

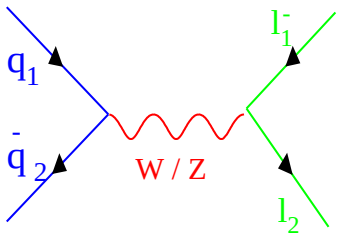

Figure 2.1: Tree level W production through s-channel process.

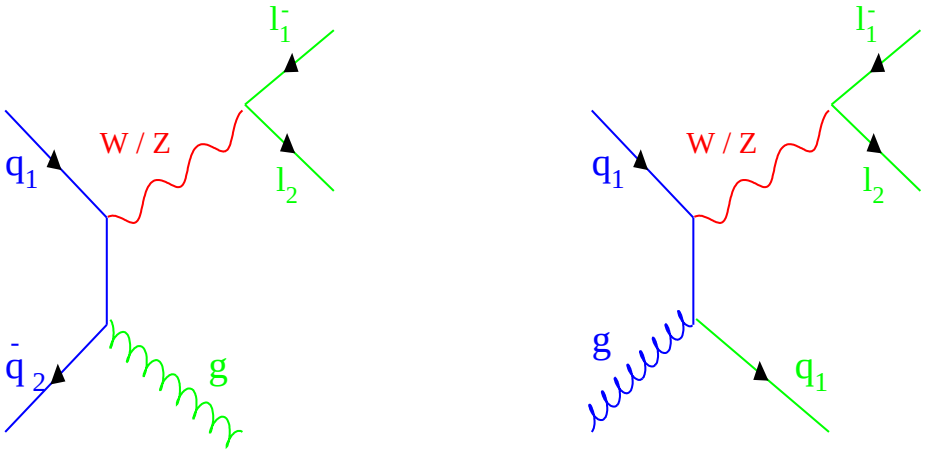

Figure 2.2: $\mathcal{O}(\alpha_S)$ W production diagrams.

being used, which in this case is a calculation to next-to-leading order in QCD [7].

$$\frac{d^3\sigma}{dq_T^2 dy d\Omega^*} = \sum_{\alpha\in\mathcal{M}} g_\alpha(\theta,\phi^*)\frac{3}{16\pi}\frac{d^\alpha\sigma}{dq_T^2 dy}, \qquad (2.2)$$
$$\mathcal{M} = \{U = L, L, T, I, P, A, 7, 8, 9, \}$$

where q_T is the transverse momentum of the W boson, y is its rapidity, $d\Omega^* = d\cos\theta^* d\phi^*$ is the solid angle of the decay electron in the Collins-Soper frame as described in appendix A. The coefficients are the following:

$$\begin{aligned}
g_{U+L}(\theta^*,\phi^*) &= 1+\cos^2\theta^* & g_A(\theta^*,\phi^*) &= 4\sqrt{2}\sin\theta^*\cos\phi^* \\
g_L(\theta^*,\phi^*) &= 1-3\cos^2\theta^* & g_7(\theta^*,\phi^*) &= 2\sin^2\theta^*\sin 2\phi^* \\
g_T(\theta^*,\phi^*) &= 2\sin^2\theta^*\cos 2\phi^* & g_8(\theta^*,\phi^*) &= 2\sqrt{2}\sin 2\theta^*\sin\phi^* \\
g_l(\theta^*,\phi^*) &= 2\sqrt{2}\sin 2\theta^*\cos\phi^* & g_9(\theta^*,\phi^*) &= 4\sqrt{2}\sin\theta^*\sin\phi^* \\
g_P(\theta^*,\phi^*) &= 2\cos\theta^*
\end{aligned} \qquad (2.3)$$

$d\sigma_{U+L}$ is the production cross section for unpolarized bosons while all other coefficients denote contributions for polarized bosons. Physically, these contributions correspond to couplings that all have distinct behaviors under parity transformations and time-reversal. $\sigma_{U+L,L,T,I,9}$ all receive contributions from the parity conserving part of the hadron tensor, $H_{\mu\nu}$, while the other four, $\sigma_{P,A,7,8}$ are parity-violating, which means that they change sign under parity transformations. However, the angular coefficients $g_{P,A,9}$ change sign, too. Consequently, the angular distributions involving $\sigma_{U+L,L,T,I,P,A}$ are parity conserving. Physically, this means that distributions such as charge asymmetry in W-boson events cannot discriminate between $(V-A)$ and $(V+A)$ couplings. The relevant coupling coefficients are:

$$\sigma_{U+L,L,T,I} \approx (v_l^2 + a_l^2)(v_q^2 + a_q^2) \qquad (2.4)$$

and

$$\sigma_{P,A} \approx v_l a_l v_q a_q \qquad (2.5)$$

where v_q (v_l) and a_q (a_l) and denote the vector and axial vector coupling of the gauge boson to the quark (lepton), respectively. Equation 2.4 corresponds to the parity-even coupling of the W-boson to the lepton current times the parity-even coupling to the quark current. On the other hand, σ_9 is proportional to the parity-odd coupling of the W-boson to the lepton current times the parity-even coupling to the quark current and $\sigma_{7,8}$ are proportional to the parity-even coupling of the W-boson to the lepton current times the parity-odd coupling to the quark current:

$$\sigma_9 \approx v_l a_l (v_q^2 + a_q^2) \tag{2.6}$$

and

$$\sigma_{7,8} \approx (v_l^2 + a_l^2) v_q a_q \tag{2.7}$$

Switching from $(V-A)$ theory to $(V+A)$ theory is then equivalent to reversing sign of these terms in equation 2.3. These angular distributions of the lepton momentum with respect to the W-boson production plane are not only P-odd but also T-odd.

The helicity cross sections $d\sigma^\alpha$ in equation 2.2 are obtained by convoluting the partonic cross section for partons with fractional momenta $p_1 = x_1 P_1$ and $p_2 = x_2 P_2$ with the respective parton distributions f:

$$\frac{d\sigma^\alpha}{dq_T^2 dy} = \sum_{a,b} \int dx_1 dx_2 f_a^{h_1}(x_1, M^2) f_b^{h_2}(x_2, M^2) \frac{s d\hat{\sigma}_{ab}^\alpha}{dt du}(p_1, p_2, \alpha_S(\mu^2)) \tag{2.8}$$

where x_1 and x_2 are the fractions of the proton and antiproton momenta, P_1 and P_2, partons 1 and 2 carry. h_1 and h_2 denote hadron 1 and 2, respectively. The sum is executed over quarks, antiquarks and gluons (a, $b = q$, $\overline{q}$, and G).

The two relevant scales in this calculation are the factorization scale M and the renormalization scale μ (see section 1.5). The factorization scale is introduced to absorb collinear initial state divergencies into the parton densities $f(x_i, M^2)$ [7]. In the numerical calculation quoted below, both scales are set to $M^2 = \mu^2 =$

$(m_W^2 + q_T^2)/2$. s, t,and u are the Mandelstam variables defined as follows:

$$\begin{aligned} s &= (p_1 + p_2)^2 \\ t &= (p_1 - q)^2 \\ u &= (p_2 - q)^2 \end{aligned} \tag{2.9}$$

The cross section can now be rewritten in terms of the azimuthal and polar angles in the Collins-Soper frame:

$$\begin{aligned} \frac{d\sigma}{dq_T^2 dy d\cos\theta^* d\phi^*} = \frac{3}{16\pi}\frac{d\sigma^{U+L}}{dq_T^2 dy}[&(1+\cos^2\theta^*) \\ &+\frac{1}{2}A_0(1-3\cos^2\theta^*) \\ &+A_1\sin 2\theta^*\cos\phi^* \\ &+\frac{1}{2}A_2\sin^2\theta^*\cos 2\phi^* \\ &+A_3\sin\theta^*\cos\phi^* \\ &+A_4\cos\theta^* \\ &+A_5\sin^2\theta^*\sin 2\phi^* \\ &+A_6\sin 2\theta^*\sin\phi^* \\ &+A_7\sin\theta^*\sin\phi^* \end{aligned} \tag{2.10}$$

Integrating over the azimuthal angle ϕ^* leads to the simple equation:

$$\frac{d\sigma}{dq_T^2 dy d\cos\theta^*} = C(1 + \alpha_1\cos\theta^* + \alpha_2\cos^2\theta^*) \tag{2.11}$$

where $C = \frac{3}{8}\frac{d\sigma^{U+L}}{dq_T^2 dy}[1 + \frac{A_0}{2}]$, $\alpha_1 = \frac{2A_4}{2+A_0}$, $\alpha_2 = \frac{2-3A_0}{2+A_0}$.

The angular coefficients α_1 and α_2 have been calculated to next-to-leading order $[\mathcal{O}(\alpha_S^2)]$ in perturbative QCD. Although they are functions of both the boson rapidity y and the transverse momentum of the W boson, the numerical results quoted in [7] were integrated over y. Figure 2.3 shows the angular parameters α_1 and α_2 as a function of the transverse momentum of the W boson, p_T^W. In this analysis, we measure α_2 as a function of p_T^W.

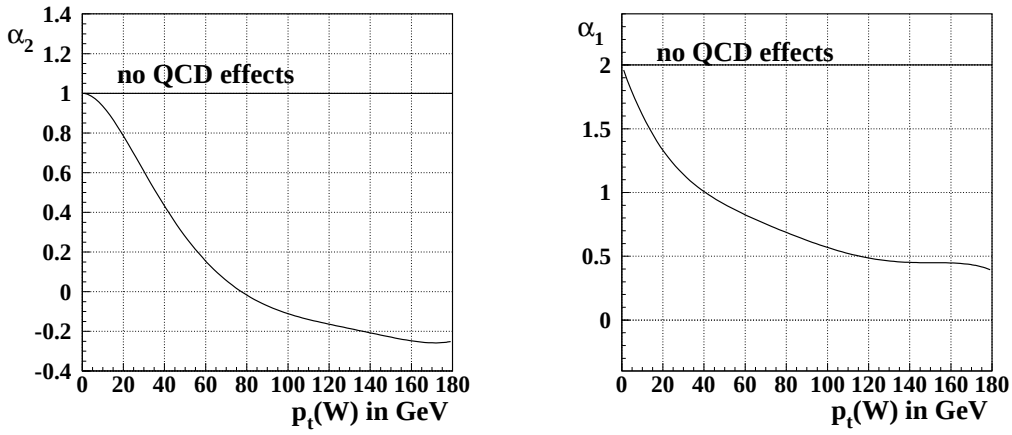

Figure 2.3: The angular parameters α_2 (left) and α_1 (right) as a function of p_T^W.

2.1 Some Intuition into the Angular Distribution

While the calculations discussed in the previous section contain all the information necessary to describe the angular distribution of the decay lepton in the W rest frame, they look a bit intimidating. It is good to gain some qualitative intuition of how the helicities of the particles involved determine the angular distribution. To attain this goal, we look at the simple case in which the W boson is produced with zero transverse momentum and the spins of all the particles involved are aligned with respect to each other as seen below.

Figure 2.4 illustrates how the spins of the created particles determine the angular distribution. The left plot represents the dominant mode for W^+ production, where a u-quark from the proton and a $\overline{d}$-quark from the antiproton interact. The spin of the quark is anti-collinear with the direction of the quark-momentum (left-handed quark), whereas the anti-quark's spin is collinear with its momentum (right-handed antiquark). Both spins are preferentially aligned in $-z$ direction. The outgoing positron is right-handed and will have its momentum preferentially pointing in $-z$ direction which is reflected in a cross section $\frac{d\sigma}{d\cos\theta^*} \sim (1-\cos\theta^*)^2$ where θ^* is the angle with respect to the $+z$-axis. This process can also occur with an $\overline{s}$-quark from the sea content of the antiproton.

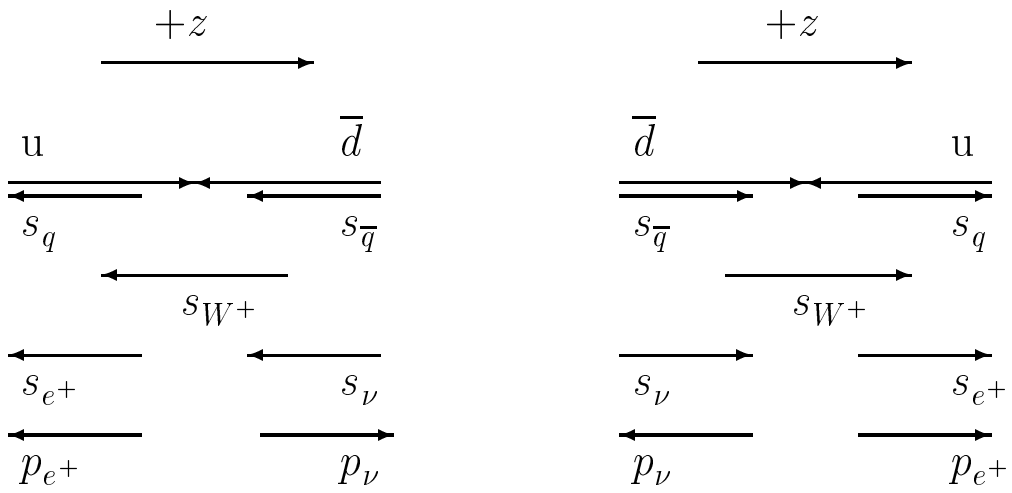

Figure 2.4: Illustration of spin states for W^+-production. u-quark from proton and $\overline{d}$-quark from antiproton (left) and u-quark from antiproton and $\overline{d}$-quark from proton (sea-sea interaction).

The interaction shown in the right plot can only occur if both quarks are from the sea-content of the proton and antiproton, respectively. The spins of both quarks now point in $+z$ direction which determines the direction of the spin of the positron ($+z$). That means that the positron will be preferentially emitted in $+z$ direction which is reflected in a cross section $\frac{d\sigma}{d\cos\theta^*} \sim (1+\cos\theta^*)^2$.

These plots are made for W^+ production. For W^- production the arguments can be made analogously, and the signs for the two cases are flipped, i.e. $(1+\cos\theta^*)^2$ for the dominant production mode and $(1-\cos\theta^*)^2$ for the mode that can only occur through sea-sea interactions. Table 2.1 summarizes the four combinations of W boson sign and polarization and the resulting angular distributions. Polarization is defined as the projection of the W spin on the positive z axis. Note, that the angular distribution can hence be written as:

$$\frac{d\sigma}{d\cos\theta^*} = C(1+S\cdot P(W)\cos\theta^*)^2 \tag{2.12}$$

where S is the sign and $P(W)$ the polarization of the W boson.

sign	polarization	
	- (dominant production mode)	+ (50 % of sea-sea interactions)
+	$(1-\cos\theta^*)^2$	$(1+\cos\theta^*)^2$
-	$(1+\cos\theta^*)^2$	$(1-\cos\theta^*)^2$

Table 2.1: Summary of angular distributions as a function of W boson sign and polarization.

Chapter 3

The Experiment

3.1 The Fermilab Tevatron

The Fermilab Tevatron (see figure 3.1), located at the Fermi National Accelerator Laboratory (FNAL) in Batavia, Illinois, is currently the highest energy particle accelerator in the world with a center-of-mass energy of 1.8 TeV in proton-antiproton collisions. Consequently, its physics capabilities are unique as seen for example in the discovery of the top quark in 1994 [9], which due to its large mass can currently not be produced anywhere else in the world. The high particle energies are reached in a chain of accelerators, all operating on the same principle: When a charged particle traverses an electric field, an acceleration takes place parallel to the electric field lines. An accelerator consists of a series of gaps with electric fields which form RF cavities. Electrically charged particles are accelerated along the gradients of the RF fields.

Two kinds of accelerators can be distinguished based on their geometric arrangement. In a linear accelerator, the gaps are arranged in a straight line. In a synchrotron, the gaps are situated along a circle or ellipse. High energies can be

obtained by reusing the gaps by letting the particles orbit as long as the desired energies are reached. Bending magnets synchronized with the beam are used to keep the particles in a circular (or elliptic) trajectory: Since the centripetal force of the orbiting particles is proportional to their energy, the magnetic fields used to keep the particles in a circular path have to be increased with beam energy. The Fermilab Tevatron is a synchrotron which made it possible to reach a large center-of-mass energy of $\sqrt{s} = 1.8$ TeV while keeping the size of the machine relatively compact.

A chain of accelerators is used to reach the final center-of-mass energy of 1.8 TeV. The various accelerators are:

- Preaccelerator
- Linac
- Booster
- Main Ring
- Antiproton Source
- Tevatron

In the following paragraph we will describe the role of each accelerator in the chain. For a good description of the Fermilab Collider complex see [10]. The production of protons starts with regular hydrogen gas from a pressurized bottle. H^- ions are produced by the addition of electrons [1]. An electrostatic **Cocroft-Walton accelerator** accelerates the ions to an energy of 750 keV. The ions are

[1] Negatively charged hydrogen ions are used since a plasma source to generate positive hydrogen ions requires a higher current and therefore a higher pulse time. The fast-pulsing negative ion source improves beam quality dramatically for the downstream accelerators because a smaller spread in particle creation time translates into higher precision in particle position downstream.

then injected into the **LINAC**, a 150 m long linear accelerator, resulting in 400 MeV protons. The electrons are then striped off by a carbon foil and the resulting protons are injected into the **Booster**, a 151 m diameter synchrotron operating at 15 Hz, which increases the energy to 8 GeV. The next stage is the **Main Ring**, a 1 km radius synchrotron, which uses about 1000 non-superconducting copper-coiled magnets. The protons are compressed into small bunches at a rate of $\approx 2 \times 10^{12}$ protons per bunch. Prior to the construction of the Tevatron, the Main Ring was the highest energy synchrotron in the world, accelerating particles to 400 GeV. Within the Tevatron complex, the Main Ring serves two purposes: It injects protons into the Tevatron and it directs a proton beam onto a target to produce antiprotons. Dependent on their destination, proton bunches are accelerated to two different energies in the Main Ring: Bunches that will be injected directly into the Tevatron get accelerated to 150 GeV. To generate antiprotons, on the other hand, 83 proton bunches are accelerated to 120 GeV and then injected into the **antiproton source**. Because antiprotons accumulate slowly, the Main Ring continues the antiproton generation process even while the Tevatron collides proton and antiproton beams.

Antiprotons are produced when the 120 GeV proton bunches are dumped onto a nickel/copper target (in the Target Hall). This way, about 20 antiprotons are produced per 1 million protons. The antiprotons are subsequently focused with a Lithium lens, and 8 GeV antiprotons are then selected by a magnetic field. Afterwards, the antiprotons are injected into the **Debuncher**, the first of two $\overline{p}$-storage rings. Radiofrequency and cooling techniques are used to equalize the antiproton energies. In the first step, called **debunching**, the protons are rotated in phase space to achieve a configuration with small momentum spread and large time spread from one with large momentum spread and small time spread. The momentum spread is further reduced by **stochastic cooling**, a process in which correction signals are applied to the beam via kicker electrodes after the trajec-

tories are measured and deviations are detected. Every 2.4 seconds, the resulting monochromatic $\overline{p}$-beam, consisting of 2×10^6 antiprotons/bunch is injected into a second storage ring, the **Accumulator**. More cooling is applied at this point and the density of the antiprotons is increased. Antiproton are kept in the storage ring until 4×10^{11} antiprotons are collected which takes 8 - 12 hours. They are then injected into the Main Ring, accelerated to 150 GeV and transferred to the **Tevatron** in opposite direction of the protons.

The Tevatron is located in the same tunnel as the Main Ring at a distance of 1m from it, except for the two interaction regions, where the distance is 19 feet at B0 (location of the CDF detector) and 89.2 inches at D0 (location of the DØ detector). The Tevatron is a synchrotron with super-conducting magnets operating at 4.6 K which allow for a magnetic field up to 3 Tesla. Six bunches of $\approx 10^{11}$ protons and six bunches of $\approx 5 \times 10^{10}$ antiprotons are ramped to 900 GeV at the same time and brought to collision in two places, at the CDF and the DØ detector while electrostatic separators keep the beams apart everywhere else. Over time, the density of the p- and $\overline{p}$-bunches decreases as a result of collisions of the beam with residual pipe gas, and beam-beam effects that blow up the beam size. The bunches have a limited life time of 12-18 hours, after which they have to be replaced. Continuous antiproton production allows a small down time between stores of about 2 hours.

At Fermilab, the beam can be used in two different modes of operation, namely in fixed target mode and colliding beam mode. In fixed target mode, a beam is directed on a target to produce a beam of secondary particles whose energy and type can be varied whereas in colliding beams mode, a proton and an antiproton beam are brought to collision. The advantage of the collider mode is that the center-of-mass energy is proportional to E and not $\sqrt{E}$ as in fixed target mode. The disadvantage is that both the center-of-mass energy and the particle type are fixed. In addition, the luminosity of a collider is lower than that of a fixed target

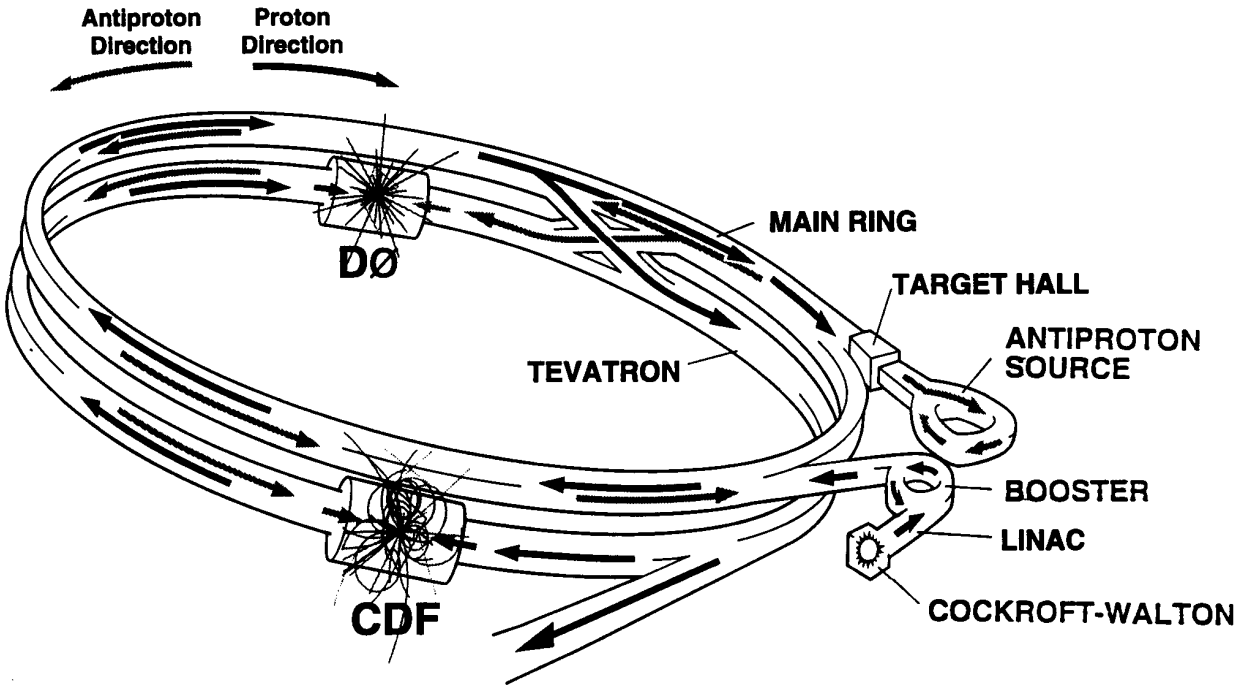

Figure 3.1: Fermilab Tevatron Collider complex.

experiment using a beam of similar intensity.

3.2 Overview of the Whole Detector

The DØ detector [11] is a large multipurpose detector which is specially optimized for the study of events with large transverse momentum, p_T, as present in a high energy colliding beam experiment.

The DØ detector consists of three subsystems with distinct purposes: The Central Detector whose main purpose is tracking of particles created in proton-antiproton collisions, the Calorimeter, which measures the energy of the particle-jets, and the Muon system which detects muons, that escape the other parts of the detector due to their long lifetime and high mass. For an overview of the DØ detector see figure 3.2. A conceptual difference between the innermost tracking

system and the calorimeter is that tracking should be done as undestructively as possible. That means that the incoming particles should only loose a small fraction of their energy in the tracking system.

The amount of energy a particle looses while traversing a certain material is characterized by a material constant, the radiation length X_0, according to:

$$\frac{dE}{E} = -\frac{dx}{X_0} \tag{3.1}$$

The radiation length is defined as the mean distance over which a high energy electron loses all but $1/e$ of its energy by bremsstrahlung. Physically, the radiation length is the mean free path for emitting bremsstrahlung. For charged particles, the radiation length depends on the Compton wavelength of the particle. Since muons are about 200 times heavier than electrons they don't suffer considerable Compton losses in the calorimeter. Electrons, on the other hand produce electromagnetic showers. Since in material, high energy photons produce electron-positron pairs, which in turn loose energy by bremsstrahlung, the above definition for radiation length applies to photons as well.

For electrons, radiation length may be parameterized in terms of atomic mass (A) and atomic number (Z) [12]:

$$X_0 \approx 180\frac{A}{Z^2} \tag{3.2}$$

For the tracking system, where particles should loose only a small fraction of their energy, materials with large radiation lengths are desirable. A calorimeter, on the other hand, should absorb as much of the particle energy as possible in order to allow for a precise energy measurement. The roughly $1/Z$ dependence of the radiation length in equation 3.2 justifies the use of depleted uranium for the electromagnetic section of the calorimeter (see section 3.4).

After these general remarks about the DØ detector and the processes by which high energy particles are detected, the subdetectors will be described in some detail in the following sections.

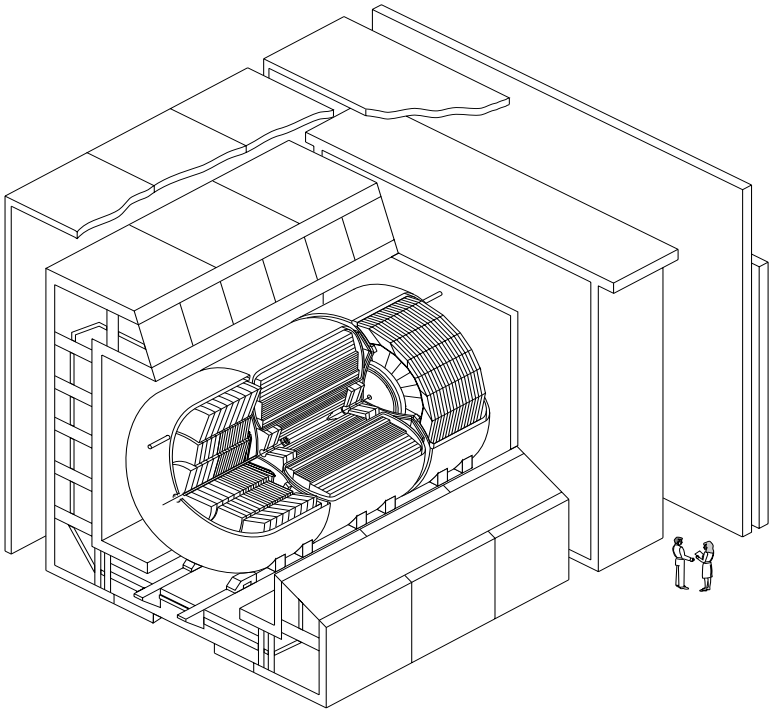

Figure 3.2: Overview of the DØ detector.

3.3 The Central Detector

The central detector [13, 11, 14] consists of four components (see figure 3.3): The innermost vertex drift chamber (VTX) is surrounded by the transition radiation detector (TRD) used for electron identification which is followed by the cylindrical central drift chamber (CDC). Two disk shaped forward drift chambers extend the forward coverage. The Central detector is contained in a cylinder of 75 cm radius and 270 cm length.

Drift chambers are gas filled volumes with a strong electric field applied between a thin anode wire and a cathode. Additional shaping electrodes are used to create a more homogeneous electric field. When a charged particle crosses the gas, it leaves a track of electron-ion pairs behind. The electrons start drifting towards the anode. In the vicinity of the thin anode wire, the electric field is very large, allowing the electrons to gain energy and create electron-hole pairs themselves

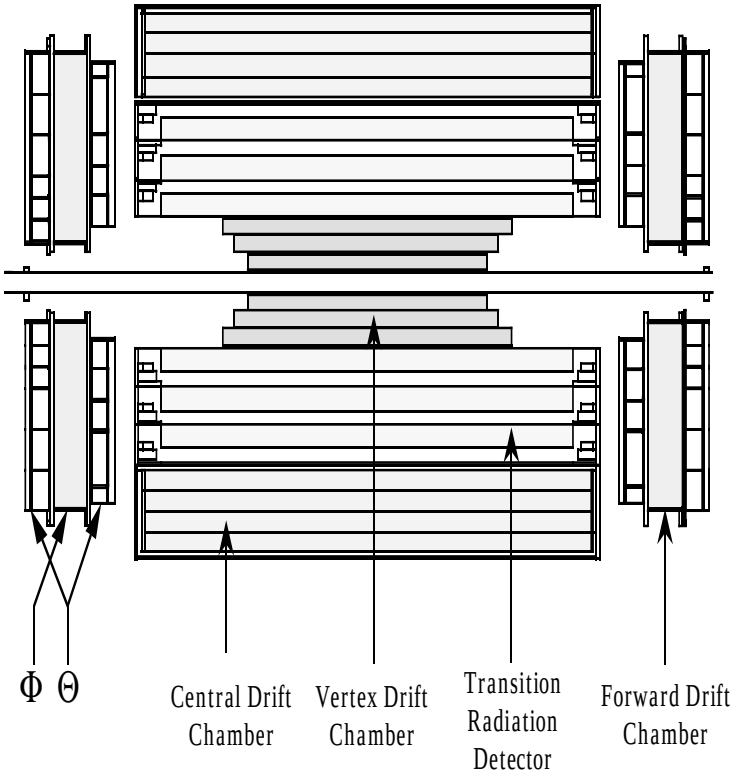

Figure 3.3: Side view of the central tracking system.

which results in a cascade of electrons moving towards the anode and creating a measurable current there. The ratio of the number of electrons collected at the anode and the number of initially created electron-hole pairs is called the gas gain with typical values ranging from 10^4 to 10^6. The fact that the electric field is nearly constant over a large area of the drift chamber except near the anode can be used to translate the drift time of the electrons to the anode into a distance measurement.

3.3.1 The Vertex Chamber

The vertex chamber (VTX) [11] is the innermost tracking chamber. It is used to accurately determine event vertex positions and to complement the other tracking chambers by identifying conversions which occur in the TRD. The VTX consists of three concentric cylinders which occupy the region 3.7 cm $\leq r \leq$ 16.2 cm. The

length of the inner cylinder is 97 cm while the two outer ones are 10 and 20 cm longer, respectively. The inner layer is divided into 16 cells while the outer ones consist of 32 cells. Each cell contains eight sense wires which are arranged in planes parallel to the direction of particles emerging from the interaction vertex. The coordinate of the wire hit and the drift time is used for $r-\phi$ information while a charge division technique along the resistive sense wires is used to resolve the hit position along z. This is done by reading out both ends of the wire and comparing the pulse heights.

The active medium (the gas ionized) is $CO_2(95\%)$-$C_2H_6(5\%)$ with a small amount (0.5%) of water added. The water helps stabilize the detector against radiation damage. [15, 16]. The sense wires operate at an electrical potential of +2.5 keV, which is above the threshold for electron cascades. Hence no information is derived from the areas under the pulses from the VTX.

The position resolution achieved with the VTX is about 60 μ in $r\phi$ and 1.5 cm in z [14].

3.3.2 The Transition Radiation Detector

The transition radiation detector (TRD) [11, 14], located between the VTX and the CDC, is used for electron identification. It makes use of the fact that relativistic particles radiate when they cross the boundary between two media of different dielectric coefficients. The energy of the emitted X-rays increases with Lorentz γ and is hence inversely proportional to the mass of the incident particle. Consequently, the measurement of the energy of the X-rays produced can be used to distinguish electrons from heavier particles such as pions.

The TRD consists of three layers, each containing a radiator (layered polypropylene foil) and an X-ray detection chamber (a proportional wire chamber, PWC). 393 18 μm thick polypropylene foils suspended in nitrogen gas are used in each radi-

ator section of the TRD. The radiators and the nitrogen are sealed by a Mylar window and surrounded by an array of sense wires suspended in a $Xenon-CH_4-C_2H_6$ mixture. For a cross sectional view of the first layer of the TRD see figure 3.4. An incident particle produces X-rays in the radiator stack, which convert in the gas of the PWC (91 % Xe, 7%CH_4, 2% CH_2), and charge drifts radially outwards and is amplified before reaching the sense wires.

The TRD provides an additional factor of about 50 [11] in rejection of isolated pions beyond that given by the calorimeter alone. For further information about the performance of the TRD see [17, 18].

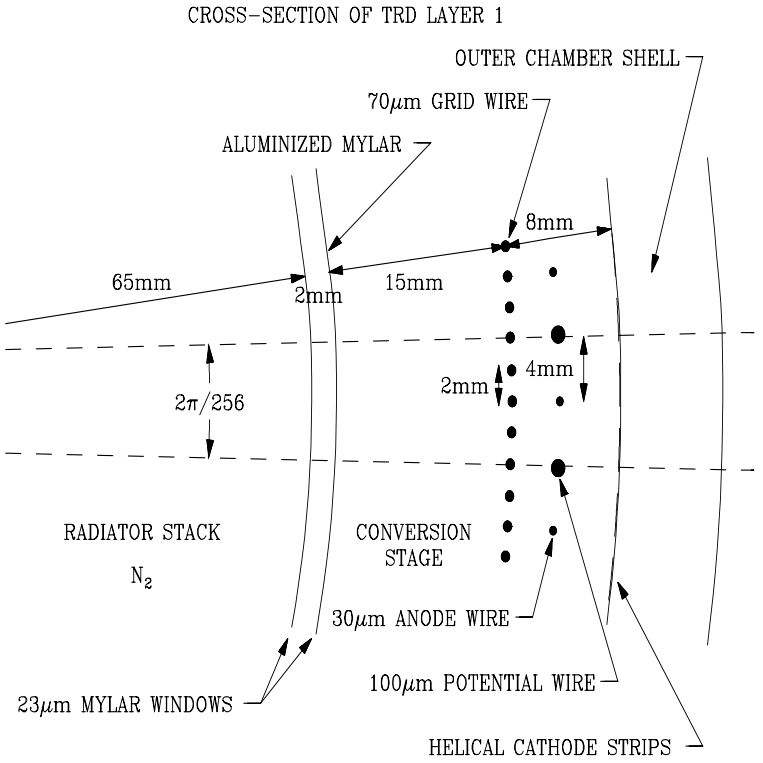

Figure 3.4: The Transition Radiation Detector.

3.3.3 The Central Drift Chamber

The central drift chamber (CDC) [19] is the outermost of the tracking detectors, providing coverage for tracks at large angles. It consists of four concentric cylindri-

cal layers, each 184 cm long, and covering 49.5 cm $< r <$ 74.5 cm. This results in an η coverage up to 1.2. For a cross sectional view of the CDC see figure 3.5. The CDC provides trajectory and ionization information for charged particles. Each layer consists of 32 modular azimuthal cells; each cell contains seven 30μm gold plated tungsten sense wires staggered $\pm 200\mu$ to remove left-right ambiguities. The hit position in $r - \phi$ is inferred from the coordinates of the hit wire and the drift time. Two additional delay lines are included in each cell to provide z-information: A charge avalanche generated by the incoming particle induces a charge on the inductive sense wire. The wire is then read out at both ends and the time difference between the two incoming pulses can be translated into a z-position. Alternate cells are offset by half of a cell to enhance pattern recognition. The resolution achieved in the CDC is 180 μ m in $r - \phi$ and 2.9 mm in z. More central drift chamber parameters can be found in table 3.1.

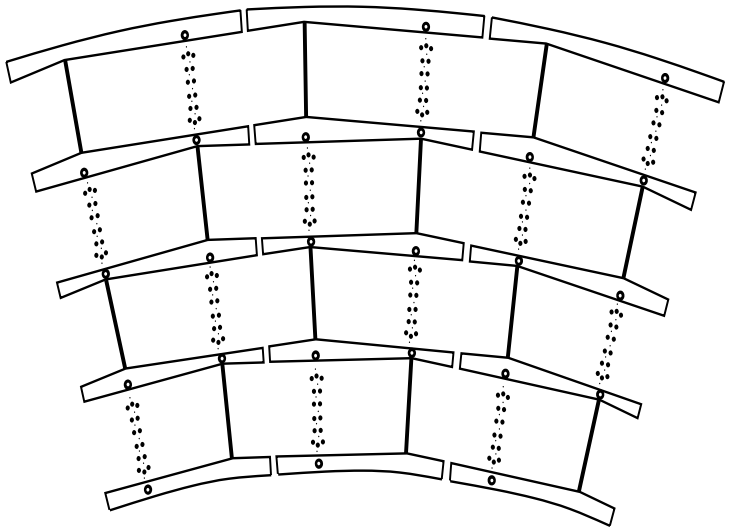

Figure 3.5: Cross sectional view of the CDC.

Table 3.1: Central Drift Chamber parameters.

Length of active volume	179.4 cm
Active radius	51.8–71.9 cm
Number of layers	4
Num. of cells/layer	32
Num. of sense wires	7/cell, 896 total
Num. of delay lines	2/cell, 256 total
Sense wire separation	6 mm with ± 200 μm stagger
Sense wire diameter	30 μm Au-plated W
Guard wire diameter	125 μm Au-plated CuBe
Sense wire potential	+1.5 kV
Gas mixture	Ar(93%)-CH_4(4%)-CO_2(3%)
Gas pressure	1 atm
Drift field	620 V/cm
Average drift velocity	34 μm/ns
Gas gain at sense wires	2.6×10^4

3.3.4 The Forward Drift Chambers

The Forward Drift Chamber (FDC) [20] extends the angular coverage to $\eta = 3.1$ or $\theta = 5^o$. Each of the two chambers located on both sides of the detector consists of three chambers (see figure 3.6): One Φ chamber with axial sense wires for a ϕ measurement and two Θ chambers for θ. The latter consist of four quadrants of which the top and the bottom one have sense wires parallel to the x-axis and the left and right one have wires parallel to the y-axis. The two Θ-chambers are rotated by 45^o with respect to each other. The Φ chambers consist of 36 azimuthal cells with 16 50 cm long axial sense wires each positioned parallel to the beampipe. Each $\Theta-$quadrant consists of six rectangular cells at increasing radii. Each cell has eight sense wires staggered again by $\pm$ 200 μm and one delay line. The resolution achieved by the FDC is 200 μm in ϕ and 300μm in θ. For a list of relevant FDC parameters see table 3.2.

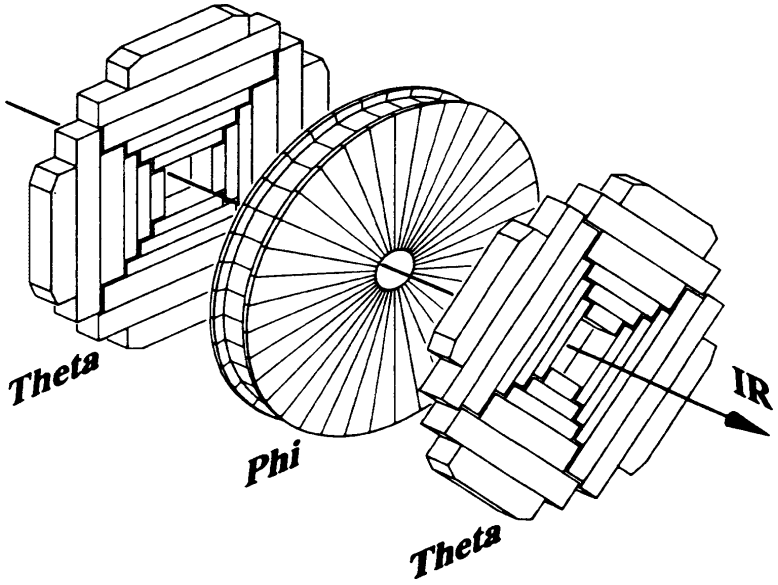

Figure 3.6: Layout of the FDC.

Table 3.2: Forward Drift Chamber parameters.

	Θ *modules*	Φ *modules*
Active z interval	104.8–111.2 cm	113.0–127.0 cm
	128.8–135.2 cm	
Active radius	11–62 cm	11–61.3 cm
Number of modules	4	2
Num. of cells/module	6×4 quadrants	32
Num. of sense wires/module	8/cell, 384 total	16/cell, 576 total
Num. of delay lines/module	1/cell, 48 total	—
Sense wire separation	8 mm with $\pm 200\mu$m stagger	
Sense wire diameter	30 μm NiCoSn	
Guard wire diameter	163 μm Au-plated Al	
Sense wire potential	+1.5 kV	
Gas mixture	Ar(93%)-CH_4(4%)-CO_2(3%)	
Gas pressure	1 atm	
Drift field	1.0 kV/cm	
Average drift velocity	37 μm/ns	40 μm/ns
Gas gain at sense wire	$2.3, 5.3 \times 10^4$	3.6×10^4

3.4 The Calorimeter

The precision calorimeter, as depicted in figure 3.7, is a strong point of the DØ experiment. In general, a calorimeter makes use of the fact that high energy elec-

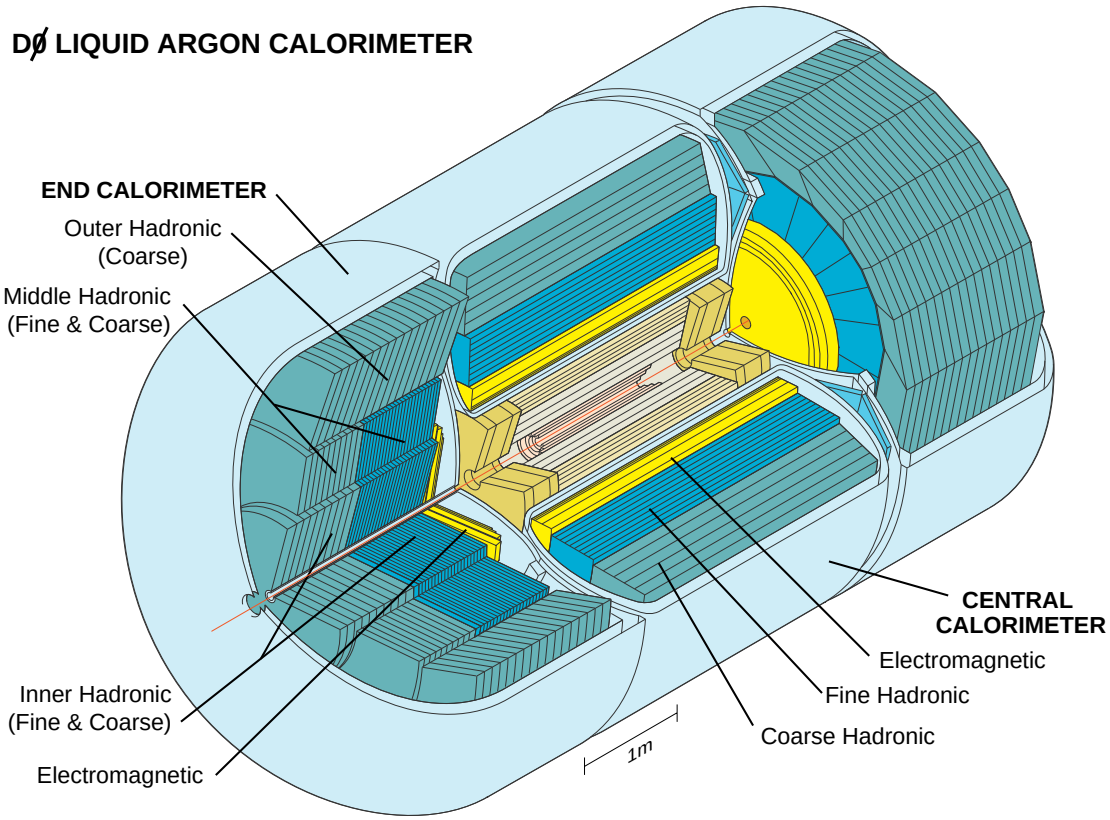

Figure 3.7: The DØ calorimeter.

trons interact with high-Z material through Bremsstrahlung. High energy photons, on the other hand, can produce electron-positron pairs in the Coulomb-field of a nucleus which can in turn interact through Bremsstrahlung. Consequently, an electron or photon can produce a cascade of photons and electron-positron pairs until the energy of each of these particles is low enough for other energy loss processes such as ionization to become dominant.

For optimal energy resolution of the calorimeter, it is desirable to use materials in which the particles loose a large fraction of their energy dE in a short path dx. For uranium, as used in the DØ detector, the radiation length X_0 is 3.2 mm which is rather small, allowing for compact detector design. Hadronic particles interact with matter differently: Here the main energy loss process is through inelastic collisions with atomic nuclei. These collisions result in new hadrons which can

then in turn scatter inelastically, resulting in hadronic showers. The size of these showers is characterized by the nuclear interaction length, λ, which is the mean free path between inelastic collisions. Since λ is 10.5 cm for uranium, which is much larger than the electromagnetic radiation length, hadronic showers are more extended in size than electromagnetic showers. While almost all electromagnetic showers will have lost their energy within the inner, electromagnetic sections of the calorimeter, hadron showers typically extend into the outer, hadronic sections.

It is important to note that there is no law of physics that forces the response of a calorimeter to be the same for hadronic and electromagnetic showers. In fact, the response to hadrons will in general be less than the response to electromagnetic objects since neutrinos and muons produced in pion and kaon decays escape the detector and since the energy spent to break up nuclei is invisible to the detector. It is highly desirable to build a calorimeter with equal response to electromagnetic and hadronic particles for the following reason: hadronic showers are not solely composed of hadronic particles, pions and eta-particles for example result in photons that induce electromagnetic showers. Since the electromagnetic content in a hadronic shower can undergo large fluctuations, any difference in response to hadronic and electromagnetic showers would degrade the energy resolution of the calorimeter. A calorimeter with equal response to hadronic and electromagnetic showers is called compensating.

In general, there are two different types of calorimeters: homogeneous calorimeters and sampling calorimeters. In a homogeneous calorimeter, the absorber material also functions as the active material. This could for example be a lead glass scintillator which traps a large fraction of the energy of the incoming particles and generates light pulses which can be read out through photomultipliers (PMTs). In a sampling calorimeter, on the other hand, layers of a dense inert material absorbing most of the energy are interleaved with layers of active material sensitive to radiation. The fraction of the incident energy that is actually detected in the ac-

tive material is called the sampling fraction. In the DØ detector depleted uranium is used as the absorber material with the advantage that its density allows for a compact calorimeter. Copper and stainless steel are used in addition in the outer regions[2]. The ionization medium is liquid argon which requires cryogenic cooling of the calorimeter.

The resolution of a calorimeter is limited by the statistical nature of the energy loss processes in matter and scales like $\frac{1}{\sqrt{N_{ion}}}$ where N_{ion} is the number of ions liberated. Since N_{ion} is proportional to the incident energy, one expects the resolution to be roughly proportional to $\frac{1}{\sqrt{E}}$. This ideally achievable resolution gets further degraded by noise effects, instabilities in the run conditions of the detector like temperature fluctuations, natural radioactivity from the depleted uranium and energy leakage out of the calorimeter. For a good discussion on calorimetry in high energy physics see [23].

3.4.1 Calorimeter Design

Since the DØ calorimeter is a sampling calorimeter with liquid argon as the active medium, a cryostat had to be used to contain the argon and keep it cool. To retain access to the central tracking system, a modular layout was chosen for the calorimeter as shown in figure 3.7. It consists of one Central Cryostat (CC), covering the region $|\eta| \leq 1.2$, two Endcap Cryostats (EC's) extending the coverage to $|\eta| \approx 4$, and the Inter-Cryostat Detector (ICD), covering the region between CC

[2]Copper and stainless steel are much less expensive than depleted uranium. By the time showers reach the outer regions of the calorimeter, they have lost most of their energy and only showers that are in the tail of the energy distribution make it this far. To catch these tails, copper or stainless steel are well suited materials [21]. Steel and copper work equally well for the outer regions; stainless steel was used for the parts of the calorimeter that were built by Russian collaborators who had larger amounts of steel available at that time [22].

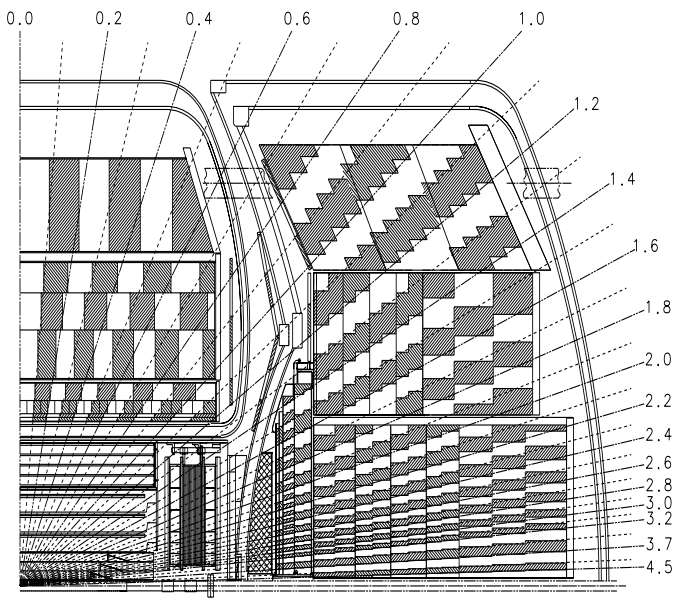

Figure 3.8: One-quarter η-view of the calorimeter and the Central detector.

and EC modules.

The DØ calorimeter is finely segmented in the transverse and longitudinal shower directions. The size and construction of the calorimeter cells varies between layers to account for the specifics of shower profiles: The electromagnetic (EM) section uses 2.3 mm thin uranium-238 absorber plates; the fine hadronic (FH) section also has 2.3 mm uranium plates while the course hadronic (CH) section uses 46.5 mm thick copper (CC) or stainless steel plates (EC). Each calorimeter cell consists of alternating absorber plates and signal readout boards as seen in figure 3.9. The 2.3 mm gap between absorber plate and pad is filled with liquid argon. The signal boards consist of a copper pad with two 0.5 mm thick G-10 sheets laminated on each side whose outer surfaces are coated with highly resistive epoxy. An electric field is established by grounding the absorber plates while applying 2 - 2.5 kV to the resistive epoxy surfaces. When an incoming particle hits

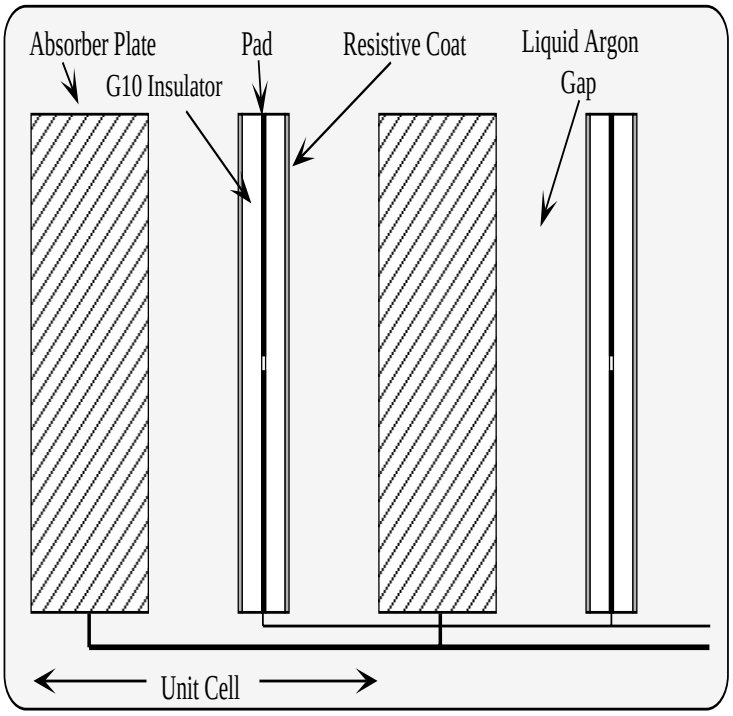

Figure 3.9: Two unit cells of the DØ calorimeter.

an absorber plate, it showers into many particles ionizing the liquid argon in the adjacent gap. Liberated electrons drift to the signal board with typical drift times of around 450 ns, inducing a signal on the copper pad. Signals from several signal boards in the same $\eta - \phi$ region are ganged together to form a readout cell.

The patterns and sizes of the readout cells are determined by taking into account typical sizes of showers: The transverse dimensions of electromagnetic showers are about 1-2 cm whereas for hadronic showers they are about 10 cm. Longitudinal subdivision within the EM, FH, and CH sections is useful since the longitudinal shower profiles help distinguish electrons and hadrons.

The overall pattern is pseudo-projective as shown in figure 3.8: The centers of the calorimeter cells lie on lines that project back to the center of the detector, whereas the cell boundaries are perpendicular to the absorber plates.

3.4.2 Central Calorimeter

The Central Calorimeter (CC) consists of three concentric cylinders parallel to the beam axis which cover 75 cm $\leq r \leq$ 222 cm from the nominal beam axis. The angular coverage is $35^\circ \leq \theta \leq 145^\circ$ which corresponds to $|\eta| \leq$1.2. The inner shell consists of 32 EM modules thick enough to contain most electromagnetic showers (20.5 total radiation lengths at $\eta = 0$ corresponds to an energy-fraction of 10^{-9} that escapes the EM modules). The middle shell consists of 16 FH modules to measure showers of hadronic particles while the outer shell, with 16 CH modules, measures any leakage out of the FH layer while minimizing punchthrough, the energy flow out of the calorimeter into the muon system.

The EM modules consist of 21 radial cells (cells along the radial direction of the calorimeter) in four readout layers called EM1-EM4. Each cell contains a 3 mm depleted uranium absorber plate, a 2.3 mm liquid argon gap and a signal board as described above, leading to a sampling fraction of 12.9 %.

The FH modules consist of 50 radial cells in three readout layers FH1-FH3. Each cell has a 6 mm uranium-niobium alloy[3] (U-Nb) absorber plate, a 2.3 mm liquid argon gap, and a signal board as described above, which amounts to a sampling fraction of 6.9 %.

Each CH module contains nine radial cells, which are ganged into just one readout layer. A sampling fraction of 1.7 % is achieved using 4.75 cm thick copper absorber plates with 2.3 mm liquid argon gaps. Figure 3.10 shows the layout of calorimeter towers.

The transverse segmentation of the calorimeter is 0.1×0.1 in $\eta \times \phi$ except for EM3 where it is reduced to 0.05×0.05 to optimize the separation between electro-

[3]Niobium is added for better mechanical strength. It makes the uranium harder and more difficult to machine, however. This is the reason it was not used in the electromagnetic sections of the calorimeter where the dimensional tolerances are smaller.

magnetic and hadronic showers in the layer where most EM showers deposit the bulk of their energy. To avoid cracks, each concentric shell is rotated azimutically with respect to the neighboring ones. A list of Central Calorimeter parameters is given in table 3.3

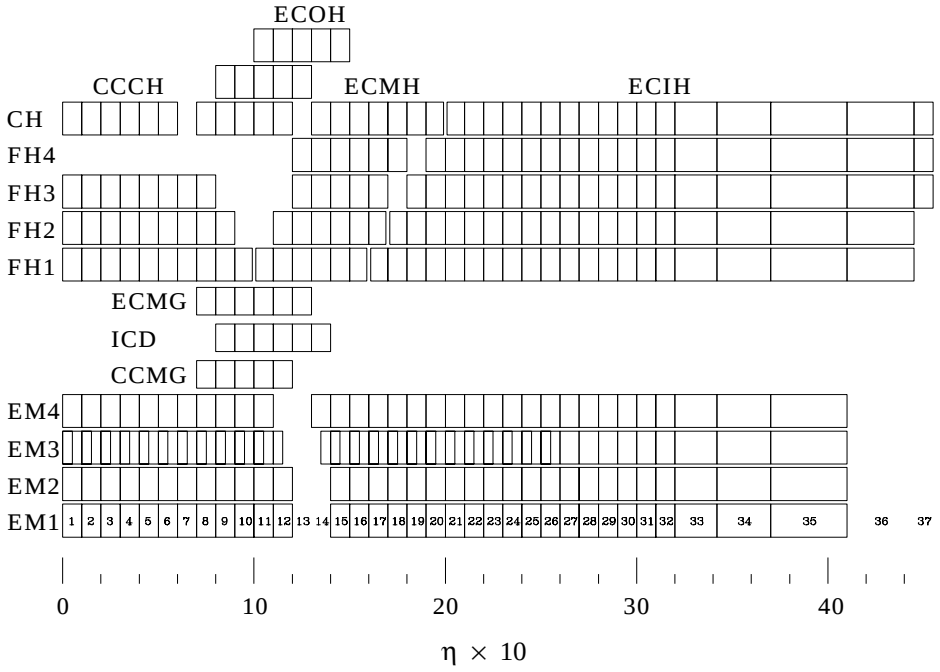

Figure 3.10: Segmentation of the DØ calorimeter towers.

3.4.3 Endcap Calorimeter

The Endcap Calorimeters (EC's) cover the forward regions $2^\circ \leq \theta \leq 30^\circ$ and $150^\circ \leq \theta \leq 178^\circ$ ($1.3 \leq |\eta| \leq 4$). Each EC cryostat is divided into four sections, Electromagnetic (EM), Inner Hadronic (IH), Middle Hadronic (MH), and Outer Hadronic (OH) (see figure 3.7).

The EM section (EMEC) consists of disk shaped modules centered on the nominal beam line with an inner radius of 5.7 cm and an outer radius of 84-104 cm which results in an angular coverage of $3^o \leq \theta \leq 27^o$. Eighteen radial

Table 3.3: Central Calorimeter parameters.

CC module type	EM	FH	CH
Rapidity coverage	$\pm$ 1.2	$\pm$ 1.0	$\pm$ 0.6
Number of modules	32	16	16
Absorber[a]	Uranium	Uranium	Copper
Absorber thickness [cm]	0.3	0.6	4.65
Liquid argon gap [cm]	0.23	0.23	0.23
Number of cells per module	21	50	9
Longitudinal depth	20.5 $X_\circ$	3.24 $\lambda_\circ$	2.93 $\lambda_\circ$
Number of readout layers	4	3	1
Cells per readout layer	$2, 2, 7, 10$	$21, 16, 13$	9
Total radiation lengths	20.5	96.0	32.9
Radiation length per cell	0.975	1.92	3.29
Total absorption lengths (λ)	0.76	3.2	3.2
Absorption length per cell	0.036	0.0645	0.317
Sampling fraction [%]	11.79	6.79	1.45
Segmentation $(\phi \times \eta)$[b]	0.1×0.1	0.1×0.1	0.1×0.1
Total number of readout cells	$10,368$	3456	768

[a]Uranium is depleted and FH absorbers contain 1.7% Niobium alloy
[b]EM3 layer has 0.05×0.05

cells containing 4 mm thick depleted uranium absorber plates are grouped into four readout layers, EM1-EM4. The transverse segmentation is mostly 0.1×0.1 in $\eta \times \phi$ with the following exceptions: In the region $|\eta| \geq 3.2$, where the pad size would be to small, the segmentation is 0.2×0.2. In EM3, the segmentation is 0.05×0.05 for $|\eta| \leq 2.7$, 0.1×0.1 for $|\eta| \leq 3.2$, and 0.2×0.2 for $|\eta| \geq 3.2$.

The Inner Hadronic layer (IH) is located behind the ECEM. It is cylindrically shaped with an inner radius of 3.92 cm and an outer radius of 86.4 cm. Longitudinally, it is divided into a fine hadronic (IFH) and a course hadronic layer (ICH). The IFH consists of 16 cell with 6 mm thick semi-circular uranium plates arranged in four readout layers FH1-FH4. To avoid cracks, each alternate plate is rotated by 90° in ϕ.

The ICH consists of a single readout layer comprising 13 cells with 46.5 mm thick stainless steel absorber plates. The segmentation on the IH segment matches

that of the ECEM: $\Delta\eta \times \Delta\phi = 0.1 \times 0.1$ for $|\eta| \leq 3.2$ and 0.2×0.2 otherwise. Beyond the ECEM coverage, i.e. for $|\eta| \geq 3.8$, it is 0.4×0.2.

Surrounding the inner core of EM and IH modules is the middle hadronic ring (MH), consisting of 16 wedge shaped modules with 33 cm $\leq r \leq$ 152 cm. Like the IH, the MH modules are divided longitudinally into fine hadronic (MFH) and course hadronic (MCH) sections. The MFH consists of 60 radial cells in four readout layers FH1-FH4 containing 6 mm thick uranium-niobium alloy absorber plates. The MCH consists of a single readout layer with 14 cells. The transverse segmentation of the MH is exactly identical to that of the IH.

The Outer Hadronic layer (OH) surrounds the MH with an inner radius of 162 cm and outer radius of 226 cm. The 16 OH modules form a parallelogram with an inner face at an angle of 27.4° with respect to the $x - y$ plane. Each OH module consists of 25 radial cells grouped into three readout layers. 46.5 mm stainless steel absorber plates are used here. For all relevant EC parameters see table 3.4

3.4.4 Intercryostat Detectors and Massless Gaps

Figure 3.8 shows that particles that travel through the crossover region between the CC and EC cryostats have to traverse mainly support structure like cryostat walls and end support plates before reaching the calorimeter modules. Two additional detectors have been installed to make measurements that attempt to correct for the energy loss in this dead material: The massless gap detector (MG) is an additional layer of liquid argon sampling on the face of each MH and OH module in the EC and each end of the FH modules in the CC. The massless gaps present no significant absorber material but they sample the shower energy before and after the dead material between cryostats which means they measure the energy lost therein. The MGs cover the pseudorapidity region between 0.7 and 1.2 and are segmented 0.1×0.1 in $\eta \times \phi$ space.

Table 3.4: Endcap Calorimeter parameters.

EC module type	EM	IFH	ICH	MFH	MCH	OH
Rapidity coverage	1.3-4.1	1.6-4.5	2.0-4.5	1.0-1.7	1.3-2.0	0.7-1.4
Num. of modules/cryostat	1	1	1	16	16	16
Absorber[a]	U	U	SS[b]	U	SS	SS
Absorber thickness [cm]	0.4	0.6	4.6	0.6	4.6	4.6
Liquid argon gap [cm]	0.23	0.21	0.21	0.22	0.22	0.22
Num. of cells per module	18	64	12	60	12	24
Longitudinal depth	$20.5X_\circ$	$4.4\lambda_\circ$	$4.1\lambda_\circ$	$3.6\lambda_\circ$	$4.4\lambda_\circ$	$4.4\lambda_\circ$
Num. of readout layers	4	4	1	4	1	3
Cells/Readout layer	$2, 2, 6, 8$	16	12	15	12	8
Tot. radiation lengths	20.5	121.8	32.8	115.5	37.9	65.1
Tot. absorption length (λ)	0.95	4.9	3.6	4.0	4.1	7.0
Sampling fraction [%]	11.9	5.7	1.5	6.7	1.6	1.6
$\Delta\phi$ segmentation[c]	0.1	0.1	0.1	0.1	0.1	0.1
$\Delta\eta$ segmentation[d]	0.1	0.1	0.1	0.1	0.1	0.1
Readout channels[e]	14976	8576	1856	2944	768	1784

[a]Uranium is depleted and FH (IFH and MFH) absorbers contain 1.7% Niobium alloy for strength

[b]Stainless Steel

[c]EM3 layer has $\Delta\phi \times \Delta\eta = 0.05 \times 0.05$ for $|\eta| < 2.6$

[d]For $|\eta| > 3.2, \Delta\phi = 0.2$ $\Delta\eta \approx 0.2$

[e]MCH and OH are summed together at $|\eta| = 1.4$

The second type of compensating detector is the Intercryostat detector (ICD). It consists of two arrays of 384 scintillation counter tiles mounted on the front surface of each EC cryostat. The size of the tiles is matched to that of the liquid argon calorimeter cells. Grooves cut into each scintillating tile guide wavelength-shifting optic fibers that channel the scintillation photons to photomultiplier tubes (PMT's) for readout. The tile arrays cover the entire rapidity range from 0.8 to 1.4. Together the ICD and the massless gaps provide a good approximation to the standard DØ sampling of EM showers.

3.4.5 Calorimeter Readout

The readout of the calorimeter signals is done in three steps: The 450 nm wide pulses are routed through four ports in the cryostats to charge sensitive preamplifiers mounted on top of the cryostat modules. Subsequently the pulses are input to baseline subtracter modules (BLS) located in the platform underneath the detector which perform analog signal shaping and splitting of the signal into two. The first signal serves as input to the calorimeter Level-1 trigger while the second one is used for data readout. Sampling occurs just before each beam crossing and 2.2μs later so that the difference between the two readings is a dc voltage that is proportional to the collected charge. Finally, if an event is accepted by the Level-1 trigger, the difference is sent to analog-to-digital converters (ADC's) that digitize and zero-suppress the signals before being sent to the Level-2 trigger.

3.4.6 Calorimeter Performance

To utilize the DØ calorimeter to its fullest potential it was necessary to study its performance extensively so that measured pulses read out by the calorimeter electronics can be related to physical energies. Two kinds of studies that complement each other were done: testbeam studies [8] with a scaled down version of a cryostat and studies with cosmic ray muons [24] were performed. The calorimeter response was found to be linear up to 0.5% in a large energy range from 10 GeV to 150 GeV. The energy resolution of a calorimeter can be parameterized as:

$$\frac{\delta E}{E} = C \oplus \frac{S}{\sqrt{E}} \oplus \frac{N}{E} \tag{3.3}$$

The constant term C includes calibration errors and affects the resolution function as a whole. The noise term N is due to residual radioactivity from the uranium in the calorimeter and is only important at low energies. The sampling term S is due to sampling fluctuations and is the dominant term. The following values for

the three contributions were measured for electrons:

$$C = 0.003 \pm 0.002 \qquad S = 0.157 \pm 0.005 \text{ GeV}^{\frac{1}{2}} \qquad \text{N} \approx 0.140 \text{ GeV} \tag{3.4}$$

while for pions they were:

$$C = 0.032 \pm 0.004 \qquad S = 0.41 \pm 0.04 \text{ GeV}^{\frac{1}{2}} \qquad \text{N} \approx 1.28 \text{ GeV} \tag{3.5}$$

The parameters measured for electrons reflect the resolution of the electromagnetic calorimeter. For the hadronic calorimeter, the actual resolution depends on the particle content of the hadronic showers and will in most cases be worse than the value measured for pions. Moreover, even two hadronic jets with with same energy that both contain mostly pions can have different responses in the calorimeter if one jet contains one very high energy pion while the other contains a large number of low energy pions.

The position resolution of the calorimeter varies from 0.8 mm to 1.2 mm as the impact position changes; the energy resolution follows the typical $1/\sqrt{E}$ dependence. The calorimeter is close to being compensating with the fraction of electromagnetic response to hadronic response varying from 1.11 for 10 GeV and 1.04 for 150 GeV (See section 3.4).

3.5 The Muon system

Although this analysis does not make use of muons, the muon system should be briefly described as an integral part of the DØ detector. In principle, this analysis could be repeated with muons instead of electrons. This might be an option for Run II where the momentum resolution for muons will be greatly improved due to the new tracking system.

Due to their long lifetime of 2.2 μs, muons don't decay within the detector. Since they are very massive compared to electrons, their likelihood for initiating electromagnetic showers in the calorimeter is greatly reduced.

To track muons, a separate system of detectors is used which makes up the outermost part of the DØ detector (see figure 3.11). The muon system consists of five magnetized iron toroids and three layers of proportional drift tubes (PDT's). Two PDT layers surround the toroid while one layer is located before the toroid. The five magnets are: CF (Central Fe) covering the angular range $\mid \eta \mid \leq 1.0$, the two EF(End Fe) from $\mid \eta \mid = 1.0$ to $\mid \eta \mid = 2.5$, and the two SAMUS (Small Angle MUon System)magnets, covering the range from about $\mid \eta \mid = 2.5$ to about $\mid \eta \mid = 3.6$. The CF and EF together are also referred to as the WAMUS (Wide Angle Muon System). The Drift tubes measure the trajectories of the muons before and after they traverse the magnetized iron which makes a measurement of the muon momentum possible: The inner layer provides the entrance point of the muon into the magnetic field while the two outer layers yield the exit direction. In addition, the iron of the toroid also provides shielding from pions that get through the calorimeter, making it possible to detect muons in the middle of hadronic jets with great purity.

3.6 Triggering and Data Acquisition

The beam crossing rate at the Tevatron during Run 1 was 286 kHz which corresponds to 3.5 μs between crossings. At a luminosity of $5 \times 10^{30} \mathrm{cm}^{-2}\mathrm{s}^{-1}$, this amounts to an average of 1.2 interactions per crossing, which would result in an enormous amount of data not manageable by the fastest and most sophisticated readout system. Moreover, since most physics processes of interest have rather small cross sections (for example top (5nb), W (20 nb), jets (10's μb)) compared to the total (elastic and inelastic) $p\overline{p}$ cross section of 70 mb at $\sqrt{s} = 1.8$ TeV; most of this data would not be useful for the most interesting physics analysis. Instead of blindly reading out every interaction, fast online decisions are made to determine if an event is interesting or not. A three step trigger system of increasing

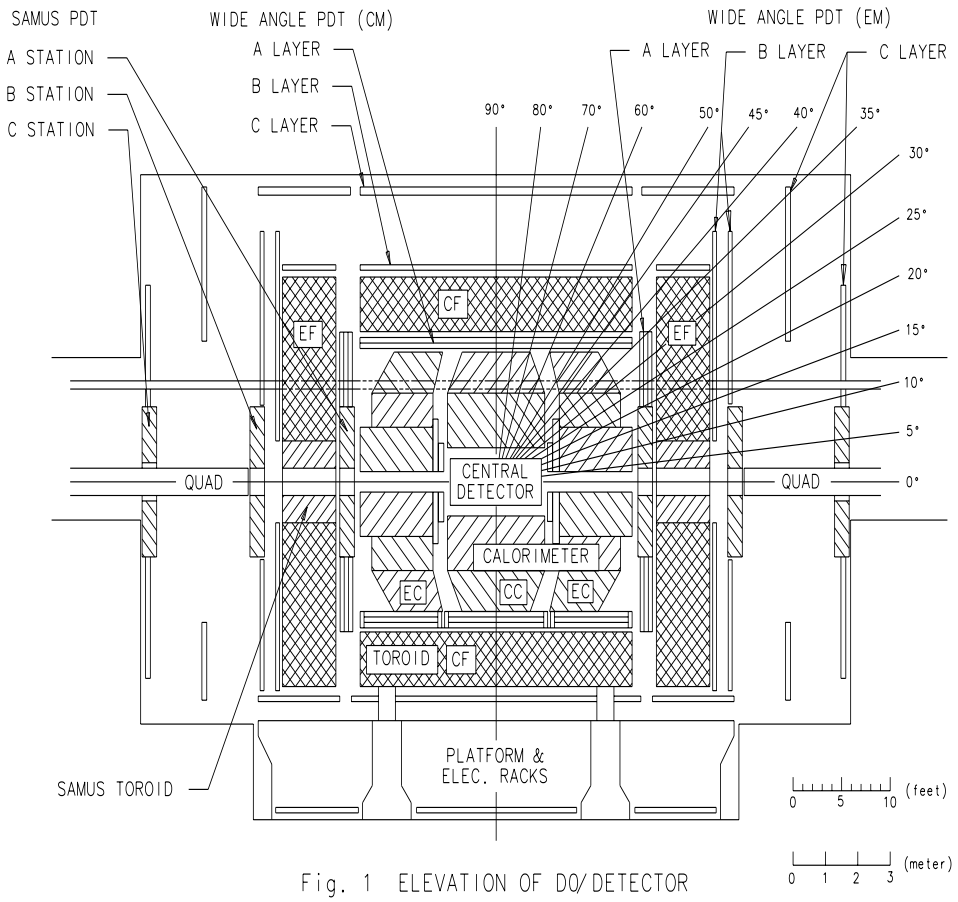

Figure 3.11: Side view of the muon system.

complexity as shown in figure 3.12 is implemented to quickly make these decisions with respect to various physics criteria.

In the first step, called Level-0, inelastic collisions are detected using scintillation counters. This reduces the rate to 150 kHz. Level-1 consists of a set of hardware triggers that operate mainly without dead time, i.e. within the 3.5 μs between beam crossings, further reducing the event rate to about 100 Hz. Some of the Level-1 trigger decisions, called Level-1.5, require additional time, however. After Level-1, events are fully digitized and can be transferred to Level-2, which is a set of software based algorithms running on a farm of 48 VAX 4000 microprocessors. These algorithms use simple and fast versions of the reconstruction programs.

The final readout rate is 2 Hz, limited by the bandwidth of the magnetic recording medium.

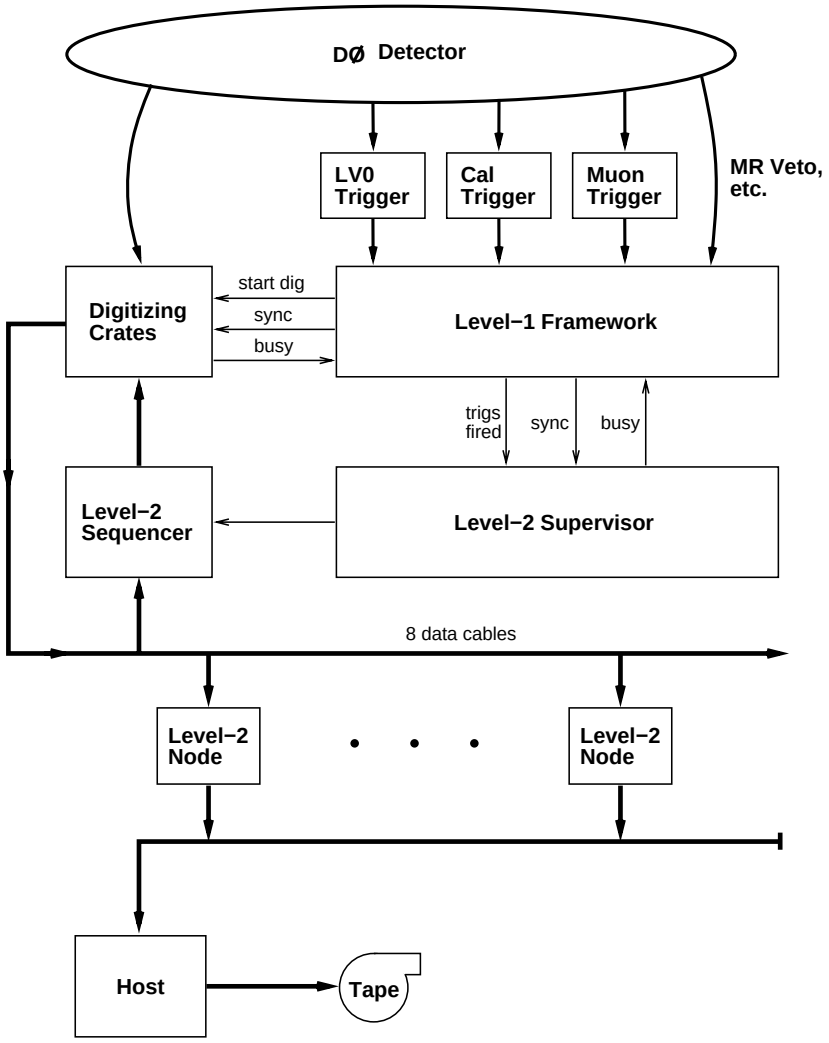

Figure 3.12: DØ trigger and data acquisition system.

3.6.1 Level-0

The Level-0 trigger uses two scintillation counter hodoscopes installed on each end of the EC modules. The information obtained from these scintillation counters serves three purposes: First, it is used as a very efficient ($\geq 99\%$) trigger which

fires if an inelastic collision of any kind has occurred. Second, the time difference of the signals between the two hodoscopes can be used to estimate the z-vertex position. This is done twice: The fast z algorithm takes 800 ns and provides Level-1 with a z-vertex measurement with $\sigma = 15$ cm compared to a z-vertex spread of 30 cm. The z-vertex position is later used to calculate the E_T of particles emerging from the interaction vertex. The slow z algorithm determines the z-vertex in 2.1 μs to $\sigma = 3.5$ cm and is used by Level-2. Finally, the rate at which the scintillation counters are hit serves as a luminosity monitor.

3.6.2 Level-1

The Level-1 trigger framework [25, 26, 27] consists of a dedicated hardware processor whose inputs are 256 single bit trigger terms. Each of these terms is related to a specific condition such as $\not\!\!E_T \geq$ 20 GeV or at least two muons present. A subsequent and/or network then reduces these 256 trigger terms to 32 Level-1 trigger bits or specific triggers. These triggers can be prescaled so that a trigger will only fire 1 in N times and vetoes related to any Main Ring activity can be activated. The Level-1 trigger decisions are based on detector data from the Level-0 hodoscopes, the accelerator timing signals, the calorimeter, and the muon system.

The Level-1 framework combines individual Level-1 components, coordinates vetoes that can inhibit triggers, and manages the readout of the digitization crates. The digitizing hardware is located in 86 front-end VME crates that are in the Moving Counting House which are mapped into 32 geographical sectors. For each of the 32 trigger bits the framework provides a list of sectors to be read out. The digitization electronics is double buffered which means that an event can be digitized while a previous event is still being read out. If Level-1.5 decisions are required, digitization is started but Level-2 is not informed until the Level-1.5 process is complete.

Level-1 Calorimeter Trigger

The Level-1 Calorimeter trigger, located on the first floor of the moving counting house, makes trigger decisions purely based on calorimeter information. For this purpose, the calorimeter cells are summed into towers of 0.2×0.2 in $\eta \times \phi$ space that cover the pseudorapidity region up to $|\eta| = 4.0$. This is done for EM and FH information separately, resulting in two times 1280 energy measurements. The fast z vertex as described earlier is used to calculate vertex-corrected transverse energies as well. The following quantities are calculated:

- The global corrected EM E_T;
- The global corrected hadronic E_T;
- The global corrected total E_T;
- The global uncorrected EM E_T;
- The global uncorrected hadronic E_T;
- The global uncorrected total E_T;
- The $\not\!\!E_T$.

These quantities can be compared with up to 32 programmable thresholds, each yielding a specific trigger term used as an input to the trigger framework. This makes it possible to specify trigger conditions like 'missing E_T above 15 GeV', or 'total corrected E_T above 100 GeV'.

In addition to these global sums, up to four different programmable reference values can be set to be compared with individual trigger tower energies. This can be done in two ways: A set of four EM tower thresholds in conjunction with four hadronic veto thresholds is used to trigger on the electromagnetic content of calorimeter towers: All towers with EM E_T above threshold t_1 and hadronic E_T

below t_2 are counted. Each pair of these thresholds is called an EM E_T reference set. In addition, a total E_T reference set is implemented for the total E_T of the tower. With this additional feature, trigger conditions like 'one EM tower above 15 GeV' or 'two EM towers above 10 GeV each' can be specified.

Level-1.5 Calorimeter Trigger

During Run 1a it was realized that with a low E_T threshold for electrons, which is necessary to retain high efficiency despite the poor E_T resolution at Level-1, the trigger rates for W and Z bosons would be so high that prescaling would be necessary. Since the amount of background strongly depends on the electron E_T threshold, it is desirable to improve the E_T measurement at the trigger level. This is done using the calorimeter Level-1.5 trigger [28, 29] that utilizes digital signal processing (DSP). Three quantities are computed at Level 1.5: a) An EM nearest neighbor algorithm is applied to all Level-1 candidates that adds the EM E_T of a seed tower to its highest E_T neighbor in η or ϕ resulting in $(2 \times 1)_{EM}$ clusters. b) In addition, the $(2 \times 1)_{total}$ is calculated in the same way using the total E_T. From these two cluster E_T's, the electromagnetic fraction (EMF) can be calculated. c)An EM isolation variable is defined as $(2 \times 1)_{EM}/(3 \times 3)_{total}$ where $(3 \times 3)_{total}$ is the sum of the total E_T of all nine towers around a seed. This variable is not used to trigger on W or Z bosons, however.

Typical conditions for the Level-1.5 calorimeter trigger are 'one EM object above 12 GeV ' or 'two EM objects above 10 GeV, one with EMF above 85%'.

Beam Vetoes

Main ring losses that occur mainly during injection (every 2.4 s) and transition (300 ms later) induce large amounts of noise in the calorimeter since the Main Ring passes through the DØ detector. Veto signals in the Level-1 framework are

implemented to reject events where these conditions apply: The **MRBS_LOSS** condition rejects events within a 400 ms window following an injection which results in 0.4 s /2.4 s $\approx$ 17% dead time. The **MICRO_BLANK** bit is set when Main Ring bunches pass through the detector within 1.6 μs of a Tevatron beam crossing, resulting in 8 % dead time.

3.6.3 Level-2

The Level-2 system serves both as the DØ data acquisition system and as a software trigger. The Level-2 trigger consists of general-purpose processors which run software filters on the complete data for an event. For each Level-1 trigger bit, a filter script exists which lists a set of Level-2 tools to do the actual filtering together with a set of parameters describing the cuts to be made by the tool. Specific tools exist for the following particle types: Jets, muons, calorimeter EM clusters, tracks associated with calorimeter clusters, scalar E_T (ΣE_T), and $\not\!\!E_T$.

As an example for such a tool consider the jet tool, whose parameters might be the minimum jet E_T, conesize to be used, and minimum number of jets. If all the tools for a specific script pass, the script passes as a whole and the corresponding bit in a 128-bit mask of filter bits is set. If at least one filter bit is set, the event gets passed to the host cluster. The host or online cluster, consisting of three DEC VAX nodes supplemented by a number of X-window terminals, serves as an interface to the detector systems and manages the output to magnetic tape and/or to a separate data stream for monitoring. It also is used to control data taking and for downloading of run parameters.

Offline reconstruction is performed on a farm of up to 96 SGI and IBM nodes. Data is stored in ZEBRA [30] format which allows for dynamic memory management in FORTRAN. At DØ, three different types of output files were used: STA's, DST's, and μDST's. STA files contain the raw data of the event along

with the result of the reconstruction and are 600-1000 kbytes/event large; DST's only contain a summary of the event data, along with the reconstruction results for high-level objects like electrons, photons, muons, and jets. Their size about 15 kbytes/event. μDST's are even smaller since they contain only the minimum amount of information necessary for physics analyses.

3.7 A Few Words on the Upgrade

One of the drawbacks of the DØ detector during Run I was the lack of a central magnetic field for sign identification of particles. The upgrade [31, 32] for Run II includes a 2 Tesla superconducting solenoid magnet which will be placed in the central part of the detector. Another major improvement will be the installation of a silicon microstrip tracker (SMT) for precise tracking and vertex finding.

Chapter 4

Event Reconstruction and Particle Identification

The information recorded by the DØ detector consists of digital signals which contain information about pulse heights, widths and times. These signals have to be converted into physics objects which can then be used in a physics analysis. At DØ, a standard software reconstruction package, DØRECO, has been developed to fulfill this task. The following sections briefly describe how raw data as recorded during a collider run is converted into higher level objects like energy clusters in the calorimeter or particle tracks which finally can be associated with objects like electrons or hadronic jets.

4.1 Track Reconstruction

Track Reconstruction in the Central Drift Chamber can be described as a chain of three subsequent processes:

- Pulse and Hit Finding;

- Segment Finding;
- Segment Matching and Global Track Fit.

The raw data coming from the Flash Analog-To-Digital converters (FADC's) contains digitized charge versus time information together with the address for the associated sense wire. After channel-by-channel corrections are applied, the integrated pulse can be used to compute the total deposited charge while timing information is translated into the position of the pulse: The drift time to the sense wire gives the distance of the hit from the sense wire while the arrival time of the pulse from the delay line (as described in Chapter 3) is translated into the location of the hit along the sense wire. As mentioned before, in order to reduce the number of readout channels, each sense wire is read out in the middle, dividing the drift volume into two symmetric halves. Consequently, individual drift times cannot allow one to determine from which side of the wire the electrons drifted. This results in a left-right ambiguity for each hit: One hit corresponds to the true track, while the other is its mirror image. This ambiguity is resolved by staggering the sense wires. The correct hit is then the one which gives a better track fit.

To reduce the number of tracks to be considered for track finding, segments of hits within a single layer are defined first. Hits within a segment are found using a road method in the $r - \phi$ plane (the z information is added later). The road is defined by a pair of hits which span the sector: One hit from the innermost and one from the outermost wire. The roads defined this way are straight (in the absence of a magnetic field in Run I) and almost radial as tracks originate from the interaction vertex and are not subject to a significant source of multiple scattering in the inner part of the tracking system. The width of the roads is chosen as roughly five times the single hit resolution to retain full efficiency while minimizing the number of fake track segments.

Once a sufficient number of hits is found within a road, an overall straight line fit is performed. A segment is formed if the corresponding χ^2 per degree of freedom is less than 10. After all segments are found, they can be easily linked to form tracks: Two segments are linked if they lie along the same line, i.e they must point to the same direction in space and their spatial mismatch in the mid-plane between the two layers must be small. After all segments are linked, a final straight line fit is performed using all hits from the linked segments. A track is found, if this fit is considered good enough and a minimum of three (out of the four) layers are found.

The track reconstruction, as described above, is performed in all three central drift chambers (VTX, CDC, and FDC), while hit and track finding in the forward direction is only performed in wide roads defined by the calorimeter clusters and the event vertex. A reconstructed track is described by five parameters which are chosen to be the coordinates of a reference point (x_0, y_0, z_0), called the track centroid or track center of gravity, along with the polar angle θ and the azimuthal angle ϕ. The track centroid is corrected for any biases in the delay lines. The z-coordinate of CDC tracks has been calibrated using cosmic ray and collider muons. More detailed discussions of hit finding and tracking can be found in [33, 34, 35, 36].

4.2 Vertex Finding

At DØ, two different methods for vertex finding have been used: One, employed by DØRECO, uses a simple histogram of z-intercept technique (called RECO vertex method) while the other (referred to as cluster or CLUS vertex method, described in section 4.7.5) uses only tracks associated with electromagnetic clusters to reconstruct the vertex position. In the following section both methods will be described, although this analysis uses the CLUS vertex method.

4.2.1 The Reco Vertex

Each CDC track is projected onto the beam line ($x \approx y \approx 0$) and the resulting z-intercepts are histogramed as seen in figure 4.1. The primary vertex is simply the vertex with the largest number of associated tracks while secondary vertices are assumed to arise from minimum bias interactions. Typical vertex z resolutions achieved with this method are 1-2 cm, while multiple vertices can be resolved when they are at least 7 cm apart. The shortfall of this method is that it becomes unreliable at high luminosities when the number of interactions per bunch crossing increases. If the track multiplicity of the high p_T interaction happens to be smaller than the one from a minimum bias interaction, this method assigns the wrong primary vertex.

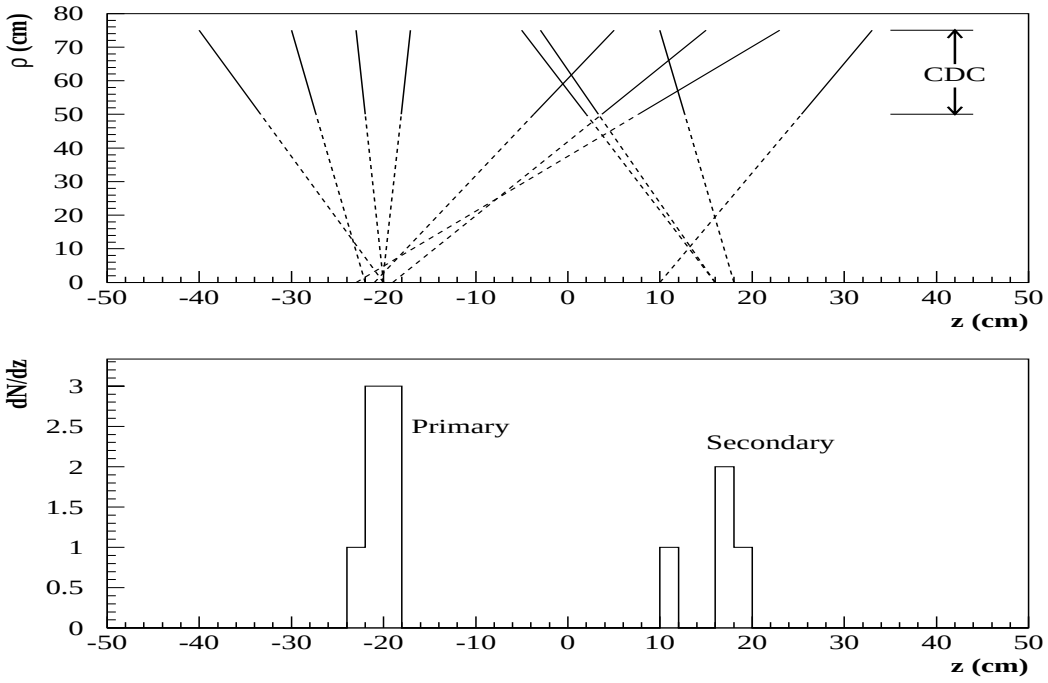

Figure 4.1: Vertex z coordinate finding by the histogram method as used by DØRECO. The upper plot shows CDC tracks projected onto the beamline (for all ϕ). The lower plot shows the corresponding z-intercept distribution.

4.3 Hit Finding in the Calorimeter

The digital information obtained by reading out calorimeter cells that pass zero suppression has to be converted into physical energy measured in GeV. This conversion is done taking into account various correction factors that can be run-dependent or vary from cell to cell. The energy conversion is written as follows:

$$E_{cell}(e,p,l) = A(d) \times W(e,l) \times C(e,p,l) \times G(e,p,l) \times ADC(e,p,l) \qquad (4.1)$$

where E_{cell} is the cell energy in GeV, and (e,p,l) correspond to:

- e = calorimeter η index: $-37 \leq e \leq 37$
- p = calorimeter ϕ index: $1 \leq p \leq 64$
- l = calorimeter depth (layer) index: $1 \leq l \leq 17$

A is an overall calibration constant dependent on the module type: Central calorimeter (CC), end calorimeter (EC), inter-cryostat detector (ICD), CC massless gap (CCMG), or EC massless gap (ECMG). A contains the conversion from ADC counts to GeV and includes high voltage corrections. W is the sampling fraction weight, determined from test beam data, which provides the best energy resolution. C contains all non-run dependent corrections such as absorber thickness in the CC and EC, or the ICD minimum ionizing signal corrections. G contains run dependent electronic gain corrections, such as response corrections due to capacitance or timing (derived from calibration runs), or shorted or missing channels. ADC is the digitized cell energy in raw ADC counts.

For each calorimeter cell, a directed energy vector can be defined as follows:

$$\vec{E}_{cell}(e,p,l) = \hat{n} E_{cell}(e,p,l) \qquad (4.2)$$

where $\hat{n}$ is the unit vector from the interaction vertex to the center of cell (e,p,l) and $E_{cell}(e,p,l)$ is the magnitude of the energy deposited in the cell. The cell

energy can then be decomposed into vectorial components:

$$E_x = E\sin\theta\cos\phi \qquad E_y = E\sin\theta\sin\phi \qquad E_z = E\cos\theta \tag{4.3}$$

and the transverse component is:

$$E_T = \sqrt{E_x^2 + E_y^2} = E\sin\phi \tag{4.4}$$

The final step in calorimeter hit finding consists of summing the energies of all the calorimeter cells in each $\eta - \phi$ tower. Cells are summed over the layer index l. The total and the electromagnetic energy are calculated separately, the electromagnetic energy is the sum of the cells in a given $\eta - \phi$ tower for the electromagnetic calorimeter (layers 1 through 7) and the first layer of the fine hadronic calorimeter (layer 8), while the total energy includes all 17 layers of the electromagnetic and hadronic calorimeter.

$$E_{tower}^{EM}(e,p) = \sum_{l=1}^{8} E_{cell}(e,p,l) \tag{4.5}$$

and

$$E_{tower}^{TOT}(e,p) = \sum_{l=1}^{17} E_{cell}(e,p,l) \tag{4.6}$$

The vectorial components for each tower are computed from the vectorial components of the cells:

$$E_x^{tower} = \sum_{layers} E_x^{cell} \qquad E_y^{tower} = \sum_{layers} E_y^{cell} \qquad E_z^{tower} = \sum_{layers} E_z^{cell} \tag{4.7}$$

and

$$E_T^{tower} = \sqrt{(E_x^{tower})^2 + E_y^{tower})^2} \tag{4.8}$$

The tower angles are computed as follows:

$$\phi_{tower} = \arctan\frac{E_y^{tower}}{E_x^{tower}} \tag{4.9}$$

$$\theta_{tower} = \arccos \frac{E_z^{tower}}{E^{tower}} \tag{4.10}$$

$$\eta_{tower} = -\ln[\tan \frac{\theta_{tower}}{2}] \tag{4.11}$$

These tower energies form the building blocks, or seeds, of the jet and electron cluster finding algorithms.

4.4 Missing Energy

Since the cross sections for processes by which neutrinos could be detected are extremely small, most neutrinos pass through the detector undetected. The transverse momentum of the neutrinos can, nevertheless, be measured by applying momentum conservation and the fact that the initial transverse momentum of the quark-antiquark system is small (≈ 300 MeV). The energy imbalance, referred to as $\not\!\!E_T$, is calculated by adding the calorimeter energies componentwise at the cell level:

$$\not\!\!E_x = -\sum_{e,p.l} E_x(e,p,l) \qquad \not\!\!E_y = -\sum_{e,p.l} E_y(e,p,l) \tag{4.12}$$

and

$$\vec{\not\!\!E}_T = \begin{pmatrix} \not\!\!E_x \\ \not\!\!E_y \end{pmatrix} \tag{4.13}$$

The missing transverse energy, $\not\!\!E_T$, is the magnitude of this vector:

$$\not\!\!E_T = |\vec{\not\!\!E}_T| = \sqrt{\not\!\!E_x{}^2 + \not\!\!E_y{}^2} \tag{4.14}$$

Since particles emitted in the forward direction often escape the detector undetected, the z-component of the missing energy cannot be associated with the longitudinal component of the neutrino momentum in this way.

4.5 Jet Reconstruction

Although this analysis does not make use of hadronic jets, jet reconstruction is discussed here briefly for completeness. Since colored partons cannot remain free particles, they cause a collimated spray of new hadrons to be created which is called a hadronic jet (see chapter 1). The objective of a jet algorithm is to identify these jets, determine their kinematic quantities and relate them to their original partons.

Several different jet finding algorithms can be used; at DØ a fixed cone algorithms is implemented for four different cone sizes in $\eta \times \phi$ space, $\mathcal{R} = \sqrt{\Delta\eta^2 + \Delta\phi^2} =$ 0.3, 0.5, 0.7, and 1.0. Jet finding with the cone algorithm is done in three steps:

- Preclustering;
- Cone clustering of preclusters;
- Splitting and Merging.

First an E_T-ordered list of seed towers is made where each calorimeter tower with $E_T > 1$ GeV is considered a seed. Then the first seed tower is taken and all adjacent seed towers within ± 0.3 in η and ± 0.3 in ϕ are added to it forming a precluster. All towers used in a precluster are removed from the list of available seeds and the process is repeated with the next remaining seed tower in the list until all seeds are used. The preclusters obtained are then ordered in decreasing precluster E_T which is the scalar sum of all the tower E_T's.

For each precluster the E_T weighted centroid in (η, ϕ) is calculated to define a cone axis and all towers within $\mathcal{R}$ are included to form a cone cluster. The cone axis is then recalculated using all the towers in the cone and the process is iterated until it is considered stable.[1] All cones with $E_T > 8$ GeV are kept.

[1] The cone axis is considered stable if it changes by less than 0.01 in (η, ϕ)-space. After 50 iterations, the process is also stopped to prevent excessive computing time in the case of bi-stable

Two cone jets are not allowed to share calorimeter cells. If a jet shares one or more calorimeter towers with a previously found one, the following actions are taken: If the two jets are closer than 0.01 in (η, ϕ) space, the newer jet is dropped. If they are further apart, the fraction of the shared E_T to the E_T of the lower E_T jet is calculated. If that fraction is larger than 0.5, the two jets are merged into one jet by combining their towers. If the fraction is less than 0.5, both jets are kept (split) and each shared cell is assigned to the closest jet. On average, 5% of the jets are merged and 30% are split. After the splitting/merging process is completed, the cone clustering process is repeated until all preclusters are exhausted.

After all jets have been found, kinematic quantities are computed for each jet by summing over calorimeter towers contained in that jet. The energy components are defined to be

$$E_i^{jet} = \sum_{k=1}^{n_{towers}} E_i^k \qquad (i = x, y, z, total) \tag{4.15}$$

and the E_T of the jet is:

$$E_T^{jet} = \sum_{k=1}^{n_{towers}} E_T^k = \sum_{k=1}^{n_{towers}} \sqrt{(E_x^k)^2 (E_y^k)^2} \tag{4.16}$$

The jet angles are calculated as follows:

$$\phi^{jet} = \arctan\left(\frac{E_y^{jet}}{E_x^{jet}}\right) \tag{4.17}$$

$$\theta^{jet} = \arccos\left(\frac{E_z^{jet}}{E_{total}^{jet}}\right) \tag{4.18}$$

$$\eta^{jet} = -\ln\left[\tan\left(\frac{\theta^{jet}}{2}\right)\right] \tag{4.19}$$

solutions.

4.6 Electron Reconstruction

Showers from electrons and photons are very similar, both are narrow clusters of energy concentrated in the electromagnetic layers of the calorimeter. Electrons can be distinguished from photons by the fact that they have tracks in the central tracking chambers associated with the cluster. The following discussion includes showers from electrons and photons.

Electromagnetic objects are reconstructed using a nearest neighbor (NN) algorithm based on tower energy, not E_T. Clusters of 3×3 towers are formed for towers with an energy above 50 MeV. The kinematic properties for each cluster found are computed from the cell energies:

$$E_i^{clus} = \sum_{k=1}^{n_{cells}} E_i^k \qquad (i = x, y, z, total) \tag{4.20}$$

The transverse cluster energy is:

$$E_T^{clus} = \sqrt{(E_x^{clus})^2 + (E_y^{clus})^2} = \sqrt{\left(\sum_{k=1}^{n_{cells}} E_x^k\right)^2 + \left(\sum_{k=1}^{n_{cells}} E_y^k\right)^2} \tag{4.21}$$

The angles are defined as follows:

$$\phi^{clus} = \arctan\left(\frac{E_y^{clus}}{E_x^{clus}}\right) \tag{4.22}$$

$$\theta^{clus} = \arccos\left(\frac{E_z^{clus}}{E_{total}^{clus}}\right) \tag{4.23}$$

and

$$\eta^{clus} = -\ln\left[\tan\left(\frac{\theta^{clus}}{2}\right)\right] \tag{4.24}$$

To distinguish electromagnetic objects from hadronic jets, two more energies are computed: E_{had} is the energy deposited in the first hadronic layer while E_{trans} is the energy outside the hottest tower (in η direction) of the cluster. With these quantities, a set of quality criteria is defined which an electron or photon candidate (called an electromagnetic object) has to satisfy:

- The total cluster energy E_{total} >1.5 GeV;
- The total transverse cluster energy E_T >1.5 GeV;
- The electromagnetic energy fraction is greater than 90% ($E_{had}/E_{total} < 0.1$);
- The hottest tower (i.e. the one containing the most energy) of the cluster has to contain at least 40% of the energy ($E_{trans}/E_{total} < 0.6$).

Once an electron or photon candidate is obtained, the cluster centroid, $\vec{x}_{clus}$, is calculated from the weighted mean of the coordinates $\vec{x}_i$ of the cluster cells in the finely segmented EM3 layer:

$$\vec{x}_{clus} = \frac{\sum_i w_i \vec{x}_i}{\sum_i w_i} \tag{4.25}$$

A logarithmic weighing scheme based on the cell energy E_i is chosen to account for the exponentional lateral profile of the shower shape:

$$w_i = \max\left[0, w_0 + \ln\left(\frac{E_i}{E_{clus}}\right)\right] \tag{4.26}$$

where w_0 is a parameter chosen to optimize the position resolution. The weights are η and ϕ dependent and were determined from test beam data.

At this point, the distinction between electrons and photons can be made based on central tracks. Tracking roads are defined between the calorimeter clusters and the primary interaction vertex position. These roads cover an azimuthal angle of ± 0.1 radians around the cluster position. In θ the road limits are determined as follows:

$$\tan\theta_{\pm} = \min\left[\frac{\rho_{clus}}{(z_{clus} - z_{vtx} \pm \delta z)}, 0.1\right] \tag{4.27}$$

where $\vec{x}_{clus} = (x_{clus}, y_{clus}, z_{clus})$ are the coordinates of the cluster centroid, $\rho_{clus} = \sqrt{x_{clus}^2 + y_{clus}^2}$, z_{vtx} is the z-coordinate of the primary interaction vertex, and δz is its error. If one or more tracks are found in such a road, the candidate cluster is defined as an electron, otherwise it passes as a photon. This method fails if the

vertex position is misidentified, usually causing the tracks from a real electron not to be found which means it only passes as a photon. This analysis makes use of an improved track finding technique which is independent of the vertex position (described later).

4.7 Electron Identification

The identification criteria imposed on electrons by DØRECO described so far are optimized for high efficiency which means that at this point large background is still present among electron candidates. Further quality cuts have to be imposed to reduce backgrounds while keeping the electron selection efficiency reasonably high. Standard techniques have been developed to this end. A set of four such cuts is commonly used at DØ, two of which make use of differences between electromagnetic and hadronic showers in the calorimeter: The electromagnetic fraction (f_{em}) and the H-matrix chi-squared (χ^2_{hm}), which is derived from a shower shape analysis. The third criterium, the shower isolation fraction (f_{iso}) is a topological cut designed to select electrons from the decay of W and Z bosons. The fourth cut, the track match significance (S_{trk}), quantifies the quality of the track matching performed for electrons using calorimeter and tracking information. In the following sections these four electron identification criteria will be described in some detail. For more information on the various electron identification cuts and the choices of their values see [37].

4.7.1 Electromagnetic Energy Fraction

By definition, electrons and photons must have more than 90% of their cluster energy deposited in the EM layers of the calorimeter. Electrons from W and Z boson decays typically have much larger electromagnetic energy fractions; tight-

ening this cut can be used to further reduce background without compromising the selection efficiency. Figure 4.2 shows the electromagnetic energy fraction for $Z \to ee$ candidates and for mainly fake electron candidates in multi-jet triggered data. It can be seen that a cut at $f_{em} = 0.95$ does not significantly reduce the acceptance for real electrons while cutting out a large fraction of fakes.

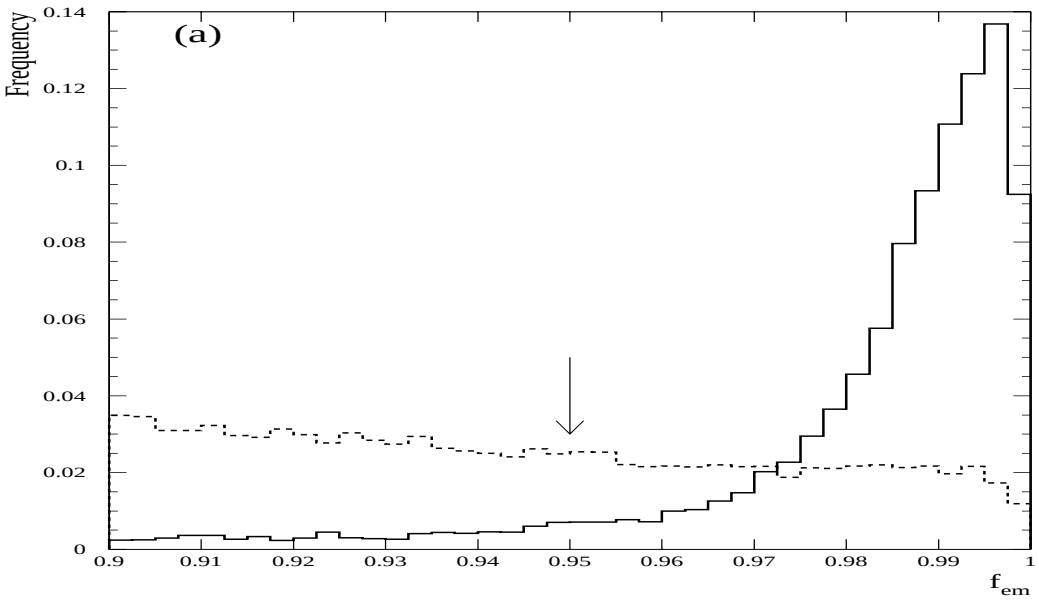

Figure 4.2: Electromagnetic energy fraction f_{em} distributions for $Z \to ee$ candidates (solid) and electrons in multi-jet triggered data (dashed) (Central Electrons).

4.7.2 Shower Shape Analysis

A powerful discriminant for electromagnetic objects is based on a detailed study of the longitudinal and transverse shower profile [38, 39, 40]. It is based on the fractional energy deposited in each cell of the calorimeter. These fractions, besides being dependent on the incident electron energy and impact position, are correlated: If a shower deposits more energy in the first layer of the electromagnetic

calorimeter due to a fluctuation it will on average deposit less in the subsequent layers. To fully account for all possible correlations, a covariance matrix M of 41 observables is built which is a measure of how "electron-like" a shower is. The variables are the fractional energies in layers EM1, EM2, and EM4 of the calorimeter and the fractional energy in each cell of a 6×6 array in $\eta - \phi$ space of the finely segmented EM3 centered around the most energetic tower in the cluster. The logarithm of the cluster energy is included to account for the dependence of the fractional energy on the cluster energy. Finally, the z-coordinate of the interaction vertex is included to account for the dependence of the shower shape on the incidence angle into the calorimeter. To account for the fact that the geometry of the calorimeter is η-dependent, 37 different matrices M are built, one for each tower in pseudorapidity in one half of the calorimeter. The other 37 in the other half can simply be obtained using the fact that the calorimeter is mirror-symmetric.

The covariance matrix M is built using Monte Carlo electrons with a large energy range (from 10 GeV to 150 GeV). For two variables x_i and x_j it is defined as:

$$M_{ij} = \frac{1}{N} \sum_{n=1}^{N} (x_i^n - \overline{x}_i)(x_j^n - \overline{x}_j) \tag{4.28}$$

where the sum is performed over N reference electrons. The matrices were verified using test beam electrons. This test is important since small differences in shower shapes between Monte Carlo and real electrons could result in large variations in the correlation matrix.

To measure how consistent the shape of a certain cluster is with the shape of an electromagnetic cluster, the χ^2 is computed as follows:

$$\chi^2_{hm} = \sum_{i,j=1}^{41} (x'_i - \overline{x}_i) H_{ij} (x'_j - \overline{x}_j) \tag{4.29}$$

A shower that closely resembles an electromagnetic shower will have a low χ^2_{hm}. The χ^2_{hm}-distribution does not follow a true χ^2 distribution because in general, the

observables x_i are not normally distributed. This does not keep this variable from being a very powerful tool to distinguish electromagnetic from hadronic showers, merely the values are not easily interpreted and a cut is chosen to optimize background versus efficiency. Figure 4.3 shows the distributions of the H-matrix χ^2 variable for test beam electrons and electrons from W boson events and compares these to test beam pions. Electrons peak at low values of χ^2_{hm} while pions pile up at large values. Figure 4.4 shows χ^2_{hm} distributions for electrons from $Z \to ee$ candidates and electron candidates in multi-jet triggered data. A cut typically used by previous analyses of 100 (for the central calorimeter) conserves high acceptance for real electrons while cutting out a large fraction of fakes.

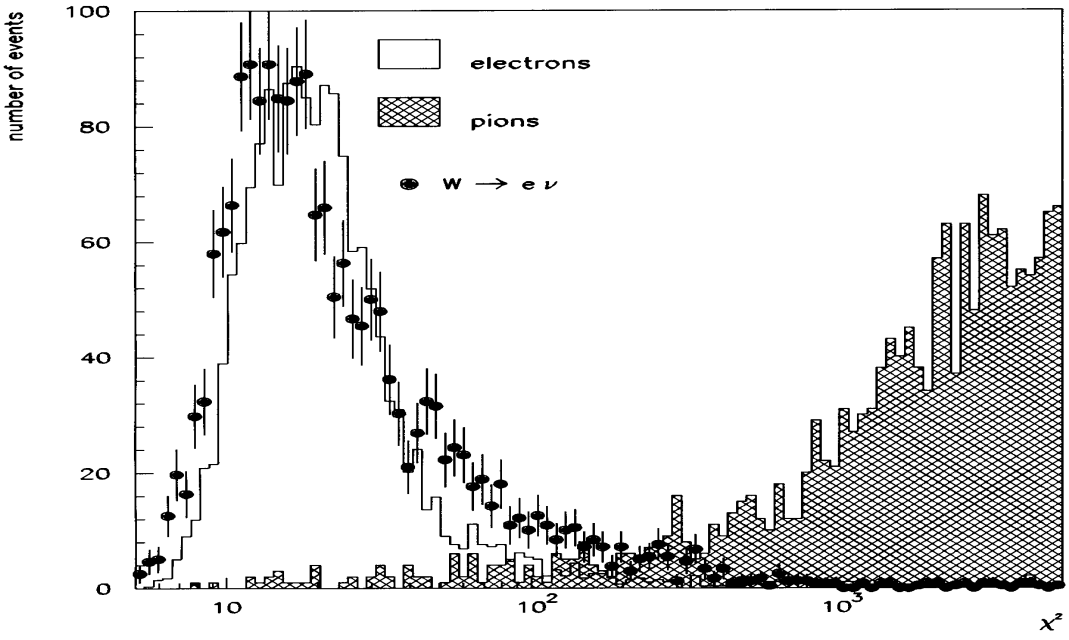

Figure 4.3: χ^2_{hm} distributions for test beam electrons (unshaded), test beam pions (shaded), and electrons from $W \to e\nu$ events (dots).

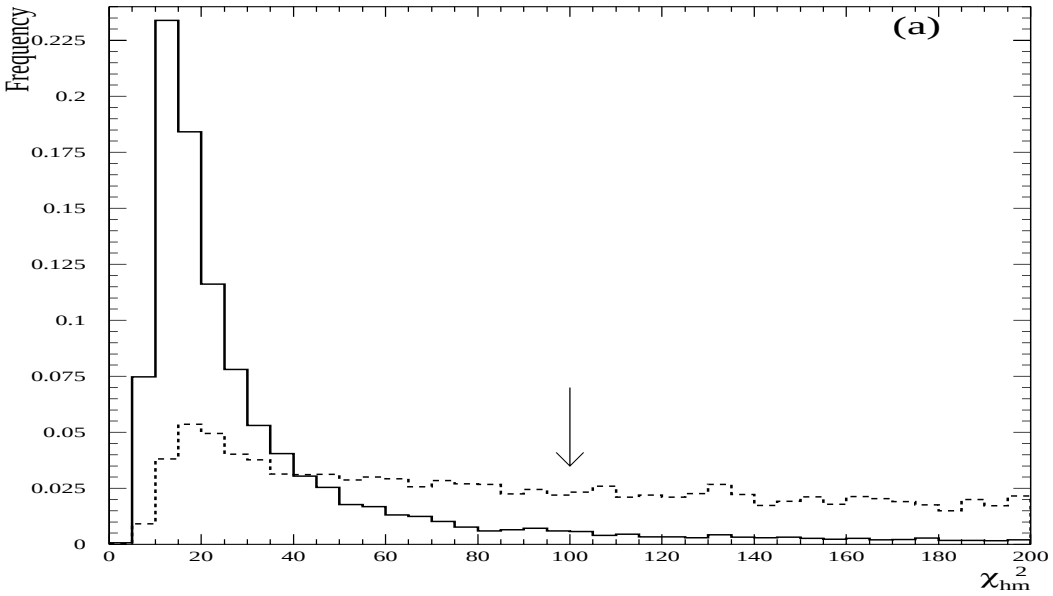

Figure 4.4: H-matrix χ^2_{hm} distributions for electrons from $Z \rightarrow ee$ candidates (solid) and electrons in multi-jet triggered data (dashed) (Central electrons).

4.7.3 Shower Isolation

Electrons originating from W and Z boson decays are isolated since these electrons are not produced together with other particles. In the case of the production of π^0 and η particles (which can mimic electrons) or electrons from heavy quark decays, the electron is most often accompanied by other hadrons.

An isolation variable is defined as follows:

$$f_{iso} = \frac{E_{total}(0.4) - E_{EM}(0.2)}{E_{EM}(0.2)} \tag{4.30}$$

where $E_{total}(0.4)$ is the total energy in an isolation cone of radius $\mathcal{R} = 0.4$ and $E_{EM}(0.2)$ is the electromagnetic energy in a core cone of radius $\mathcal{R} = 0.2$. A cut on f_{iso} will largely reduce the contribution from electrons from other sources. Unlike the selection criteria described before, this cut selects specific kinds of electrons, electrons from W and Z boson decays, while rejecting real electrons from other unwanted sources. Figure 4.5 compares the f_{iso} distributions of electrons from

$Z \rightarrow ee$ events to the ones from multi-jet triggered data. The loose cut $f_{iso} \leq 0.15$ cuts out a significant fraction of electrons from sources other than W and Z boson decays.

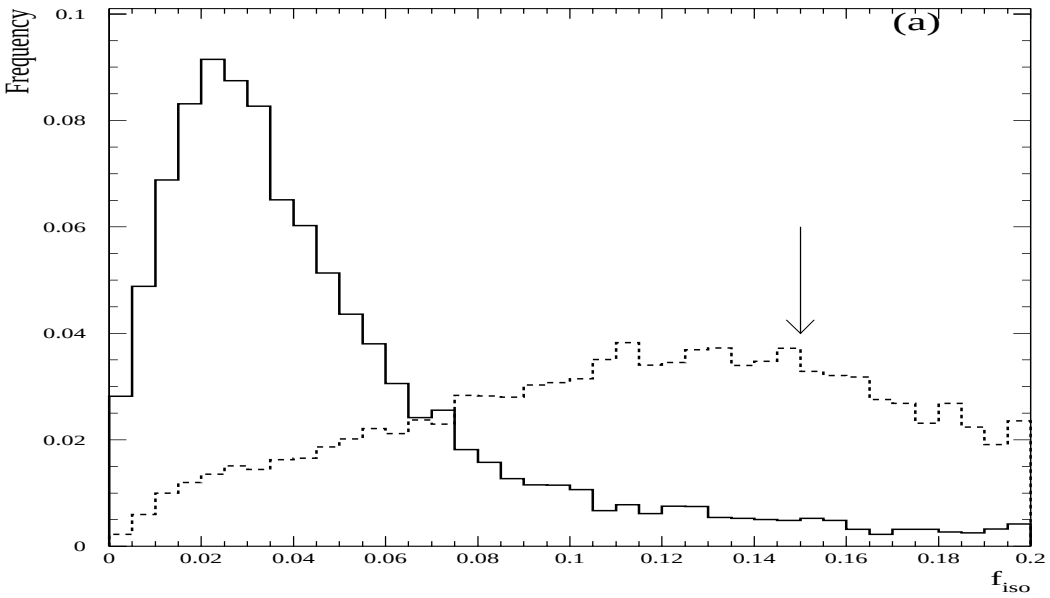

Figure 4.5: Isolation distribution f_{iso} for electrons from $Z \rightarrow ee$ candidates(solid) and electrons in multi-jet triggered data (dashed) (Central electrons).

4.7.4 Track Matching

The requirement imposed on an electron at the DØRECO level to have at least one track in a wide road defined by the vertex position and the cluster centroid is rather loose. Accidental overlaps for example from pions or η particles can cause tracks to be present in the roads amounting to large backgrounds.

Tracks produced by electrons can be distinguished from accidental overlaps by taking into account how well their projections from the interaction vertex into the EM3 layer of the calorimeter match the cluster centroids. Tracks associated with real electrons will have a very good track match. The track match significance in

the central calorimeter is defined as follows:

$$S_{trk}^{CC} = \sqrt{\left(\frac{\rho\Delta\phi}{\sigma_{\rho\phi}}\right)^2 + \left(\frac{\Delta z}{\sigma_z}\right)^2} \tag{4.31}$$

where $\rho\Delta\phi$ is the transverse spatial mismatch, Δz is the longitudinal spatial mismatch, and $\sigma_{\rho\phi}$, and σ_z are the corresponding resolutions. For the endcap calorimeter a similar expression exists:

$$S_{trk}^{EC} = \sqrt{\left(\frac{\rho\Delta\phi}{\sigma_{\rho\phi}}\right)^2 + \left(\frac{\Delta\rho}{\sigma_\rho}\right)^2} \tag{4.32}$$

where $\rho\Delta\phi$ is the transverse spatial mismatch, $\Delta\rho$ is the longitudinal spatial mismatch, and $\sigma_{\rho\phi}$, and σ_ρ are the corresponding resolutions. Figure 4.6 shows the difference in cluster centroid and EM3 projected positions for electrons from $Z \to ee$ candidates with low track match significance for central and forward electrons. Figure 4.7 illustrates the definition for S_{trk}. In figure 4.8, the S_{trk} distribution for electrons from $Z \to ee$ candidates is compared to electron candidates from the same control sample as before. A cut of 5 in the CC reduces the rate for fake electrons significantly while keeping the acceptance for real electrons high.

4.7.5 The Cluster Vertex

If the vertex found by DØRECO is wrong, it can happen that no charge track is found in the tracking road defined by the vertex and the cluster, and consequently, the electron is undetected. A better way to measure the vertex position relies on calorimeter clusters and associated tracks ([41, sec.4.8.1]) For each electromagnetic cluster in the calorimeter, a search among all CDC and FDC tracks is performed for the best matching track regardless of whether the track was contained in a tracking road. The center of gravity of this track together with the center of gravity of the calorimeter cluster is then used to project to the beamline to find the vertex:

$$z_v = z_0^{trk} - \left(\frac{z_0^{cal} - z_0^{trk}}{\rho_0^{cal} - \rho_0^{trk}}\rho_0^{trk}\right) \tag{4.33}$$

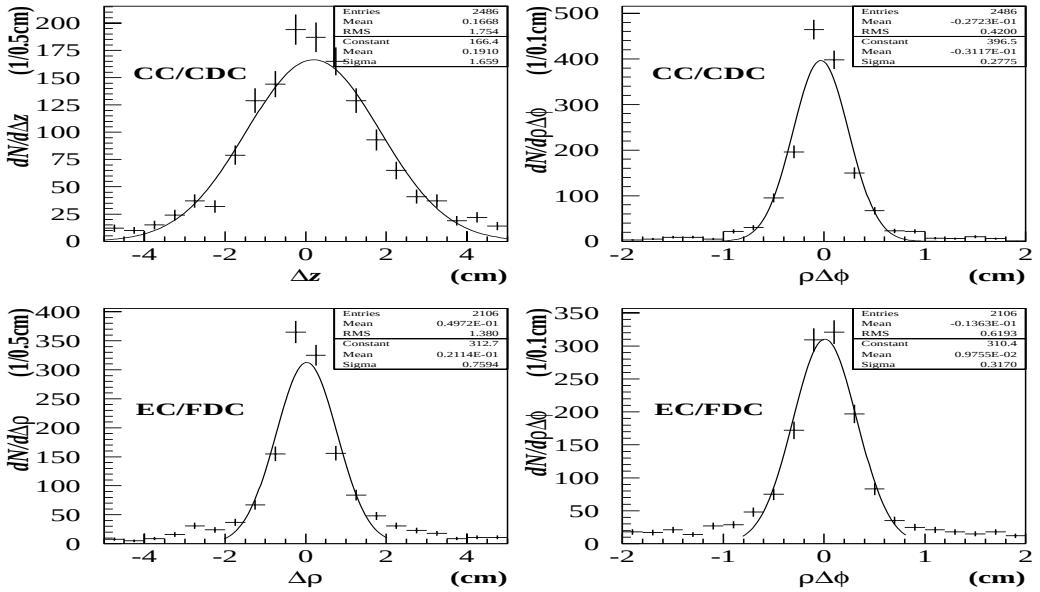

Figure 4.6: Differences in cluster centroid and EM3 projected track positions for electrons from $Z \to ee$ candidates with $S_{trk} < 30$.

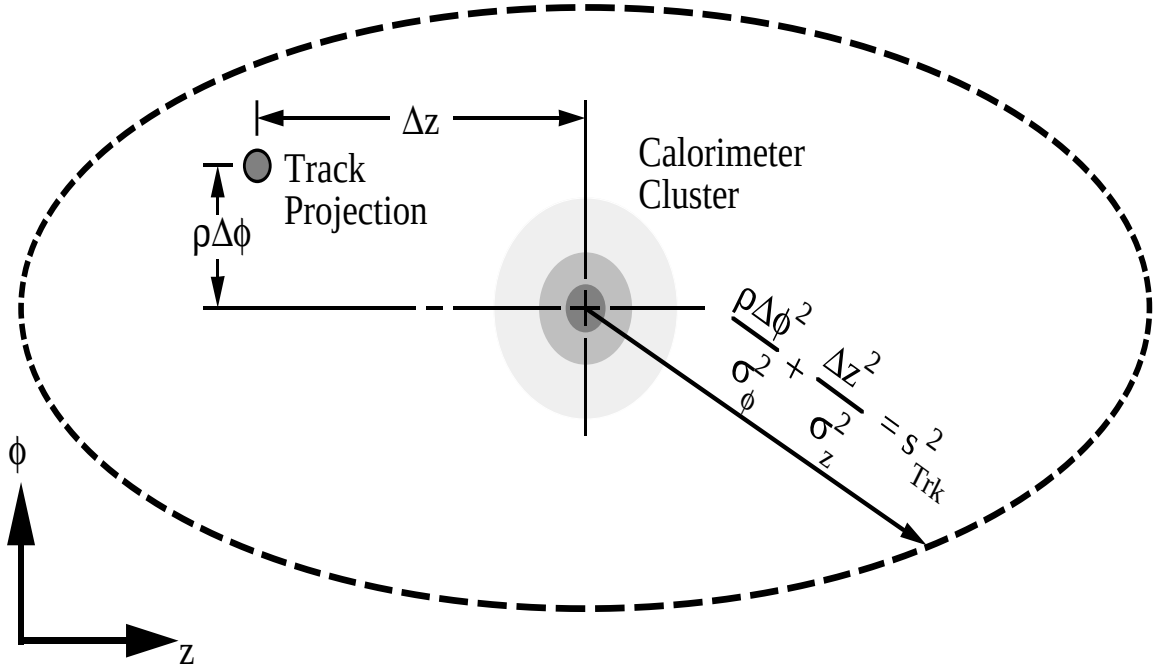

Figure 4.7: Definition of the track match significance in terms of the cluster centroid in EM3 and the projection of the track to that radius.

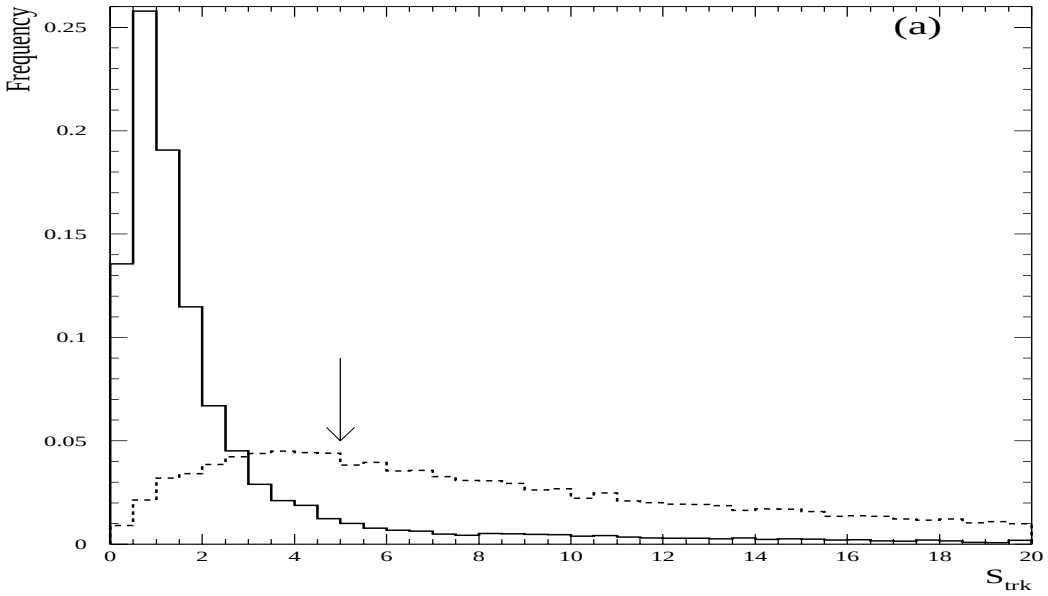

Figure 4.8: Track match significance distribution S_{trk} for electrons from $Z \rightarrow ee$ candidates(solid) and electrons in multi-jet triggered data (dashed) (Central electrons).

where z_0^{trk}, ρ_0^{trk} and z_0^{cal}, ρ_0^{cal} are the center-of-gravity of the drift chamber track and the calorimeter cluster, respectively. Figure 4.9 illustrates this method to find the vertex. The vertex resolution achieved with this technique can be calculated from

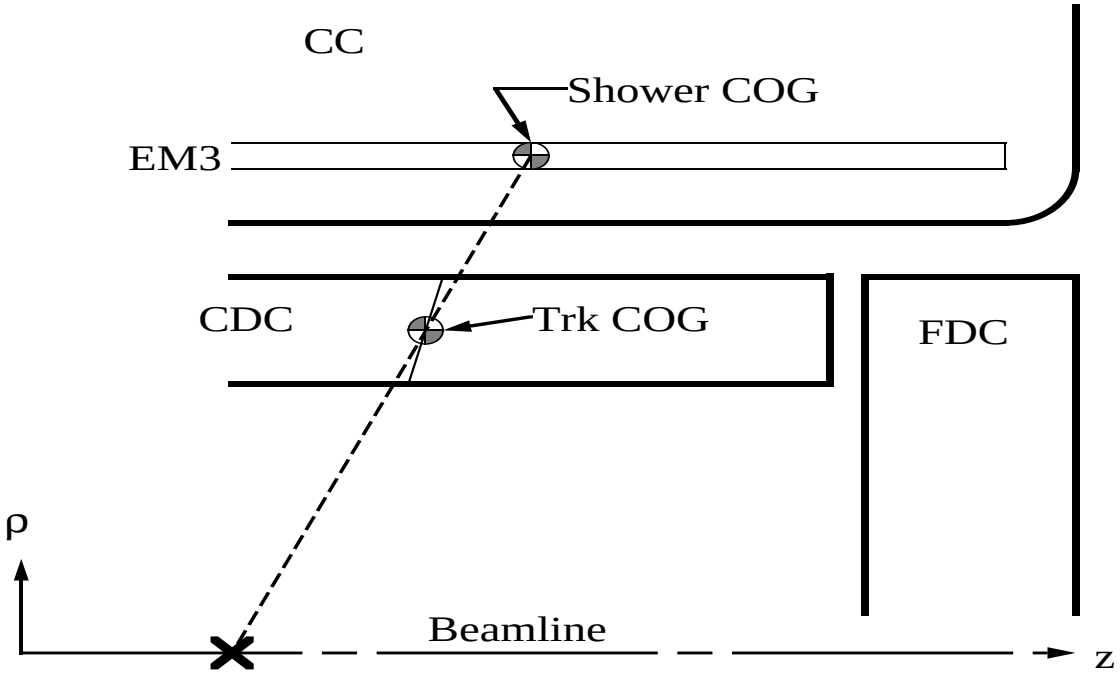

Figure 4.9: Vertex position finding by cluster-track projection method.

$Z \to ee$ events where the single electron vertex resolution, σ_z, is given by:

$$\sigma_z = \frac{1}{\sqrt{2}}\sigma(z_1 - z_2) \tag{4.34}$$

under the assumption that the z-intercepts z_1 and z_2 of the two electrons electrons are uncorrelated. The distribution of $(z_1 - z_2)$ is shown in figure 4.10; the corresponding resolution is $\sigma_z = 1.9$ cm.

Of even greater importance than the possible improvement in the vertex resolution is the dependence of the vertex resolution on instantaneous luminosity. At high luminosity, a higher track multiplicity leads to a larger probability of the RECO vertex being mismeasured (here defined as being off by more than 10 cm from the electron vertex which occurs 13% of the time in the inclusive Z sample). (See figure 4.11). It is not possible to calculate an analogous quantity for the CLUS

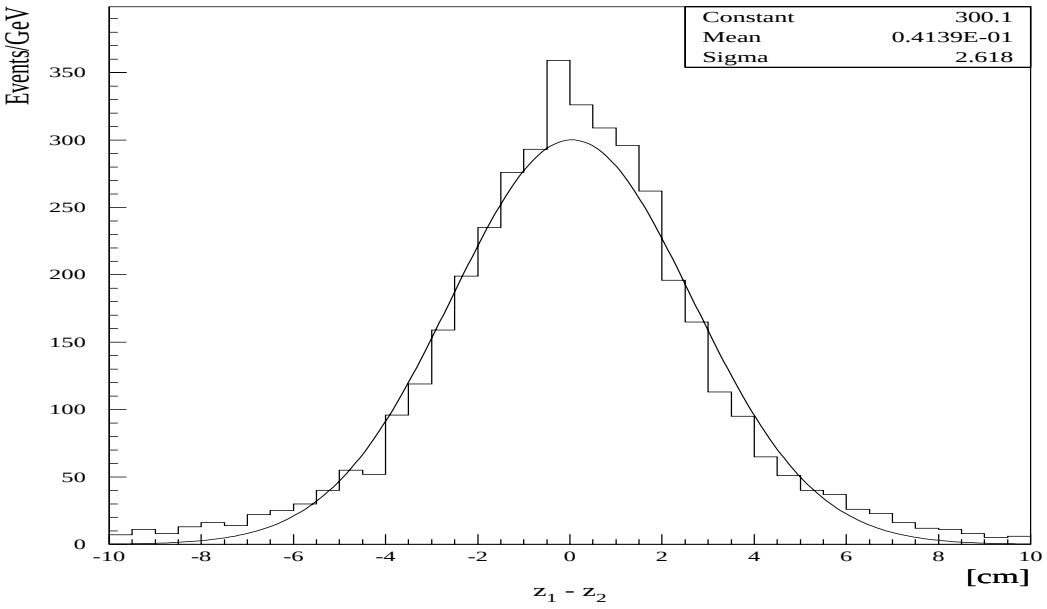

Figure 4.10: Distribution of $(z_1 - z_2)$ for $Z \to ee$ events.

vertex because the "true" vertex is not known, but the difference of the vertices calculated from each of the two electrons can serve as a reference. The latter quantity is much less luminosity dependent which shows that the CLUS vertex is more robust in a high luminosity environment. The transverse mass distribution in the events gets smeared out if the vertex is mismeasured as shown in figure 4.11.

4.7.6 Combining The Four EM Identification Cuts: The Four Variable Likelihood

Better background rejection while maintaining high electron selection efficiency can be obtained by combining the individual electron identification variables into a likelihood test [42, 43]. A probability ratio using a Neyman-Pearson test for two hypotheses H, signal $(H = e)$ and background $(H = b)$ is defined as:

$$\mathcal{R}(f_h) \equiv \frac{p(x|b)}{p(x|e)} = \frac{f_h p(x|h) + (1 - f_h)p(x|ee)}{p(x|e)} \tag{4.35}$$

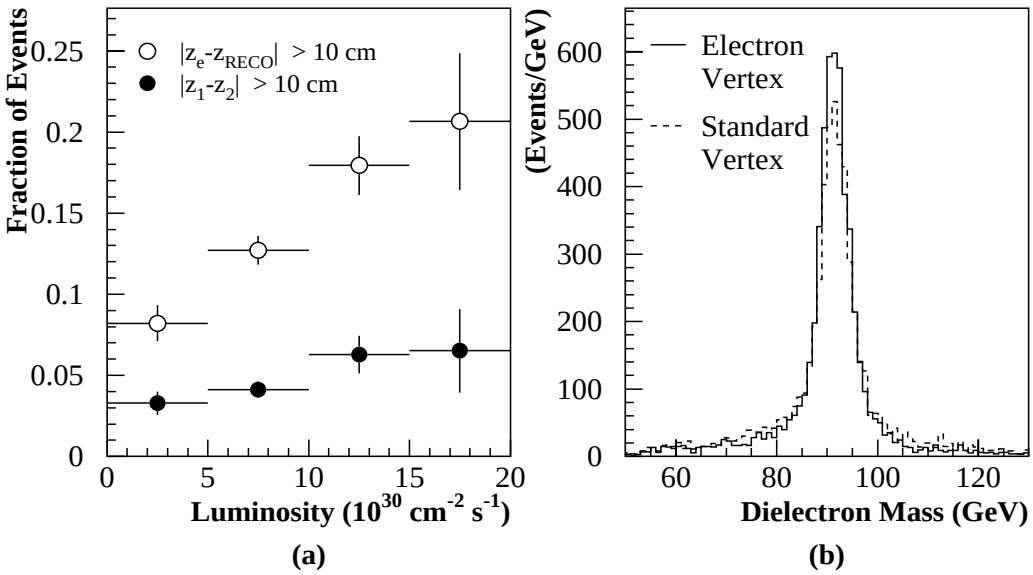

Figure 4.11: (a) Frequency at which the RECO vertex is mismeasured as a function of instantaneous luminosity. To be compared to the frequency at which the vertices obtained by projecting the two electrons into the beamline are more than 10 cm apart. (b)Invariant mass distributions for $Z \to ee$ events for the two vertex methods.

where x is an observable and $p(x|H)$ is the probability density for x given H is true. The background consists of two components, conversions ($H = ee$) and hadron overlaps ($H = h$) with fraction f_h of hadron overlaps in the background. A candidate EM cluster is considered an electron if $\mathcal{R} < k$ where k is chosen to select the desired efficiency and background rejection for a specific analysis. The probability density is calculated by forming the joint likelihood of the four variables CDC dE/dx, H-matrix χ^2, track match significance σ_{trk}, and EM energy fraction f_{EM}:

$$p(x|H) = p_1(dE/dx|H) \times p_2(\chi^2|H) \times p_3(\sigma_{trk}|H) \times p_4(f_{EM}|H) \tag{4.36}$$

It should be noted that a five variable likelihood is used by some analyses which includes the TRD efficiency in addition to the four variables used above. Although this might in principle yield even better background rejection, the five variable likelihood is not used in this analysis since the TRD information is not available at the μDST level and remaking the QCDWZ ntuple [44] this analysis is based on from DST's would have taken too long. To reduce the QCD background to a low level even at large transverse momentum, a rather tight cut on the 4-variable likelihood of 0.25 is imposed.

4.8 Event Displays

To get a feeling for what a typical W boson event looks like, we include events displays for three different candidate events. Figure 4.12 shows a W candidate in the end view. A well-collimated electromagnetic energy cluster can be seen as well as large missing E_T. Figure 4.13 shows another candidate event in the $\eta - \phi$ view. A W + 1 jet event is shown in figure 4.14. In addition to the electromagnetic object and missing E_T a jet is present that deposits a large fraction of its energy in the hadronic part of the calorimeter.

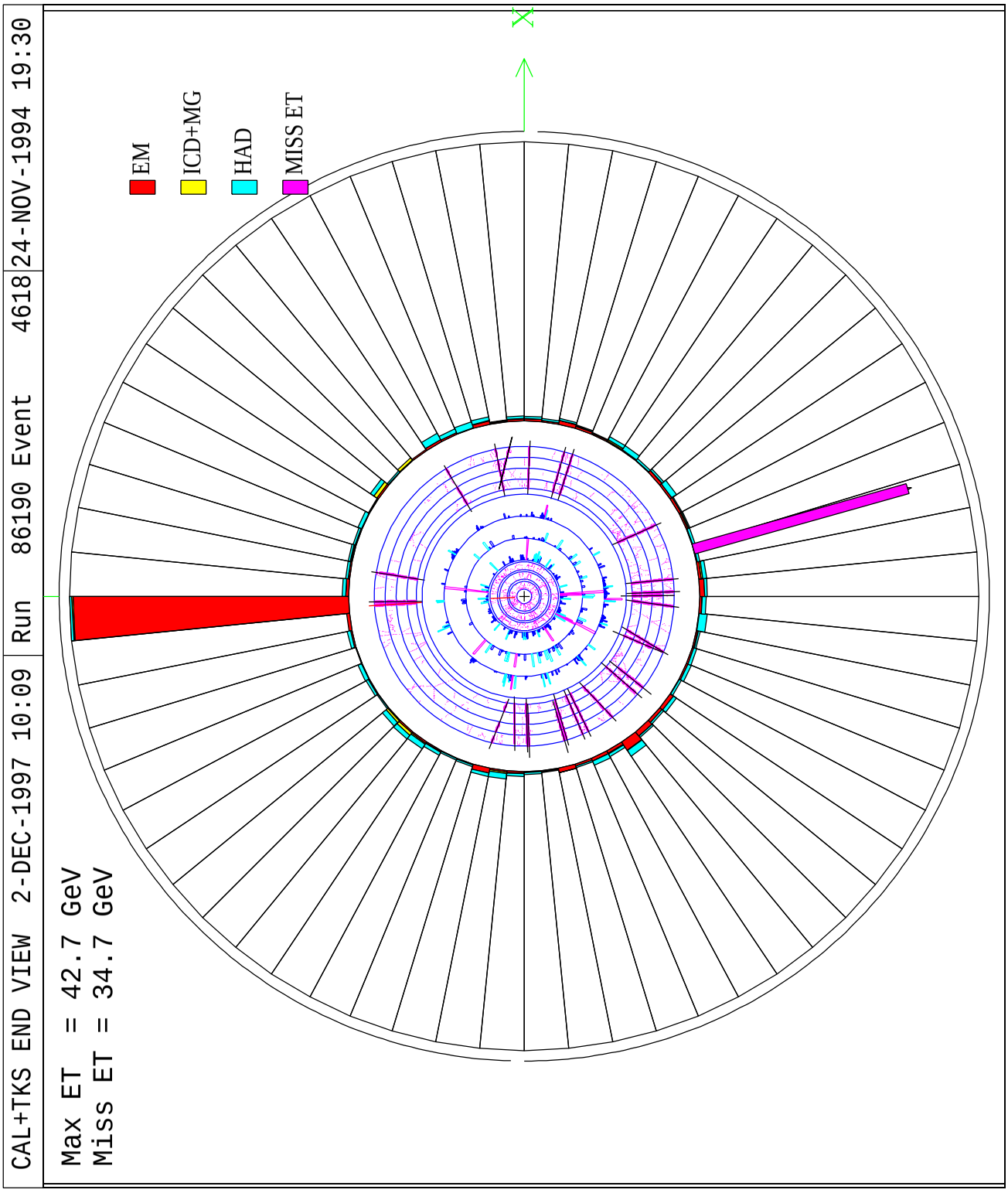

Figure 4.12: W Boson candidate, end view.

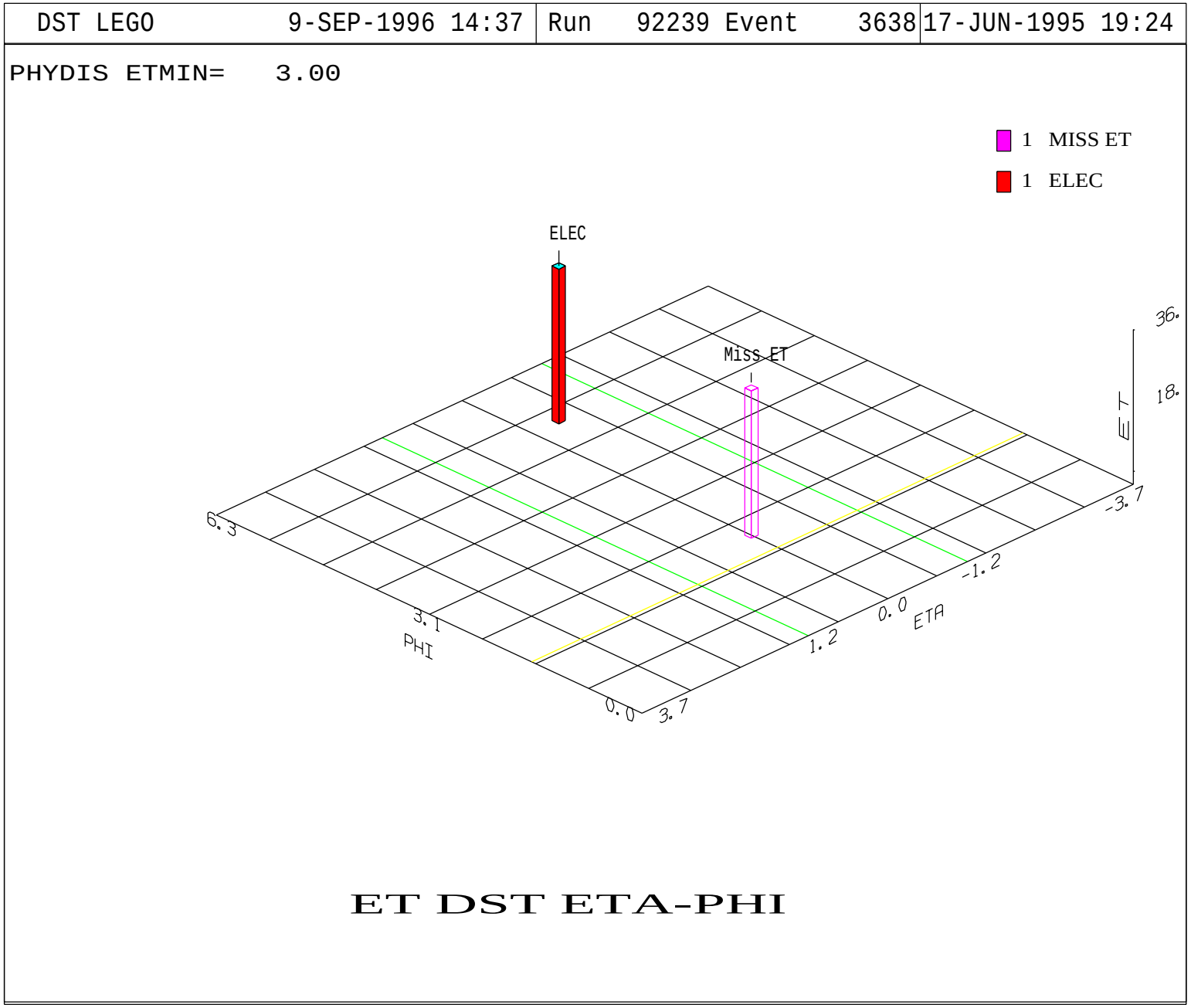

Figure 4.13: W Boson candidate.

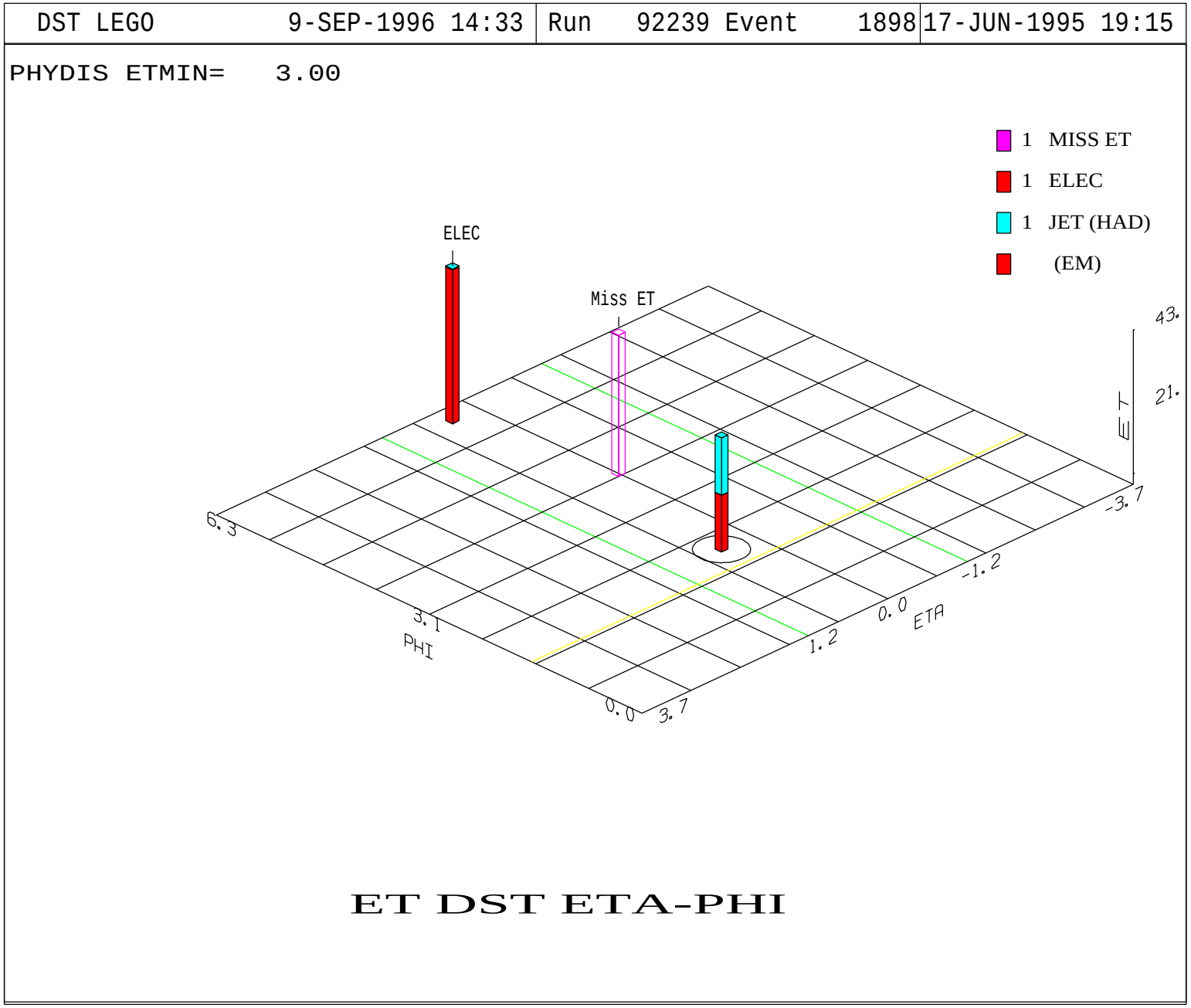

Figure 4.14: W +1 jet candidate.

Chapter 5

The Analysis

5.1 Introduction

The goal of the measurement is to determine the angular distribution of electrons from W decays in the Collins-Soper frame [45]. The Collins-Soper frame is a rest frame of the W boson in which the z-axis bisects the proton and negative antiproton axis. (For a description of the Collins-Soper frame see appendix A). The Collins-Soper frame is chosen for the following reason: Since the longitudinal momentum of the neutrino cannot be measured in a collider experiment, a rest frame of the W boson can never be reconstructed unambiguously. In the Collins-Soper frame, this ambiguity is hidden in the W mass which makes all equations describing kinematic quantities in this frame particularly simple.

The angular distribution of decay electrons from W bosons is determined by the (V-A) character of electroweak interactions. At higher transverse momentum, however, QCD effects change the direction of the helicity of the W boson with respect to the lab frame which alters the angular distribution so that the (V-A) character becomes hidden. This means that this measurement can serve as a probe

for perturbative QCD independent of inclusive measurements.

Since the transverse mass of the W boson,

$$m_T = \sqrt{2p_T^e p_T^\nu \left[1 - cos(\phi^e - \phi^\nu)\right]} \tag{5.1}$$

is correlated with the decay angle of the lepton (see equation 5.4), QCD effects introduce a systematic shift to the W mass measurement at DØ. In the W mass measurement, fits to the transverse mass are used to determine the W invariant mass [46, 47]. The shift is $O(40$ MeV) [48] for events with $p_T \leq 15$ GeV used in the mass measurement. In Run II, when the total error of the W mass will be reduced from the current 105 MeV [46, 47] to an estimated 50 MeV (for 1 fb^{-1}) to about 30 MeV (for 10 fb^{-1}) [49], a good understanding of this systematic shift is important.

Next-to-leading order [1] $[O(\alpha_S^2)]$ perturbative QCD predicts the angular distribution to be [7]:

$$\frac{d^3\sigma}{dP_T^2 dy d(\cos\theta^*)} \propto 1 + S \cdot P(W)\, \alpha_1 \cos\theta^* + \alpha_2 \cos^2\theta^* \tag{5.2}$$

where $\alpha_i \equiv \alpha_i(p_T^W, y^W)$; $P(W)$ is the polarization of the spin of the W boson in +z (=proton) direction, S is the W sign, and θ^* is the polar angle of the charged lepton in the Collins-Soper rest frame of the W boson (see appendix A). This has to be compared to (V-A) theory in the absence of QCD which leads to:

$$\frac{d\sigma}{d(\cos\theta^*)} \propto (1 + S \cdot P(W)\, \cos\theta^*)^2 \tag{5.3}$$

which has previously been measured by UA1 [50, 51, 52]. This implies that in the limit of zero transverse momentum, where QCD effects are negligible, α_1 and α_2 have to approach 2 and 1, respectively. Figure 5.1 illustrates why the angular dis-

[1] The effects described here are already noticeable at leading order $[O(\alpha_S)]$ in QCD. The theoretical calculation referenced here is done to $[O(\alpha_S^2)]$, though.

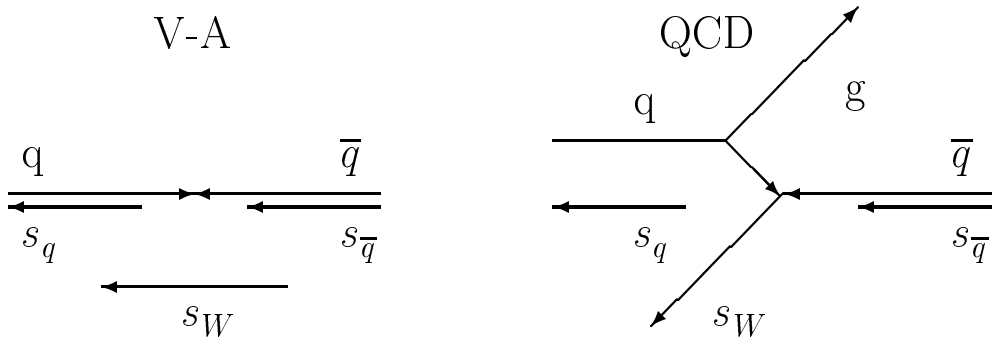

Figure 5.1: Illustration of angular dependence on p_T.

tribution of the electron in W boson decays depends on its transverse momentum. At zero p_T, the spins of the quarks and the W boson are aligned leading to the $(1 \pm \cos\theta^*)^2$ dependence determined by the (V-A) character of electroweak interactions. At finite transverse momentum, which is generated by initial state radiation (ISR) of a gluon or quark jet by one of the incoming particles, the direction of the spin of the W boson changes, which modifies the helicity contributions to the cross section and the angular distribution of the decay electrons. Note that deviations of the angular distribution due to QCD effects are detectable in the Collins-Soper frame because this frame is not a helicity frame. In a frame where the z-axis is collinear to the boson helicity, we would still observe the unaltered $(1 \pm \cos\theta^*)^2$ distribution.

Figure 5.2 (left) shows the dependence of the angular parameters α_1 and α_2 on the transverse momentum of the W boson. In the limit of zero transverse momentum, it approaches unity as predicted by (V-A) theory without higher order QCD corrections. While the angular parameters α_i are initially functions of the transverse momentum of the W boson and its rapidity, the values displayed here are integrated over all rapidities. If α_2 varied considerably with rapidity, the effects

of limited acceptance had to be taken into account when calculating the expected α_2. This is not the case, however.

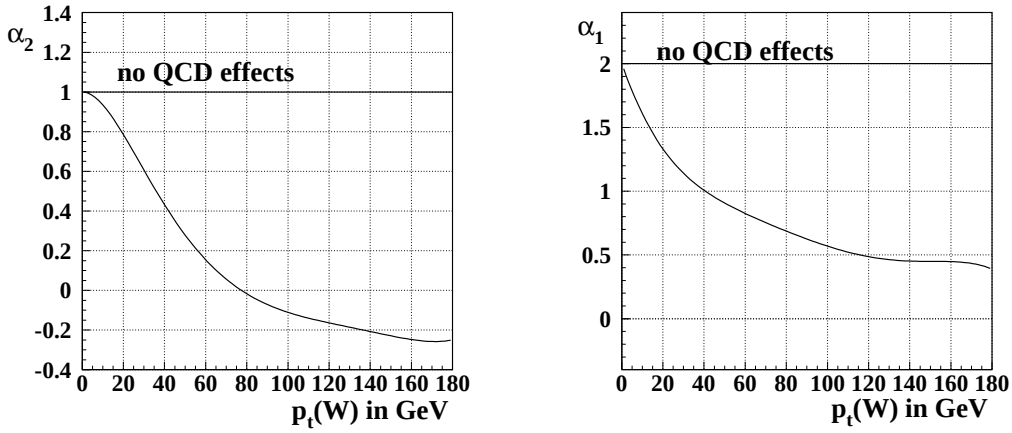

Figure 5.2: The angular parameters α_2 (left) and α_1 (right) as a function of p_T^W.

Since the DØ detector in Run 1 does not have a magnetic field in the tracking detectors, it is not possible to identify the sign of the electron. Without sign identification, this analysis can only be performed summing over both W-signs and W-polarizations which implies that the linear term in $\cos\theta^*$ averages to zero in the limit of complete acceptance. After acceptance cuts have been applied, even the sign averaged angular distribution depends on the linear term; but since this is only a second order effect, this measurement is not sensitive to α_1. For this analysis, we therefore fix α_1 to the value predicted by next-to-leading order QCD (see figure 5.2 (right)).

The first measurement of α_2 as a function of p_T was done with Run 1a data [53]. Here we repeat the measurement using data from Run 1b. The major improvements over the original measurement are better statistics by a factor of six, extension of the maximum transverse momentum of the W boson from 30 to 200 GeV and lower backgrounds by a factor of five due to an improved set of cuts and

electron identification techniques. We also use a different technique to extract the angular distribution which does not suffer from the previous problem of events with imaginary solutions for $\cos\theta^*$ being lost. These were events where $p_{T,CS}^{lepton} \geq 0.5 M_W$ which is possible as a result of detector smearing and the fact that a fixed W mass was used; for more details see [53].

5.2 Description of the analysis method

5.2.1 Using Bayesian statistics to extract the lepton angle

To directly measure the decay angle of the electron, $\cos\theta^*$, all momenta in the lab frame have to be known to perform the boost to the Collins-Soper frame. This is not possible, however, since the longitudinal momentum of the neutrino cannot be measured (see section 4.4). A solution to this problem is to use the correlation between $\cos\theta^*$ and the transverse W mass to infer $\cos\theta^*$ on a statistical basis. This is done using a Bayesian approach. For a very comprehensive treatment of Bayesian statistics see [54].

Figure 5.3 generated from the Columbia-Michigan State Monte Carlo (CMS) [46, 55, 56, 57] shows the correlation of the smeared transverse W mass and the true angle $\cos\theta^*$. By correlating the smeared transverse mass as it would be measured in the DØ detector and the true (unsmeared) angle $\cos\theta^*$, the Bayesian analysis described below will yield the unsmeared angular distribution; the angular distribution obtained this way is the distribution for accepted events which is different from the $1 + S \cdot P(W)\,\alpha_1 \cos\theta^* + \alpha_2 \cos^2\theta^*$ for all events. Since the correlation between the angle and the transverse mass depends on the transverse momentum of the W boson, a separate correlation plot will be used for each p_T bin. The correlation does not depend on the angular parameters α_1, and α_2, however, as

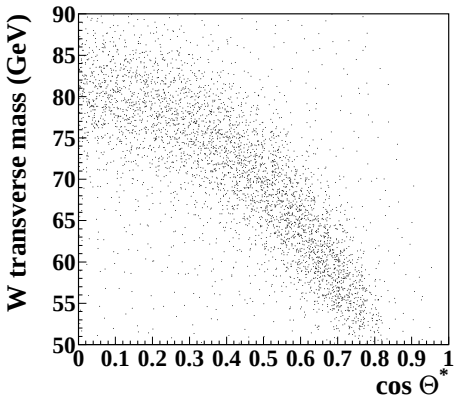

Figure 5.3: Smeared W transverse mass versus $\cos\theta^*$ for $p_T^W \leq 10$ GeV. Acceptance cuts are applied to this plot. This correlation plot is used to infer the $\cos\theta^*$ distribution from the measured m_T distribution.

can be seen from equation 5.4. This equation provides the analytical expression[2] for the dependence of the transverse mass on the angles θ^* and ϕ^* where ϕ^* is the azimuthal angle in the Collins-Soper frame with respect to the x-axis: [53]

$$m_T^W = \frac{m_{e\nu}}{\sqrt{2}} \times \sqrt{2\sqrt{a_0 + a_1\gamma^2 + a_2\gamma^4} - 2(-\sin^2\theta^* + \gamma^2(1 - \cos^2\phi^*\sin^2\theta^*)} \quad (5.4)$$

where the various parameters are defined as:

$$\begin{aligned} \gamma &= \frac{p_T^W}{m_{e\nu}} \\ a_0 &= \sin^4\theta^* \\ a_1 &= 2\sin^2\theta^*(\sin^2\phi^* - \cos^2\phi^*\cos^2\theta^*) \\ a_2 &= (1 - \cos^2\phi^*\cos^2\theta^*)^2 \end{aligned}$$

[2]Please note that this analysis is done integrated over ϕ^*.

To obtain an angular distribution from a measured transverse mass distribution, the transverse mass distribution has to be inverted using the following probability function:

$$f(\cos\theta^*|m_T) = \frac{g(m_T|\cos\theta^*)h(\cos\theta^*)}{\int g(m_T|\cos\theta^*)h(\cos\theta^*)d\cos\theta^*} \tag{5.5}$$

where

- $g(m_T|\cos\theta^*)$ is the probability of measuring m_T given a certain $\cos\theta^*$ value (obtained from the Columbia-Michigan State Monte Carlo (CMS)(see section 5.3))[3];
- $h(\cos\theta^*)$ is the prior probability [4] for $\cos\theta^*$: $(1+\cos^2\theta^*)$. We use the sign averaged value $\alpha_1 = 0$ here;
- $f(\cos\theta^*|m_T)$ is the probability that an event with transverse mass m_T has a decay angle $\cos\theta^*$.

The angular distribution can now be inferred from the measured m_T distribution by integrating $f(\cos\theta^*|m_T)$ over m_T:

$$N_j = \sum_{i}^{all\ m_T\ bins} N_i^{m_T} f(\cos\theta_j^*|m_{Ti}) \tag{5.6}$$

[3]It is important to note that $g(m_T|\cos\theta^*) = \frac{N_{i,j,accepted}}{\sum_j N_{i,j,all}}$ where i is the index for m_T and j for $\cos\theta^*$. The resulting $\cos\theta^*$ distribution will then be the angular distribution for accepted events.

[4]The prior reflects all prior knowledge, i.e. the angular distribution in the absence of QCD effects. Note that it describes the angular distribution before acceptance cuts.

It has been tested that the results of this measurement do not change when a flat prior is chosen. The changes in α_2 are 0.0001, 0.0002, 0.002, and 0.00004, respectively, for the four p_T bins used in this analysis and are negligible compared to the statistical errors.

where N_j is the number of events in $\cos\theta^*$ bin j and $N_i^{m_T}$ is the measured number of events in transverse mass bin i.

To measure the angular parameter α_2, a series of $\cos\theta^*$ templates are generated from Monte Carlo in bins of p_T^W, each normalized to unity. Each of the templates is generated by taking the transverse mass distribution from a high statistics Monte Carlo sample for a specific $\alpha_2$value and converting it into an angular distribution by means of the Bayesian method described previously. Detector effects are included by applying smearing, efficiency, and acceptance corrections in the Monte Carlo program. The angular distribution obtained from data will then be compared to these templates to determine which value for α_2 fits best. Figure 5.4 shows a series of such templates for $p_T^W \leq 10$ GeV. The method is tested with Monte

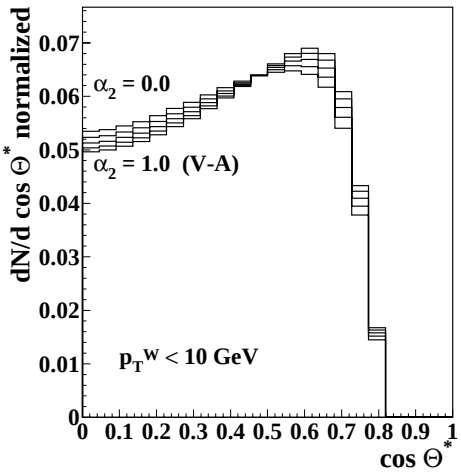

Figure 5.4: Templates of the angular distribution for various α_2 values for $p_T^W \leq 10$ GeV. These templates are obtained from the CMS Monte Carlo after acceptance cuts have been applied which results in the drop-off at small angles.

Carlo. Results are shown in figure 5.5 for unlimited statistics and Figure 5.6 for data statistics. In the limit of infinite statistics, the method described above to invert the transverse mass distribution results in an angular distribution identical to the true angular distribution.

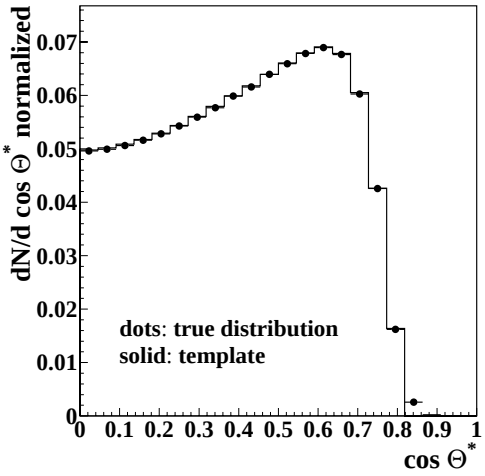

Figure 5.5: Angular distribution for a template as obtained by inverting the transverse mass distribution compared to the true angular distribution for high statistics.

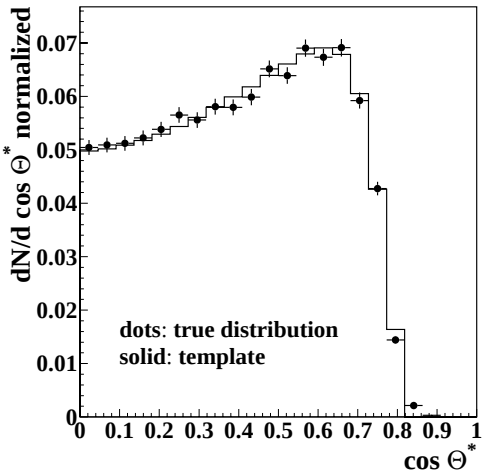

Figure 5.6: The true angular distribution for a Monte Carlo sample with statistics similar to data compared to the same template as above.

Why use Bayesian Statistics?

It would be possible to perform this analysis without the use of Bayesian statistics by simply comparing the measured transverse mass distribution to Monte Carlo

templates. A log-likelihood function could be used to find the transverse mass distribution, corresponding to a certain α_2 value, that fits best, and the two transverse mass distributions that correspond to $\alpha_2 \pm 1\sigma$. We started out using Bayesian statistics since in the beginning it was not clear if one could not improve the sensitivity of this measurement by adding more variables and performing the Bayesian analysis in a multi-parameter space. This would be much harder without the use of Bayesian statistics. Studies showed, however, that the transverse mass is in fact the best single variable and other additional variables like the electron E_T don't improve the sensitivity. Another reason why we kept the Bayesian approach is that it automatically leads to an angular distribution whereas directly comparing the transverse mass to templates would result only in the measurement of the angular parameter α_2.

In principle, it would be desirable to include all backgrounds in the Bayesian analysis and treat them as nuisance parameters. We chose not to perform the analysis this way since the prior probabilities as a function of $\cos\theta^*$ for the backgrounds would be very difficult to determine. This is specially true for the QCD multijet background for which we use a data based technique since no suitable Monte Carlo exists for its estimation.

5.2.2 The log-Likelihood Method

To extract the angular parameter α_2 from the angular distribution obtained by inverting the transverse mass distribution, a log-likelihood method is used:

$$\log \mathcal{L} = \sum_{i=\cos\theta^* \, bins} n_i \log(p_i) \tag{5.7}$$

where p_i is the normalized population of a $\cos\theta^*$ bin for one of the Monte Carlo templates and n_i is the population of the same bin in the angular distribution obtained from data. The statistical errors for α_2 are taken at the points where $\log\mathcal{L}$ drops by 0.5 units: In the case of Gaussian errors, which is approximately

the case here, the s-standard-deviation error can be determined by a contour [1] given by the vector of parameters α' such that

$$\ln \mathcal{L}(\alpha') = \ln \mathcal{L}_{max} - s^2/2 \tag{5.8}$$

Here we use the one standard deviation (s=1). The absolute value of $\log \mathcal{L}$ is meaningless here.

5.2.3 Monte Carlo Sensitivity Studies

Since the number of high p_T W bosons is limited in Run I, it was not clear in the beginning if this measurement would be sensitive enough to distinguish between the next-to-leading order QCD prediction and a theory without QCD effects. In addition, the measurement of the angular distribution is further degraded by the fact that the angle cannot be measured directly but is inferred from smeared out correlation between α_2 and m_T. To decide whether it would be worthwhile repeating this measurement with Run 1b data, a Monte Carlo experiment scaled to Run 1b statistics was performed. Four bins in p_T^W were chosen so that the statistical errors on α_2 in each of the three largest p_T bins would be smaller than the difference between the QCD prediction and the prediction in the absence of QCD. The first bin, covering $p_T \leq 10$ GeV is not sensitive to the difference between both theories since the QCD prediction for α_2 approaches unity for zero p_T. Since this bin actually includes the largest number of events and has the smallest error for α_2, it can serve as an indicator if this method works correctly: The result for α_2 should be one within the error.

Figure 5.7 shows the transverse momentum and transverse mass distribution for central Run1b W events on which this Monte Carlo study is based. The results of such a Monte Carlo measurement are summarized in table 5.1 and in figure 5.9.

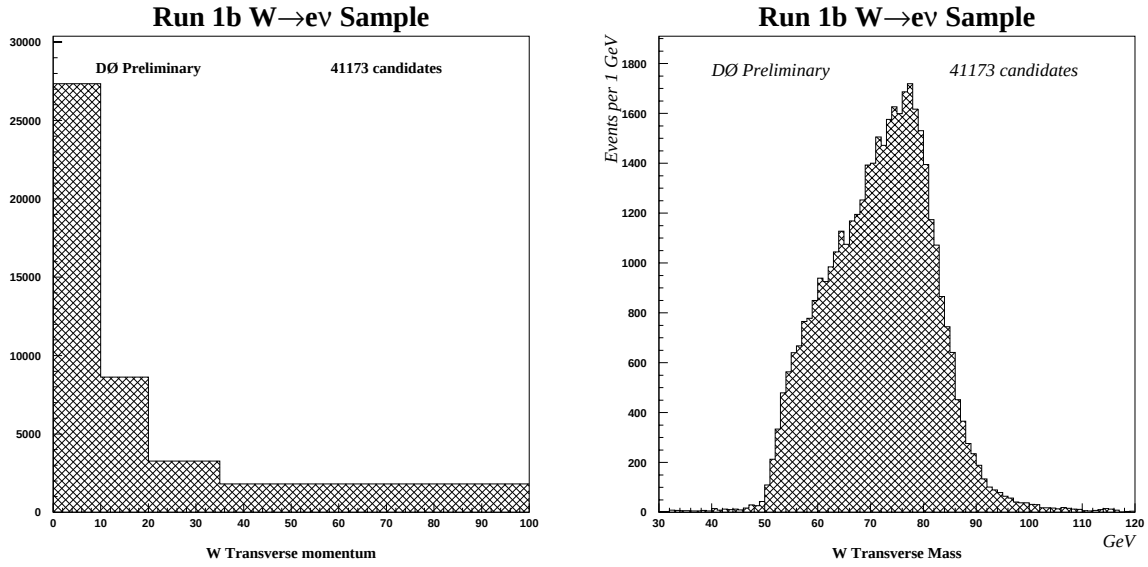

Figure 5.7: W transverse momentum in GeV (left) and transverse mass in GeV (right).

p_T(W)	$\overline{p_T^W}$	events	$\alpha_{2,theor}$	α_2
0.0 - 10.0	4.44	26570	0.986	0.99 $\pm$ 0.12
10.0 - 20.0	12.58	8177	0.902	0.80 $\pm$ 0.23
20.0 - 35.0	25.66	2961	0.685	0.79 $\pm$ 0.37
35.0 - 200.0	53.54	1312	0.232	0.28 $\pm$ 0.43

Table 5.1: Expected and measured α_2 for the p_T^W ranges used in this analysis for one particular Monte Carlo run.

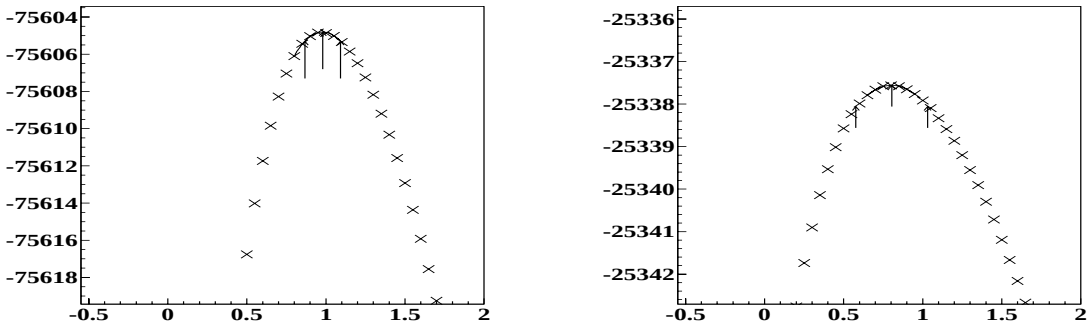

Figure 5.8: Log likelihood as a function of α_2 for $p_T \leq 10$ GeV (left) and 10 GeV $\leq p_T \leq 20$ GeV (right).

Figure 5.8 shows the log-likelihood distributions for two p_T bins. The 1 σ statistical errors are determined by the α_2 values where $\log \mathcal{L}$ drops by 0.5 units. To estimate the average sensitivity expected, ten statistically independent Monte Carlo experiments each performed with statistics scaled to the number of W events in Run I were performed. Table 5.2 summarizes the average χ^2 with respect to the next-to-leading order QCD calculation by Mirkes and the (V-A) theory prediction, respectively, for these ten experiments. The confidence limits are derived from these χ^2-values.

	Mirkes	(V-A)	(V-A) - Mirkes
average χ^2	3.1	10.7	7.6
average C.L.	0.54	0.03	0.11

Table 5.2: Sensitivity for 10 MC experiments. The average χ^2 is shown with respect to the next-to-leading order QCD calculation and with respect to the $(V-A)$ prediction in the absence of QCD effects.

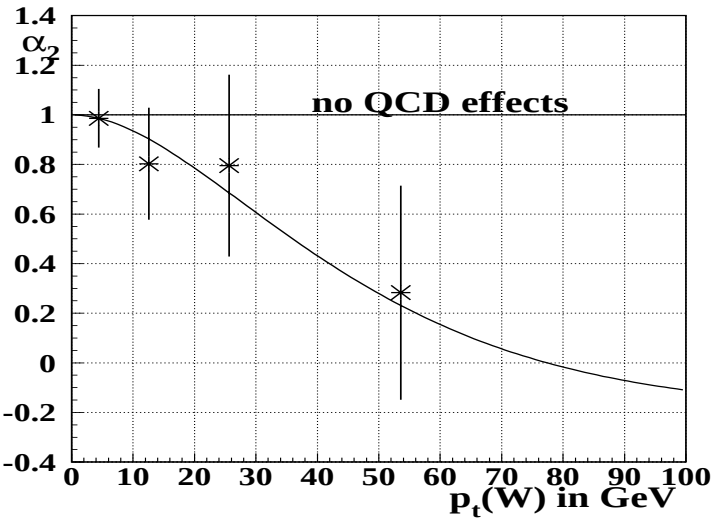

Figure 5.9: Most likely α_2 values and 1 σ errors for a specific MC run.

Conclusion of Monte Carlo Sensitivity Studies

Monte Carlo studies scaled to Run 1b statistics indicate that we should be able to distinguish between next-to-leading order QCD and (V-A) theory without QCD effects to $\approx$1.5 - 2.0 σ using the Bayesian method described above. Although the statistical power of this measurement is not as good as one would hope for, it is still worthwhile repeating this experiment since the angular distribution of electrons in W boson decays has never been measured with a data set this large. The Fermilab Tevatron is currently the only collider in the world that can produce a large number of high p_T W bosons.

5.3 The CMS Monte Carlo Program

The kinematics of W boson production and decay are simulated using the fast Columbia-Michigan State (CMS) Monte Carlo generator [46]. CMS was initially written at DØ for the W mass analysis and has since been used in the measurement of the inclusive W and Z cross section, and the measurement of the transverse mass

distribution for the W and the Z boson.

CMS is not a full parton level generator, kinematic distributions for various processes have to be produced using a full triple differential cross section generator like Resbos [3]. The parton level boson cross section enters CMS as a grid (see appendix B) of boson rapidity versus transverse momentum. The invariant W mass enters CMS as a Breit-Wigner function that depends on the center-of mass s of the quark-antiquark system. CMS subsequently decays the boson and smears the resulting particles by taking into account detector resolution effects. Acceptance effects are modeled by a parameterized detector simulation. A detailed description of the CMS Monte Carlo program is given in [55, 56, 57]. In the following sections we discuss the generation and decay of W bosons in CMS in some detail with special emphasis on the parameters that had to be tuned for this analysis.

5.3.1 W Boson Generation

Ideally, vector boson production is modeled by a fully differential cross section:

$$\frac{d^5\sigma}{dm dp_T dy d\phi d\epsilon} \tag{5.9}$$

where m, p_T, y, ϕ, and ϵ are the vector boson mass, transverse momentum, rapidity, azimuthal angle, and polarization, respectively. In the CMS Monte Carlo, this cross section is factorized into four pieces:

$$\frac{d^5\sigma}{dm dp_T dy d\phi d\epsilon} = \frac{d\sigma}{dm} \cdot \frac{d^2\sigma}{dp_T dy} \cdot \frac{d\sigma}{d\phi} \cdot \frac{d\sigma}{d\epsilon} \; . \tag{5.10}$$

This factorization is not strictly correct, but correlations between the various terms are small. The ϕ-term is simple: Vector bosons are produced uniformly in ϕ so that CMS just picks a random ϕ value in $[0, 2\pi]$.

The polarization of a W boson is defined by its charge. In the case of W^+ production, two cases have to be considered: If the u and the $\overline{d}$ quark come from the valence contents of the proton or antiproton, respectively, the W^+ is polarized

opposite to the proton direction. If both quarks come from the sea content, on the other hand, two polarizations can occur. In 1/2 of these interactions, which occur 20% of the time, the polarization of the W will be reversed. For more details on this see appendix B.

The other two parts of the cross section in equation 5.10 will be discussed below.

5.3.2 Boson Mass

The W mass is modeled by a relativistic Breit-Wigner with an $\hat{s}$- dependent width modified by a parton luminosity term, which models the dependence of the mass on the momentum distribution of the quarks:

$$\frac{d\sigma}{dm} = PL(m) \cdot \frac{m}{(m^2 - M^2)^2 + m^4, \, ^2/M^2} \ , \tag{5.11}$$

where $PL(m)$ is the parton luminosity term, m is the mass of the vector boson being generated, and M and , are the boson's true mass and natural width, respectively.

$PL(m)$ depends on the structure function and is well modeled by the following function:

$$PL(m) = \frac{e^{-\beta \cdot m}}{m} \ , \tag{5.12}$$

where the parton luminosity slope β is obtained by fitting equation 5.11 to the invariant mass distribution from `HERWIG` [58] W events (see figure 5.10). Without the parton luminosity term, figure 5.10 would be symmetric; the momentum distribution of the quarks biases the mass towards lower values.

5.3.3 Transverse Momentum and Rapidity

As already discussed in chapter 2, at lowest order the W boson is produced through a Drell-Yan diagram as shown in figure 5.11. W bosons produced this way have

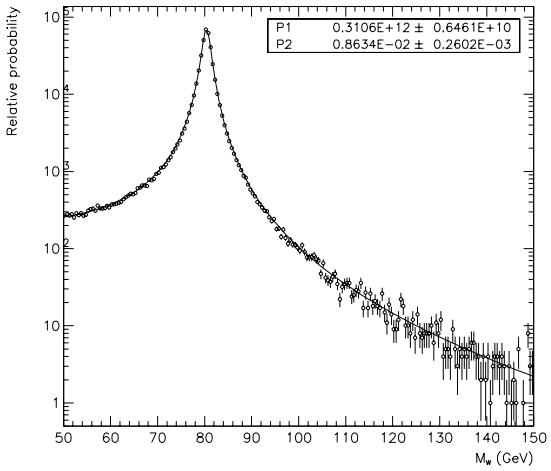

Figure 5.10: Mass distribution from HERWIG showing the parton luminosity effect [56, p. 68].

longitudinal momentum due to the momentum imbalance of the incoming quarks but no transverse momentum since the momenta of the proton and antiproton are collinear with the beam axis. The fact that W bosons are produced with finite transverse momentum is attributed to contributions from higher order diagrams as shown in figure 5.12. The additional quark- or gluon-jet recoils against the W boson and carries away transverse momentum equal and opposite to p_T^W.

In CMS, the W p_T and rapidity y are generated according to theory calculations including perturbative and non-perturbative effects. For large p_T^W (above 50 GeV), fixed order perturbation theory describes the production of vector bosons well. A calculation to next-to leading order ($\mathcal{O}[\alpha_S^2]$) in perturbative QCD by Arnold and Reno [59] is used in this regime. For $p_T^W < 20$ GeV, a resummed calculation (see chapter 1) by Ladinski and Yuan [60] is used. The p_T distributions for both theories are matched at intermediate p_T^W to ensure a smooth transition.

The resummed calculation by Ladinski and Yuan is performed in impact pa-

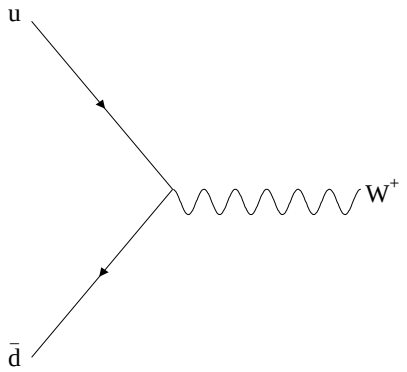

Figure 5.11: Lowest order (Drell-Yan) diagrams for W production.

rameter space where the impact parameter b is the Fourier-transformed variable to p_T. The double differential cross section for vector boson production is written as:

$$\frac{d^2\sigma}{dp_T dy} \propto \int \frac{d^2b}{(2\pi)^2} e^{i\vec{b}\cdot\vec{p_T}} W(b_\star) e^{-S_{NP}(b)} \ , \tag{5.13}$$

where $b_\star$ is a function of b which handles the divergence at large b or small p_T by introducing a cutoff b_{max}:

$$b_\star = \frac{b}{\sqrt{1 + b^2/b_{max}^2}} \ . \tag{5.14}$$

The function $W(b_\star)$ describes the perturbative part of the calculation while non-perturbative effects at large B are contained in the function $S_{NP}(b)$, which in the parameterization used by Ladinski and Yuan is written as:

$$S_{NP} = g_1 b^2 + g_2 b^2 \ln\left(\frac{Q}{2Q_\circ}\right) + g_1 g_3 \ln(100 x_A x_B) \ , \tag{5.15}$$

with $Q_\circ$ an arbitrary momentum scale, Q the mass of the vector boson, and x_A, x_B the momentum fractions of the incoming quarks. The parameters g_1, g_2, and g_3

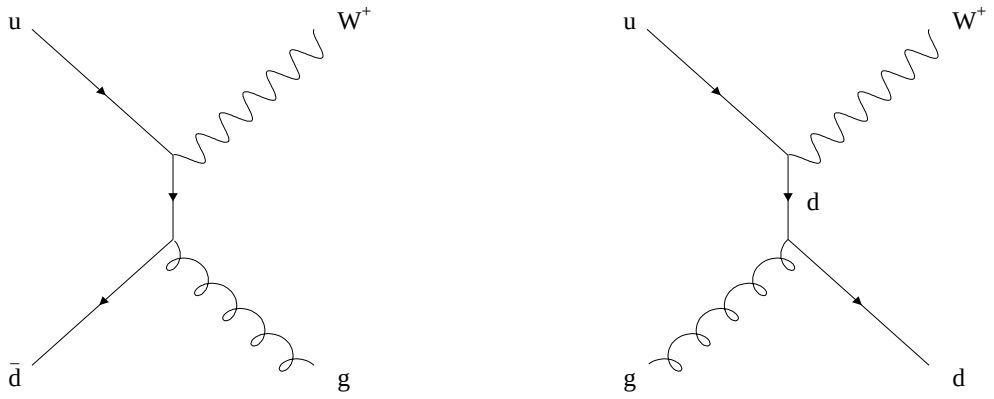

Figure 5.12: Higher order diagrams for W production: (left) the initial state gluon radiation process and the (right) Compton process.

are determined by Ladinsky and Yuan. They fit their hypothesis to the available Drell-Yan and Z production data and obtain the values:

$$g_1 = 0.11^{+0.04}_{-0.03}\,\mathrm{GeV}^2 \qquad g_2 = 0.58^{+0.1}_{-0.2}\,\mathrm{GeV}^2 \qquad g_3 = -1.5^{+0.1}_{-0.1}\,\mathrm{GeV}^{-1}\,, \qquad (5.16)$$

where $Q_\circ = 1.6$ GeV, and $b_{max} = 0.5$ GeV^{-1} are chosen. It has been shown [56] that g_2 is the dominant parameter. The above value for g_2 is found to agree well with DØ $Z \to ee$ data [61].

5.3.4 W Boson Decay

The decay of the W boson is performed in the Collins-Soper rest frame of the W. Since the leptons can be treated as massless particles, they are produced back-to-back in the rest frame. Each lepton is produced with momentum equal to 1/2 the boson mass. Figure 5.13 shows the leading order diagram for $W \to e\nu$ decay.

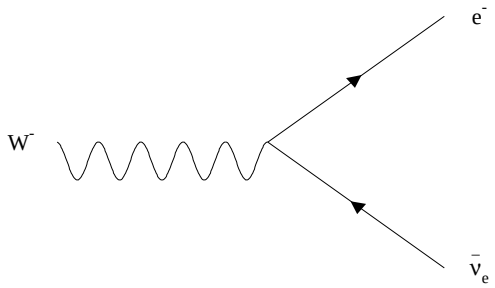

Figure 5.13: Leading order diagrams for $W \to e\nu$ decays.

The decay angle of the lepton is generated in the Collins-Soper frame according to Mirkes calculation [7] (see equation 5.2). Subsequently, the boost to the lab frame is performed.

5.3.5 QED radiative Decays

Final state radiation (Bremsstrahlung) of a photon from the decay electron is a correction to the lowest order decay process that has to be taken into account since the photon can lower the momentum of the electron. A calculation by Berends and Kleiss [62] to $\mathcal{O}[\alpha_{EM}]$ concludes that in 31% of the W decays, a photon with energy above 50 MeV is radiated. In CMS, these photons are generated for the correct fraction of events, subsequently the electron, the neutrino, and the photon are boosted into the lab frame. If the electron and photon are close in $\eta \times \phi$ space ($\mathcal{R} = \sqrt{\Delta\phi^2 + \Delta\eta^2} < 0.3$), they are merged, otherwise the photon is treated as a

separate object.

5.3.6 $W \to \tau\nu \to e\nu\nu$

$W \to \tau\nu$ decays where the tau subsequently decays electronically are indistinguishable from $W \to e\nu$ events: Both are characterized by an electron and large missing E_T in the final state. The CMS Monte Carlo produces $W \to \tau\nu \to e\nu\nu$ events a fraction of the time to account for this production mode. The production kinematics for $W \to \tau\nu$ events are exactly the same as the ones for $W \to e\nu$. Kinematic differences come in through the subsequent three body decay $\tau \to e\nu\nu$, which is performed in the rest frame of the τ. The energy and angular correlations of the electron with respect to the τ polarization vector are correctly taken into account by selecting them from a two-dimensional distribution obtained from $\tau \to e\nu\nu$ decays generated with the ISAJET [63] Monte Carlo.

5.3.7 Electromagnetic Scale and resolution

The response of the electromagnetic calorimeter is determined from test beam data and parameterized as:

$$E^{\text{true}} = \alpha E^{\text{meas}} + \beta \,, \tag{5.17}$$

where α is the electromagnetic scale and β is the offset. The offset is determined from low energy J/ψ [64] and π^0 [65] resonances. The parameters are found to be $\alpha = 1.072$ and $\beta = -0.158$ GeV. Since scale corrections are applied to the data, α and β are set to 1.0 and 0.0 in CMS, respectively. The error on α is taken to be 0.0008 [46].

5.3.8 Hadronic Scale

The scale of the measured recoil momentum[5] differs from the electron energy scale because the recoil measurement also includes energy from hadronic showers and suffers from the loss of energy in uninstrumented regions of the calorimeter [46].

The response of the hadronic calorimeter relative to the response of the electromagnetic calorimeter was determined using $Z \rightarrow ee$ events, where the transverse momentum of the Z boson can be obtained from either the measurement of the transverse momentum of the two electron system ($\vec{p}_T^{\,ee}$) or from the recoil activity [6] in the event ($-\vec{p}_T^{\,rec}$). To minimize the effects of the energy resolution in the determination of the hadronic energy scale relative to the electromagnetic energy scale, the momentum imbalance was measured with respect to the (η, ξ)-coordinate system [46] (See figure 5.14). The η axis is defined as the bisector of the two electron transverse directions and the ξ-axis as the direction perpendicular to η. Since the momenta are projected onto an axis that is independent of any energy measurement, noise contributions to the momenta average to zero and do not bias the result. The η imbalance is then defined as

$$\eta_{imb} \stackrel{\text{def}}{=} \vec{p}_T^{\,ee} \cdot \hat{\eta} + \vec{p}_T^{\,rec} \cdot \hat{\eta} \tag{5.18}$$

where $\hat{\eta}$ is a unit vector along the η axis. If the electromagnetic and hadronic responses are equal, η_{imb} is zero. Since the positive η axis is always in the direction of $\vec{p}_T^{\,ee}$, any systematic bias in the measurement of $\vec{p}_T^{\,rec}$ will manifest itself as a bias in η_{imb}.

To determine the functional dependence of the recoil system with respect to the dielectron system, $\vec{p}_T^{\,rec} \cdot (-\hat{\eta})$ is plotted as a function of $\vec{p}_T^{\,ee} \cdot \hat{\eta}$ as shown in figure 5.15. It was found that for $p_T > 10$ GeV the hadronic response is well

[5] The content of the following two subsections is also described in [66].

[6] The p_T^W is measured from the recoil.

described by a linear scale and offset:

$$p_{T,\eta}^{rec} = \alpha_H \; p_{T,\eta}^{ee} + \beta_H \tag{5.19}$$

where $p_{T,\eta}^{rec} \stackrel{\text{def}}{=} \vec{p}_T^{\,rec} \cdot \hat{\eta}$ and $p_{T,\eta}^{ee} \stackrel{\text{def}}{=} \vec{p}_T^{\,ee} \cdot \hat{\eta}$. The parameters α_H and β_H are determined by a least-square fit to the data.

For small p_T values ($p_T < 10$ GeV), however, the relation between the hadronic and electronic recoil is better described by a logarithmic function [46]:

$$p_{T,\eta}^{rec} = \left(\gamma_H \ln(p_{T,\eta}^{ee}) + \delta_H\right) p_{T,\eta}^{ee} \tag{5.20}$$

The parameters γ_H and δ_H are determined by a least-square fit to the data in the low p_T region (see figure 5.16). A logarithmic function also describes the jet energy response of the DØ calorimeter. We get the following parameters with their respective errors from the fits:

α_H	β_H	γ_H	δ_H
0.972 ± 0.0095	-1.21 ± 0.14	0.099 ± 0.019	0.620 ± 0.047

Table 5.3: Hadronic response parameters and their errors.

The contribution from the underlying event does not affect the determination of the scale since it is distributed randomly with respect to the η direction.

Correcting the hadronic recoil momentum by the energy scale factor $R_{rec} = \alpha_H + \beta_H / p_T^{ee}$ and $R_{rec} = \gamma_H \ln(p_T^{ee}) + \delta_H$, respectively, the η imbalance is defined as:

$$\eta_{imb}^{corrected} = \vec{p}_T^{\,ee} \cdot \hat{\eta} + (\vec{p}_T^{\,rec} / R_{rec}) \cdot \hat{\eta} \tag{5.21}$$

Figure 5.17 shows the result of the corrected η imbalance. The distribution of the η imbalance is well described by a Gaussian distribution with a width of (4.14 ± 0.12) GeV. This value is in good agreement with previous values (4.2 GeV in reference [46]).

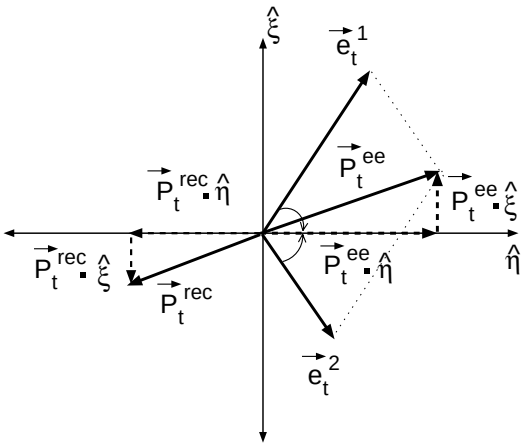

Figure 5.14: Definition of the η–ξ coordinate system in a Z boson event. The η axis is the bisector of the electrons in the transverse plane; the ξ axis is perpendicular to η [55, p. 46].

Dependence of the Hadronic Scale on Cafix Energy Scale Corrections

`CAFIX` [67, 68] is a package developed at DØ to perform energy scale corrections to electromagnetic objects and to hadronic jets. These energy scale corrections are subsequently used to correct the missing E_T of the event. The cafix corrected missing E_T is called PNUT4 whereas the uncorrected missing E_T is called PNUT2. This analysis uses PNUT4 because it is closer to the true missing E_T at high p_T. Former analyses like the measurement of the transverse momentum spectrum for Run1A and the angular distribution of electrons from W bosons for Run1A were performed using PNUT2. The reason why the hadronic scale for PNUT4 is still less than one is that cafix only corrects clustered energies like jets. An even better algorithm that would perform cell-by-cell corrections would be expected to render a scale very close to unity. It would be impracticable to perform corrections on all the calorimeter cells, however correcting clusters is a good approximation.

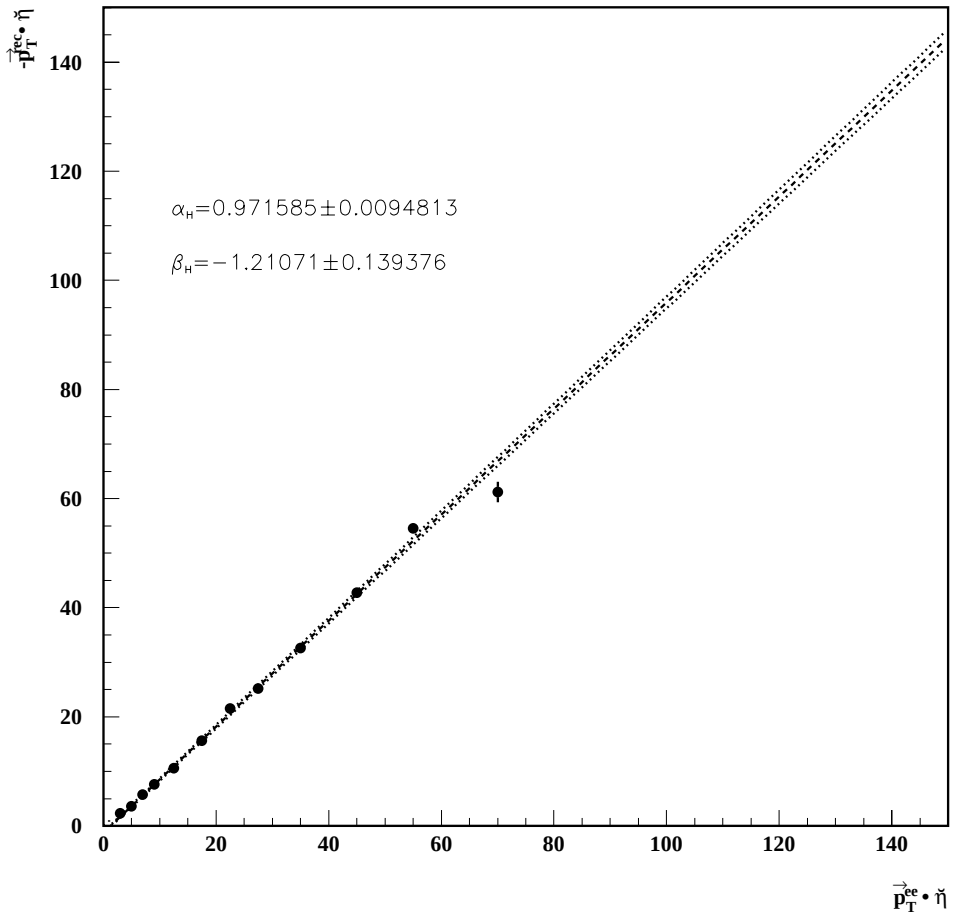

Figure 5.15: For $Z \to ee$ events (points) the average value of $\vec{p}_T^{\,rec} \cdot (-\hat{\eta})$ is shown versus $\vec{p}_T^{\,ee} \cdot \hat{\eta}$ (both in GeV). The line shown is obtained from a linear least squares fit to the data. The dotted lines represent the statistical uncertainties from the fit.

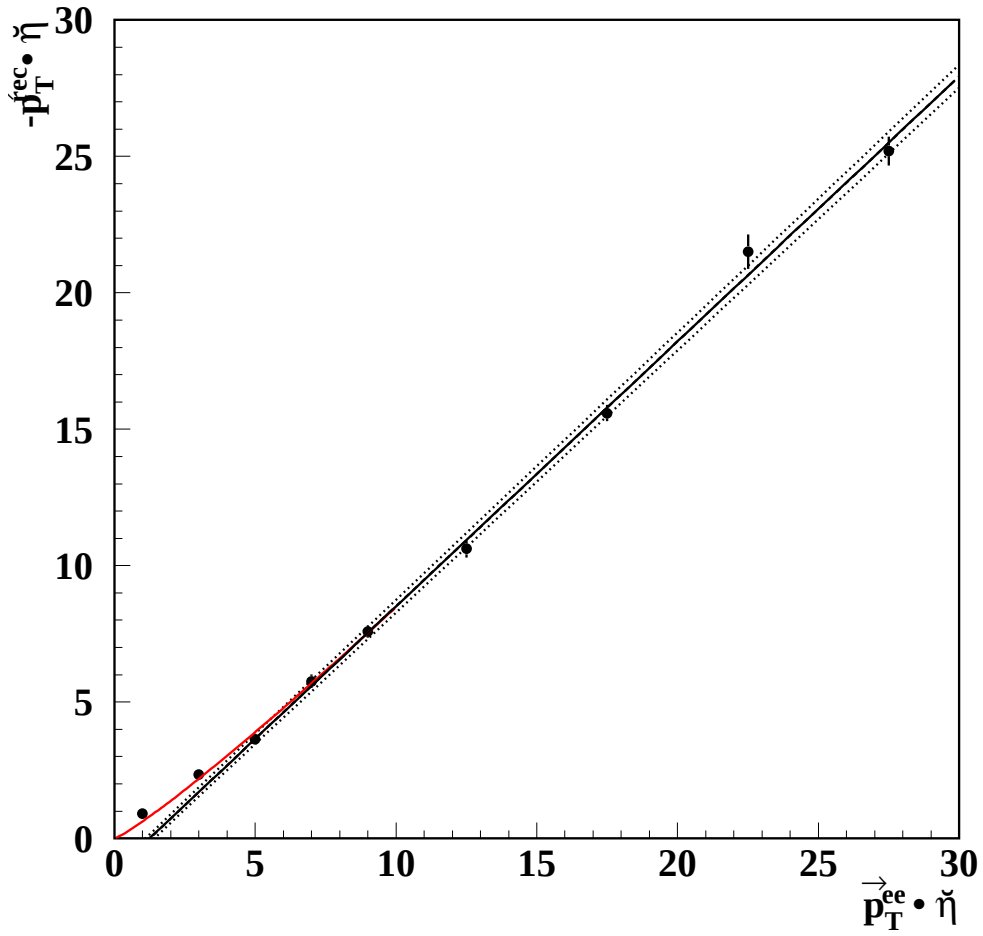

Figure 5.16: For $Z \to ee$ events (points) the average value of $\vec{p}_T^{\,rec} \cdot (-\hat{\eta})$ is shown versus $\vec{p}_T^{\,ee} \cdot \hat{\eta}$ (both in GeV). Shown is the linear fit valid at $p_T > 10$ GeV and a logarithmic fit valid for $p_T < 10$ GeV. The dotted lines represent the statistical uncertainties from the linear fit.

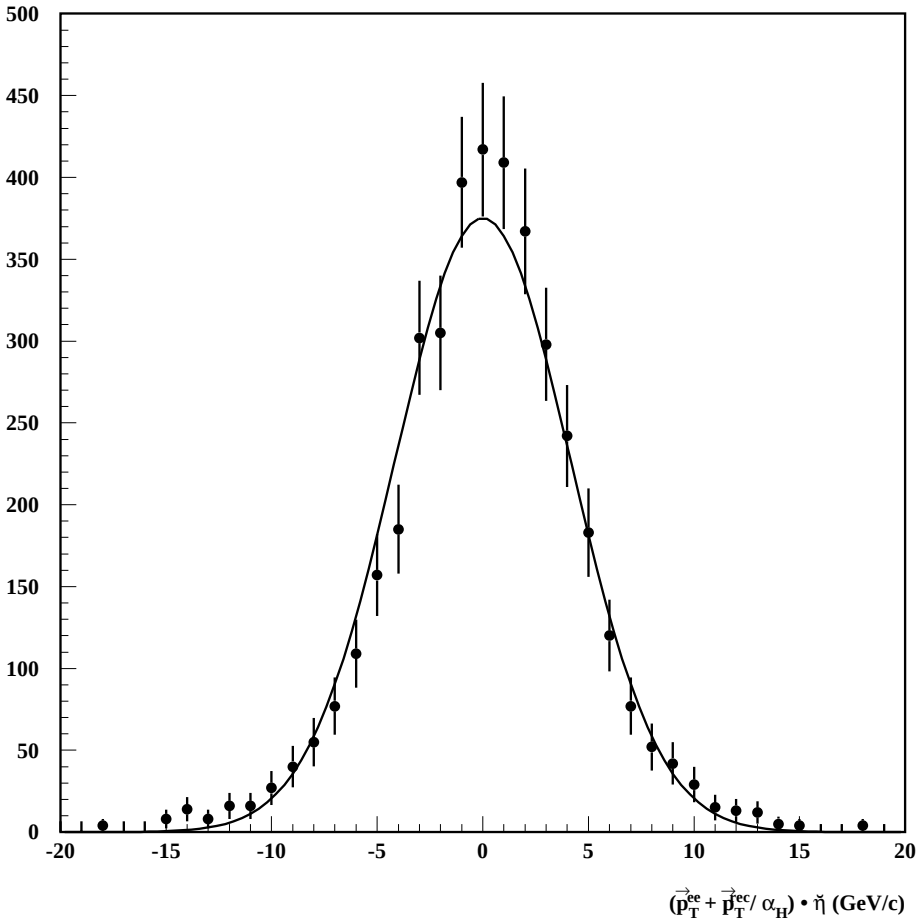

Figure 5.17: The corrected η imbalance. The Gaussian fit is also shown (curve).

Input Scale to CMS

In the Monte Carlo, the hadronic recoil is calculated from the electronic recoil by multiplying with the response parameter R_{rec} (see section 5.3.8). However, the parameters α_H, β_H, γ_H, δ_H used to determine R_{rec} are determined from the transverse momentum in the η-direction. At low transverse momentum, $p_{T,\eta}$ will be considerably lower than p_T as seen in figure 5.18. In addition, in the Monte Carlo there

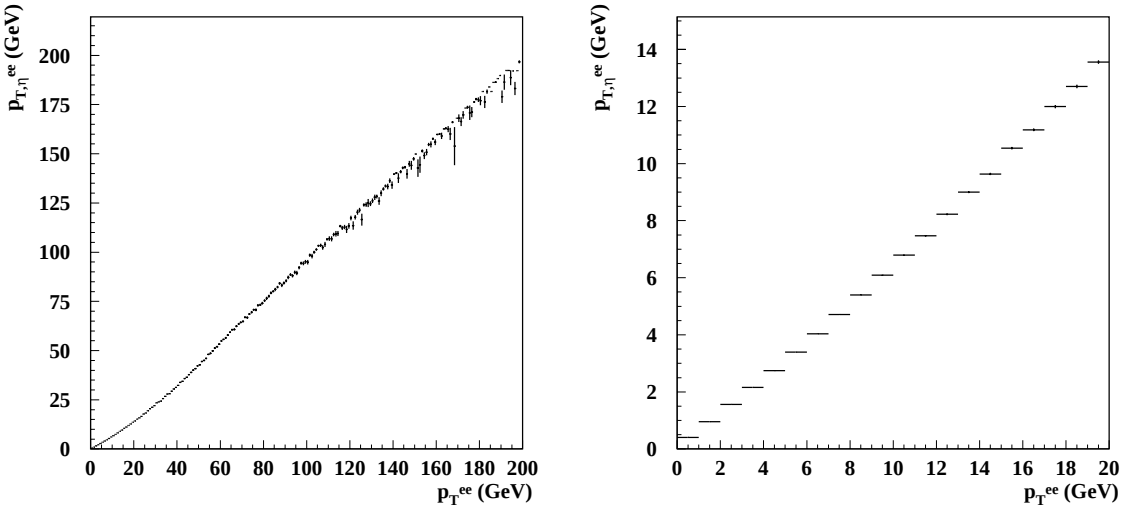

Figure 5.18: $p_{T,\eta}^{ee}$ versus p_T^{ee} from Monte Carlo for all p_T (left) and $p_T < 20$ GeV (right).

are also other corrections applied to the recoil which affect the hadronic response, mainly due to contributions from the underlying event [55]. The underlying event comprises all the interactions from spectator quarks, i.e. all the physics apart from the hard scatter and its final state radiation. This means that a set of hadronic parameters used as input to CMS might yield different parameters when a fitting technique as described in section 5.3.8 is applied to the Monte Carlo events.

To correct for these effects, the input parameters for CMS have to be determined that yield the same hadronic parameters as the data. We vary one parameter at a

time and iterate until the parameters agree. Table 5.4 summarizes the measured hadronic response parameters and the input values for CMS that produce the same fit parameters.

	α_H	β_H	γ_H	δ_H
data	0.972 ± 0.0095	-1.21 ± 0.14	0.099 ± 0.019	0.620 ± 0.047
input CMS	0.973	-1.50	0.130	0.500
output CMS	0.972	-1.21	0.097	0.616

Table 5.4: Measured hadronic response parameters and input parameters for CMS.

5.3.9 Tuning the Recoil Resolution Parameters

The resolution for the hard component of the recoil momentum u_T is parameterized as

$$\sigma_{rec} = s_{rec}\sqrt{u_T} \tag{5.22}$$

where σ_{rec} is the resolution of the calorimeter and s_{rec} is a tunable parameter. The soft component of the recoil is modeled by adding $\not\!\!E_T$ from Minimum Bias events[7] to the transverse momentum balance. The $\not\!\!E_T$ is added randomly in ϕ, modeling detector resolution effects and pile-up. This additional $\not\!\!E_T$ component is scaled by a tunable factor α_{mb}.

We tune the two parameters s_{rec} and α_{mb} simultaneously since they are strongly correlated. The optimal choice for the two parameters is determined by the following method: The width of the $\eta-$balance distribution is plotted in bins of $p^{ee}_{T,\eta}$

[7]Minimum Bias events are taken with a trigger requiring only that a $p\bar{p}$ interaction has taken place. The kinematic properties of these events are independent of specific hard scatter processes and model detector resolution effects and pile-up which lead to a finite $\not\!\!E_T$.

(see figure 5.19). The $\eta-$balance resolution has three components, one is due to s_{rec}, the second one to α_{mb}, and the third one is due to the electron resolution. The contribution from each one of these components is determined by varying the corresponding parameter while setting the other two parameters to zero and plotting the η-balance resolution as a function of the varied parameter. The electron resolution is considered fixed and simply turned off and on to determine the $\eta-$balance resolution due to it. A combined χ^2 is formed according

$$\chi^2 = \sum_{p_\eta (ee)\ bins} \left(\frac{\sigma_{ele} \oplus \sigma_{s_{rec}} \oplus \sigma_{\alpha_{mb}} - \sigma_{data}}{\delta_{data}} \right)^2 \tag{5.23}$$

and the optimal values for s_{rec} and α_{mb} are the ones that minimize this χ^2. The optimal values are the ones in the center of the $\chi^2 + 1$ ellipse in figure 5.20. We find them to be $s_{rec} = 0.665 \pm 0.062$ and $\alpha_{mb} = 1.064 \pm 0.02$.

The overall energy flow transverse to the beam direction is measured by the sum $S_T = \sum_i E_i \sin\theta_i$ over all calorimeter cells except cells belonging to the electron cluster. For W events $\langle S_T \rangle = 98.7$ GeV $\pm$ 0.3 GeV and for Z events $\langle S_T \rangle = 91.0$ GeV $\pm$ 0.9 GeV (see [46]). The resolution for measuring transverse momentum balance along any direction is

$$\sigma_T(S_T) = 1.42\,\mathrm{GeV} + 0.15\sqrt{S_T\,\mathrm{GeV}} + 0.007 S_T \tag{5.24}$$

The different energy flows in W and Z events lead to a correction to α_{mb} of $\sigma_T(98.7\,\mathrm{GeV})/\sigma_T(91.0\,\mathrm{GeV}) = 1.03 \pm 0.01$, leading to $\alpha_{mb} = 1.095$. This correction is not correlated with s_{rec}. Z bosons are not intrinsically produced with less energy flow in the underlying event than W bosons. The requirement of two isolated electrons biases the Z sample towards lower energy flow compared with the W sample where only one electron is required(see [46]).

The study leading to the above values of s_{rec} and α_{mb} was performed with a linear hadronic scale. Since the hadronic scale is non-linear in the low-p_T region, one would have to redo this study for low p_T events. But dividing the data into

two samples in p_T would increase the statistical error on the parameters; hence we choose an alternative approach: Former analyses [69] used PNUT2 instead of PNUT4 for the missing E_T which leads to an energy scale of $\alpha_H = 0.73$, close to what we get if for events with $p_{T,\eta} < 5$ GeV (0.68). Therefore, for events with $p_T <$ 10 GeV we adopt the value $s_{rec} = 0.50$ obtained for events with PNUT2 with the same error as above (0.062). Since α_{mb} should not depend on the hadronic scale, we use the same value throughout.

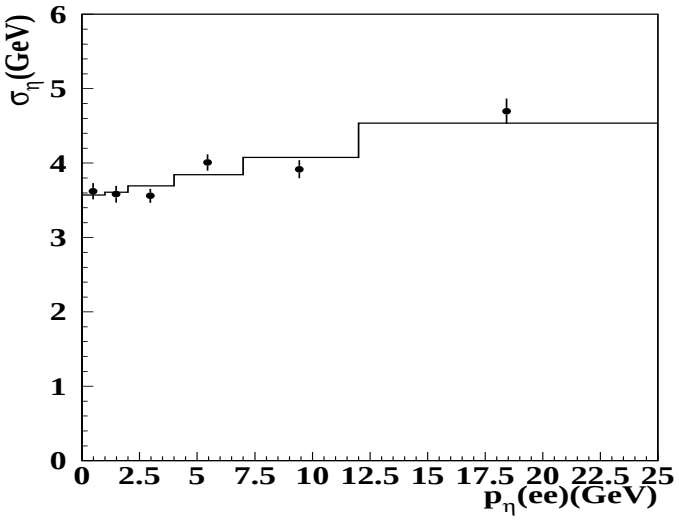

Figure 5.19: The width of the $\eta-$balance distributions versus $p_{T,\eta}^{ee}$ for the Z data (crosses) and the CMS Monte Carlo simulation (solid histogram).

5.3.10 Underlying Event energy

In the calculation of the recoil $\vec{u}_T$, the energy cluster assigned to the electron is excluded. This energy cluster does not only contain the energy deposited by the electron but also some energy from other particles in the event and electronic noise. By excluding this energy, a bias in the recoil along the direction of the electron, $u_{\parallel}$, is introduced. This bias is a function of $u_{\parallel}$ and instantaneous luminosity since

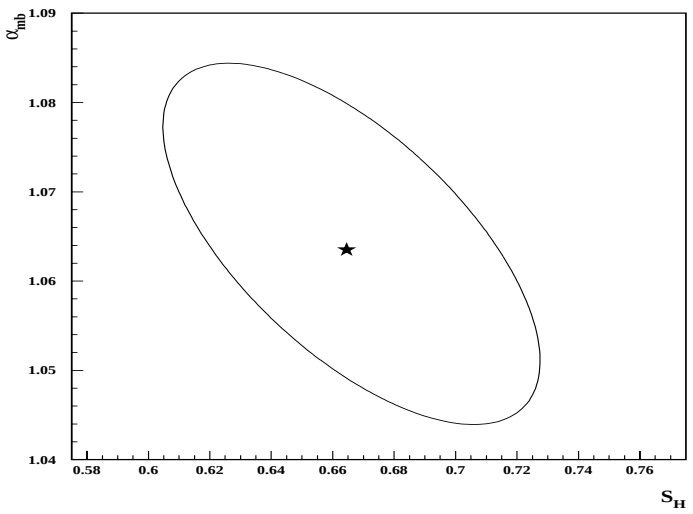

Figure 5.20: The $\chi_0^2 + 1$ contour for the recoil resolution parameters α_{mb} and s_{rec}.

more activity in the event causes more underlying energy to be lost. It is calculated from the transverse energy flow into 1×5 tower segments in $\eta \times \phi$ separated in ϕ from the electron so that no electromagnetic energy is included. Figure 5.21 shows the mean value of this bias, $\Delta u_{||}$ as a function of $u_{||}$ extrapolated to zero luminosity. It is important to model this bias well since it propagates directly into the transverse mass: For $p_T^W \ll M_W$

$$m_T \approx 2p_T(e) + u_{||} \tag{5.25}$$

In the CMS Monte Carlo program, a sixth order polynomial fit is used to parameterize the functional dependence of $\Delta u_{||}$ on $u_{||}$. Above $u_{||} = 30$ GeV and below $u_{||} = -25$ GeV the values at 30 GeV and -25 GeV are used, respectively, because of the limit in statistics at large $|u_{||}|$. For a more detailed description of the calculation of the underlying event energy see [46].

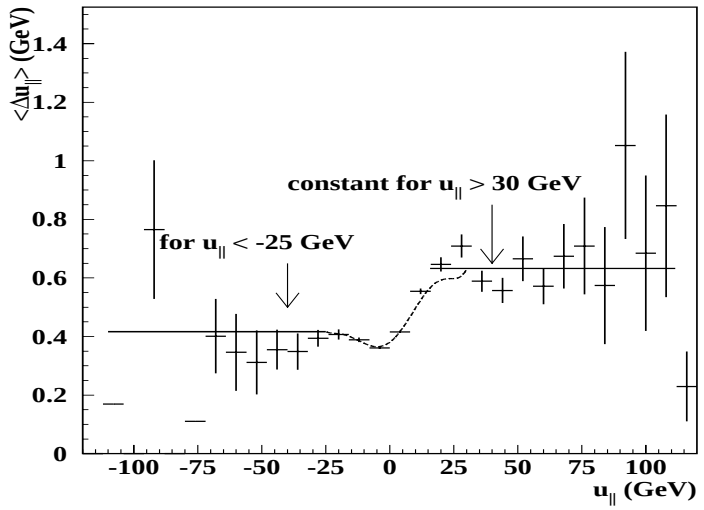

Figure 5.21: The variation of $\langle \Delta u_{\parallel} \rangle$ as a function of $u_{\parallel}$.

5.3.11 Summary of the CMS Simulation Parameters

The CMS Monte Carlo is used in this analysis to produce a theoretical prediction for the correlation between the angle of the electron in the Collins-Soper frame, $\cos\theta^*$, and the transverse mass of the W boson. CMS models detector smearing effects and detection efficiencies which allow the predictions to be directly compared to the data. Since CMS is very fast, it was easy to generate a large number of events, typically 20 million to 80 million for various studies. The program was run using the theoretical calculation by Ladinski and Yuan [60] and smeared according to the following parameters:

$$\alpha_H = 0.973 \pm 0.0095 \quad \text{Hadronic scale for } p_T > 10 \text{ GeV} \tag{5.26}$$

$$\beta_H = -1.5 \pm 0.14 \quad \text{Hadronic offset for } p_T > 10 \text{ GeV} \tag{5.27}$$

$$\gamma_H = 0.130 \pm 0.019 \quad \text{logarithmic part for } p_T < 10 \text{ GeV} \tag{5.28}$$

$$\delta_H = 0.500 \pm 0.047 \quad \text{Hadronic scale for } p_T < 10 \text{ GeV} \tag{5.29}$$

$$S_{rec} = (66.5 \pm 6.2)\% \quad \text{Sampling term for } p_T > 10 \text{ GeV} \tag{5.30}$$

$$S_{rec} = (50.0 \pm 6.2)\% \quad \text{Sampling term for } p_T < 10 \text{ GeV} \tag{5.31}$$

$$\alpha_{mb} = 1.095 \pm 0.02 \quad \text{Number of minimum bias events} \tag{5.32}$$

The systematic errors of the measured angular parameter α_2 due to detector simulation are obtained by varying the above parameters individually by $\pm 1\sigma$, redoing the analysis with the varied Monte Carlo predictions, and combining the resulting uncertainties in quadrature. This will be discussed in more detail in section 5.5. For more details on this see also [66]. The variation due to the choice of PDF is considered to be small [70], and CTEQ4M [71] is taken as the nominal choice.

5.4 The analysis

After having described analysis techniques developed for this measurement and the CMS Monte Carlo program, we will now discuss the analysis proper. The following section will cover data selection, backgrounds, and results obtained for the angular parameter α_2.

5.4.1 W selection

The event selection criteria for this analysis are identical to the ones used in the measurement of the transverse momentum distribution for Run 1B. For more details see [66]. The fiducial and kinematic cuts are also identical to the ones used in the measurement of the W cross section [72] with the main difference that this analysis uses PNUT4 and the four-variable likelihood rather than four separate electron identification cuts. These are the cuts used in this analysis:

- Trigger requirements
  - Events must pass the Level-0 minimum bias requirement;
  - Level-1 trigger (hardware)
    - $E_T^{em} > 12.0$ GeV or 10.0 GeV (dependent on trigger version);

* GOODCAL beam veto: events that occurred during the MRBS_LOSS period were rejected;

- Level-1.5 trigger (hardware)
  * $E_T^{em} > 15.0$ GeV (for trigger versions 10.0 and higher);
  * electromagnetic fraction $f_{em} > 0.85$ (for trigger versions 10.1 and higher);
- Level-2 filter (software)
  * Event must pass the Level-2 trigger $EM1\_EISTRKCC\_MS$
    This trigger requires an electromagnetic object ≥ 20 GeV (see section 4.6), loose shower shape (ele) and isolation fraction cuts (iso) and $\not\!\!E_T \geq 15.0$ GeV;
  * Event must pass the GoodBeam veto condition: Events that are flagged with MRBS_LOSS or MICRO_BLANK are rejected (for more on beam vetoes see section 3.6.2);

- acceptance cuts
  - one electron with $p_T \geq 25$ GeV in a good fiducial region of the detector: $|\eta_{det}| \leq 1.1$ [8] and $5\% < \mathrm{mod}(\phi^e_{cluster}) < 95\%$ in the CC where mod $(\phi^e_{cluster})$ is defined as the ϕ-angle of the electron cluster relative to the edge of the central electromagnetic calorimeter module, in units of the angle subtended by the module.
  - p_T(neutrino)$\geq$ 25 GeV. Cafix jet corrections are applied to the missing E_T(PNUT4);

[8] The detector-η (η_{det}) is the pseudorapidity of the electromagnetic cluster in the calorimeter with respect to the center of the detector as opposed to the physics-η which is calculated with respect to the vertex.

- electron quality cuts
  - one tight electron which is defined by the following cuts:
    * isolation ($f_{iso} < 0.15$) (see section 4.7);
    * four variable likelihood $\mathcal{L}_4 \leq 0.25$. The four variable likelihood consists of EM fraction, H-matrix χ^2, track match significance and drift chamber dE/dx [42];
    * good track match[9]: $\sigma_{trk} < 5$;
- The tight electron determines the vertex position, $|z| \leq 96.875$;[10]
- For efficiency studies, Z background rejection and calculation of the QCD background, three additional less stringent definitions are needed:
  - A probe electron passes the Level-2 esc16 [11] requirement of the trigger and has to be in the good fiducial region of the detector;[12]
  - A loose electron is an isolated ($f_{iso} < 0.15$) electromagnetic cluster in the good fiducial region that passes the Level-2 $eis20$ trigger;

[9]The $\sigma_{trk} < 5$ cut is imposed on a tight electron in addition to the four variable likelihood cut since the definition of a mother electron already includes the σ_{trk} cut. The reason for this is that we start from PELC's and PPHO's; the track requirement eliminates photon candidates. None of the events that pass the for variable likelihood cut fail the track match requirement.

[10]This cut is imposed to be consistent with the Level-0 requirement.

[11]The Level-2 shower shape cut is denoted by ele, the isolation requirement is labeled iso, requiring both is denoted by eis; while requiring neither is labeled esc. The Level-2 E_T requirement is appended to the trigger term: $esc16$ refers to an esc object > 16 GeV.

[12]The studies referred to here use Z events with one tight electron. The second electron can then be used as an unbiased probe for efficiency studies. In order to determine the efficiency of the isolation cut of the trigger, a diagnostic sample that passed the $EM2\_EIS\_ESC$ Level-2 filter was used. This filter requires one isolated EM cluster with transverse energy $E_T^{L2} \geq 20$ GeV while the other was only required to have $E_T^{L2} \geq 16$ GeV.

  - A mother electron is a loose electron that passes tracking requirements, i.e. $\sigma_{trk} < 5$;
  - A tight electron is a mother electron that passes the four-variable likelihood cut $\mathcal{L}^{(4)} < 0.25$.

- Events with a second loose electron are rejected if the invariant mass of the two electrons is close to the Z mass i.e. $m_{ee} \in$[75 GeV,105 GeV];
- 41173 CC events pass these selection criteria;
- in addition to these cuts, this analysis is performed for 50 GeV $\leq m_T^W \leq$ 90 GeV.

Optimizing the Likelihood Cut

Cutting on the single four-variable likelihood allows us to make the optimal choice of background fraction and efficiency. Figure 5.22 shows the tight electron efficiency (see section 5.4.2) versus four variable likelihood cut. Figure 5.23 shows the QCD background fraction for all p_T (left) and 50 GeV $< p_T <$ 200 GeV versus four variable likelihood cut. One can see that both the efficiency and the background fraction depend strongly on this cut. Since this analysis is most sensitive at large values of p_T, a tight cut for the four variable likelihood is chosen to keep the background small at large p_T. This cut is the same as the one chosen by the top mass analysis. Figure 5.24 shows the Significance ($\sigma = \text{signal}/\sqrt{\text{background}}$) as a function of four variable likelihood for all p_T (left) and 50 GeV $< p_T <$ 200 GeV. One can see that the significance, which is a common variable to be maximized when optimizing a certain cut, increases with a tighter cut on the four variable likelihood. An even tighter cut than 0.25 would not be desirable since this analysis already suffers from statistical limitations.

The best way to optimize this cut and in principle all cuts would be to perform

the full analysis with variable cut values and choose the cut value that minimizes the error on the final measurement (here the angular parameter α_2). However, this is almost never done since it would involve recalculating the backgrounds and efficiencies many times and translating them into the final analysis. Instead reasonable assumptions are made about desirable efficiencies and background levels.

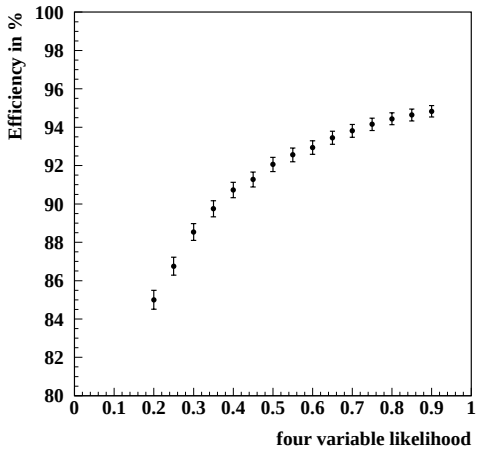

Figure 5.22: Electron efficiency as a function of the 4-variable likelihood cut.

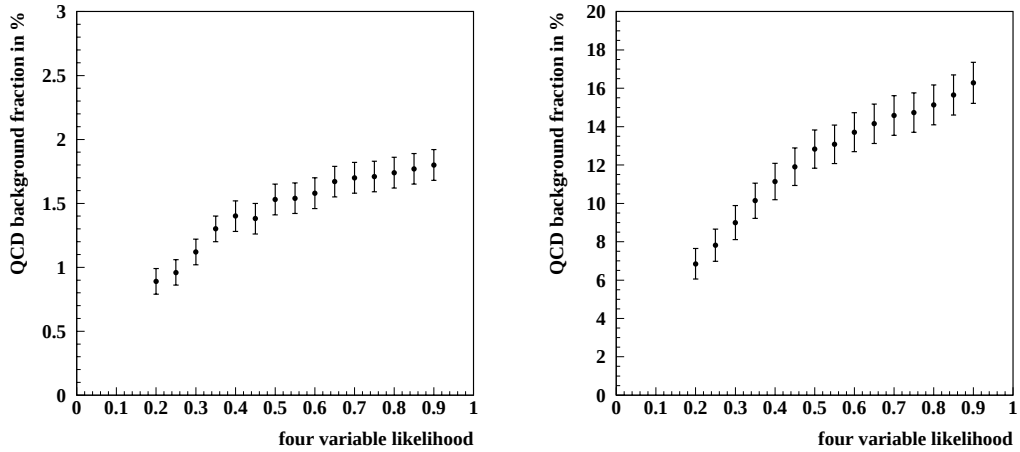

Figure 5.23: QCD background fraction as a function of the 4-variable likelihood cut for all p_T (left) and 50 GeV $< p_T <$ 200 GeV (right).

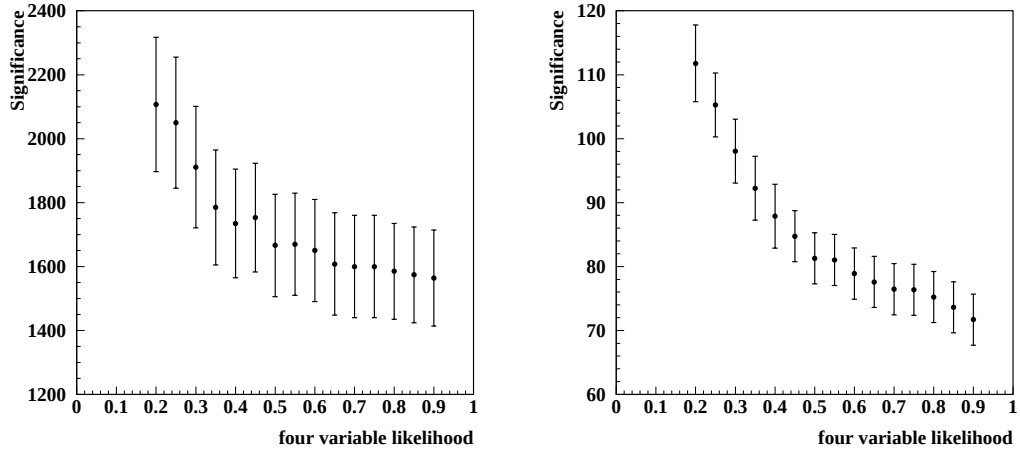

Figure 5.24: Significance ($\sigma = \text{signal}/\sqrt{\text{background}}$) as a function of the 4-variable likelihood for all p_T (left) and 50 GeV $< p_T <$ 200 GeV (right).

5.4.2 Efficiencies

The methods to calculate efficiencies are described in [66]. The following signal efficiencies are calculated from $Z \to ee$ events. Events are required to pass the $EM2\_EIS\_ESC$ Level-2 filter, contain two PELC-banks[13] and have two electromagnetic objects in the good fiducial region of the detector with $E_T^e > 25$ GeV . The invariant mass of the two electrons has to be close to the Z mass (86 GeV $< M_{ee} <$ 96 GeV) and one of the electrons has to pass the tight electron selection criteria (See section 5.4.1). The other electron can then be used as an unbiased probe for efficiency studies.

The underlying background is estimated by applying the same selection criteria as above to two symmetric side-band regions (61 GeV $< M_{ee} <$ 71 GeV and 111 GeV $< M_{ee} <$ 121 GeV) and subtracting the average number of events in these regions from the number of events in the signal region (86 GeV $< M_{ee} <$ 96 GeV). The side-bands are selected such that they are far enough from the signal region to contain mainly background events. Each side-band is 10 GeV wide so that the number of events to be subtracted from the signal region is simply the average of the number of events in the side-bands. (For the choice of side-bands, see also section 5.4.3).

Hence the background subtracted efficiency of a cut A relative to a looser cut B is given by:

$$\varepsilon_{B \to A} = \frac{N_s^A - N_b^A}{N_s^B - N_b^B}, \tag{5.33}$$

where, for example, N_s^A and N_b^A are the number of signal and background events in the sample that pass cut A, respectively. Following the method and notation of references [73, 69, 74, 75], the overall selection efficiency can be expressed

[13] An electromagnetic cluster enters a PELC-bank if at least one matching track was found, otherwise it enters a PPHO-bank since it is most likely associated with a photon in this case.

as the product of five factors: the efficiency of the Level-Ø system (ε_{L0}), the efficiency of the Level-2 trigger $\not\!\!E_T$ requirement (ε_{L2met}), the electron trigger efficiency (ε_{trig}), and the efficiencies of the off-line electron identification (ε_{id}) which includes calorimeter ID and tracking efficiencies. The trigger and off-line electron ID efficiencies are measured together as the *tight electron selection efficiency* (ε_{ele}^{W}).

$$\varepsilon_{tot} = \varepsilon_{L0} \cdot \varepsilon_{L2met} \cdot \underbrace{\varepsilon_{trig} \cdot \overbrace{\varepsilon_{cal} \cdot \varepsilon_{trk}}^{\varepsilon_{id}}}_{\varepsilon_{ele}^{W}} \tag{5.34}$$

Therefore, the tight electron selection efficiency is measured as:

$$\varepsilon_{ele}^{W} \stackrel{\text{def}}{=} \frac{\sharp \text{ of tight electrons}}{\sharp \text{ of probe electrons}} \tag{5.35}$$

The background subtracted result of the selection efficiency is:

$$\varepsilon_{ele}^{W} = 0.6620 \pm 0.0057 \text{ (stat)} \qquad \text{in the CC} \tag{5.36}$$

Figure 5.25 shows the tight electron selection efficiency as a function of p_T^W including a heuristic fit function (see [66]). Using these electron definitions, the efficiency of the tight cuts relative to the sample of mother electrons is also measured. This efficiency will be used for the determination of the multi-jet background in section 5.4.3.

$$\varepsilon_{\text{mother}\to\text{tight}} = \varepsilon_t \stackrel{\text{def}}{=} \frac{\sharp \text{ of tight electrons}}{\sharp \text{ of mother electrons}} \tag{5.37}$$

The efficiency of the tight cuts is:

$$\varepsilon_t^{CC} = 0.8675 \pm 0.0047 \text{ (stat)} \tag{5.38}$$

Figure 5.26 shows the efficiency ε_t^{CC} as a function of p_T.

Note that the tight electron efficiency shows a slight dependence on the transverse momentum of the W as a result of the isolation cut. We choose the electron efficiency flat in p_T^W with an error of 10% to cover this effect.

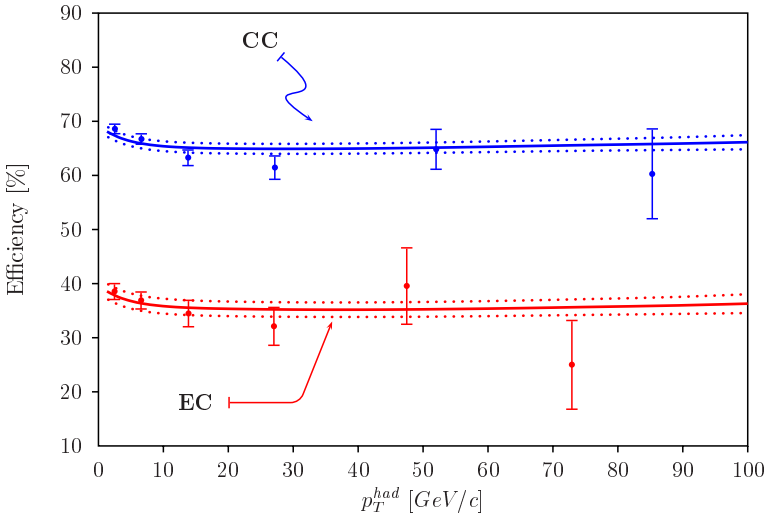

Figure 5.25: Background corrected *tight electron selection* efficiency ε_{ele}^{W} as a function of the transverse momentum p_T^{had}. The full line represents the parameterized efficiency and the systematic uncertainty is shown as dotted line.

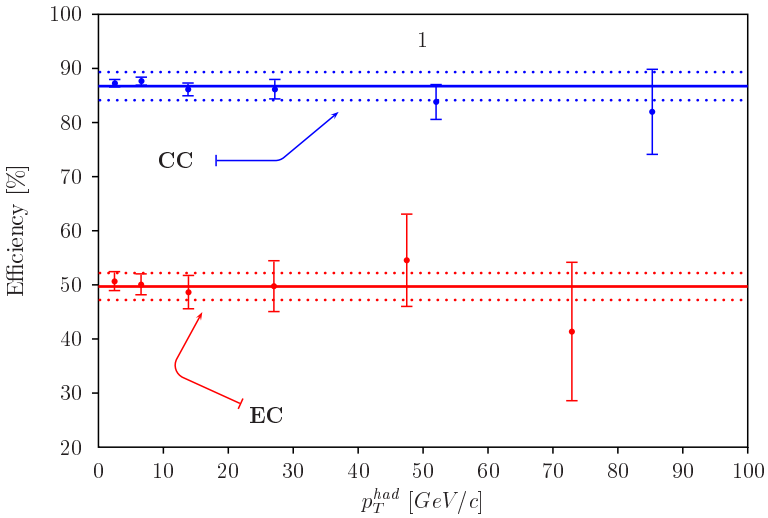

Figure 5.26: Efficiency of the *tight cuts* relative to the cuts applied to the mother sample ε_t as a function of p_T^{had}. The dotted lines represent a 3% systematic uncertainty around the inclusive values shown as full lines.

5.4.3 Backgrounds

In this analysis, the lepton angle $\cos\theta^*$ is inferred from the transverse mass on a statistical basis. The results of this procedure will only be accurate if backgrounds are correctly taken into account. There are two possible ways to include backgrounds in the Bayesian analysis used to measure the angle: The equation to invert the transverse mass (equation 5.5) could itself contain terms for the backgrounds which would then be treated as nuisance parameters, i.e. unwanted parameters that are integrated over.

The second method is to subtract all backgrounds from the transverse mass distribution and invert the background subtracted distribution. While the first method might seem to be preferable since it makes full use of the power of Bayesian statistics, we chose the second method for the following reason: In order to include the backgrounds into the Bayesian method, their prior probability distributions in $\cos\theta^*$ would have to be known. For QCD multijet events that fake signal events, this prior distribution is not known and assumptions about it would have to be made.

Instead of directly including the backgrounds into the Bayesian method, we determine the transverse mass spectrum for each background in the four p_T bins used in this analysis and subtract it from the transverse mass spectrum for $W \to e\nu$ candidate events. To avoid large statistical fluctuations, the background shapes are fit with appropriate functions and the fit shapes are subtracted. The errors on the final measurement of α_2 due to errors in the backgrounds are determined by varying the background shapes and overall rates by their errors and rerunning the analysis with the varied backgrounds.

QCD Multijet Background

Although the use of tight electron selection criteria (specially the four variable likelihood) reduces the QCD background fraction very effectively, QCD multijet events which pass all W selection criteria still pose one of the largest backgrounds. The reason for this is the very large multijet cross section (several μb) compared to the W cross section (22.27 nb [69]). QCD multijet events can fake W events if one jet is misidentified as an electron and the energy in the event is mismeasured due to another jet being located in one of the uninstrumented regions of the detector which results in large $\not\!\!E_T$. To estimate this background, the matrix method described in [69] is used. For a derivation of the equations used below see appendix C. The background fraction can be written as

$$f_b = \frac{N_b \epsilon_j}{N_t} \tag{5.39}$$

where N_t is the number of tight electrons in the signal sample, N_b is the number of background events in the mother sample, and $\epsilon_j = \frac{N_{tight}}{N_{mother}}$ is the rate for a bad mother electron to pass the tight selection cuts. N_{mother} and N_{tight} are the number of bad electrons that pass the mother and tight electron selection cuts, respectively.

A sample of "bad" electrons is obtained from the the Level-2 monitor trigger $em1\_ele\_mon$.[14] This trigger had no missing E_T cut imposed, and contamination of real W events is avoided by selecting events with low missing E_T ($E_T \leq 15$ GeV). Figure 5.27 shows ϵ_j as a function of missing E_T. The number of background events in the mother sample is calculated as follows:

$$N_b = \frac{\epsilon_s N_m - N_t}{\epsilon_s - \epsilon_j} \tag{5.40}$$

where N_m and N_t are the number of mother and tight electrons in the signal

[14] This trigger requires an electromagnetic object with E_T greater than 20 GeV, no missing E_T cut is imposed. Unfortunately, only a limited number of events were taken with this trigger.

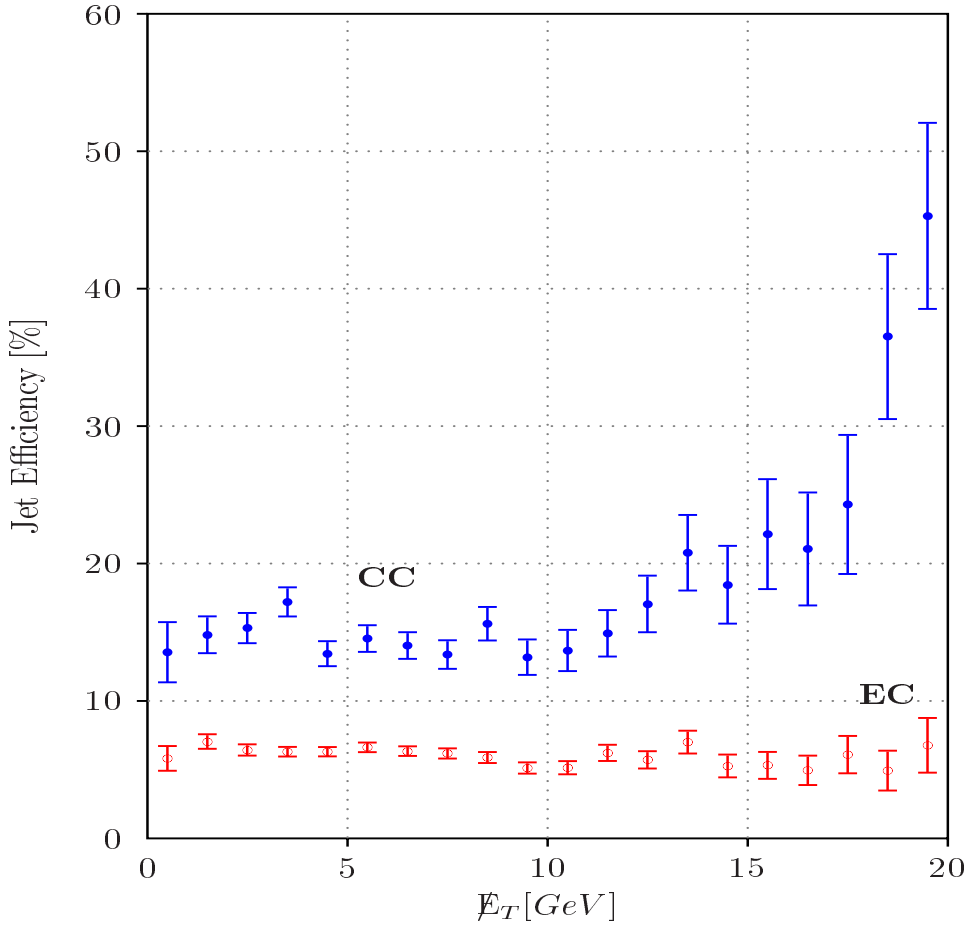

Figure 5.27: Missing E_T for QCD fake events.

sample[15], and

$$\epsilon_s = \frac{N_{t,\,side-band\,subtracted}}{N_{m,\,side-band\,subtracted}} \tag{5.41}$$

is the efficiency for a good mother electron to pass tight selection cuts. This efficiency is calculated from $Z \to ee$ events: A good electron is selected by requiring at least one tight electron in a Z event and using the second electron as an unbiased probe. These events are further required to have an invariant mass in the Z mass region between 86 and 96 GeV. Background events are accounted for by subtracting events from the symmetric side-bands outside the Z mass region, i.e. $m_{ee} \in [60, 70]$ or $m_{ee} \in [110, 120]$. The invariant Z mass for mother and tight events is shown in figure 5.28.

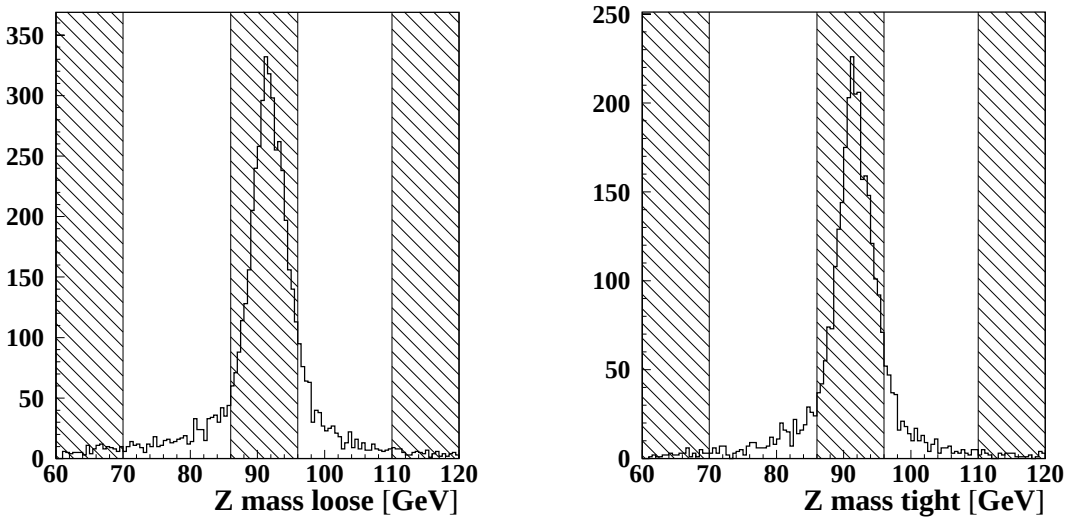

Figure 5.28: Z invariant mass for mother (left) and tight (right) electrons. The signal region and the two side-bands are hatched.

The overall QCD background fraction is $0.95\% \pm 0.6\%$ ($0.77\% \pm 0.6\%$) without (with) a transverse mass cut of 50 GeV $< m_T^W <$90 GeV imposed. Figure 5.29

[15]By signal sample we mean the sample of $W \to e\nu$ candidate events obtained by applying the W selection cuts described in section 5.4.1.

shows the QCD background fraction as a function of transverse mass in four p_T bins. In figure 5.30 the number of QCD background events is shown in the four p_T regions. A third order polynomial fit is used for subtracting the background shape from the transverse mass distribution for W boson events. Figure 5.30 shows the fit together with its errors.

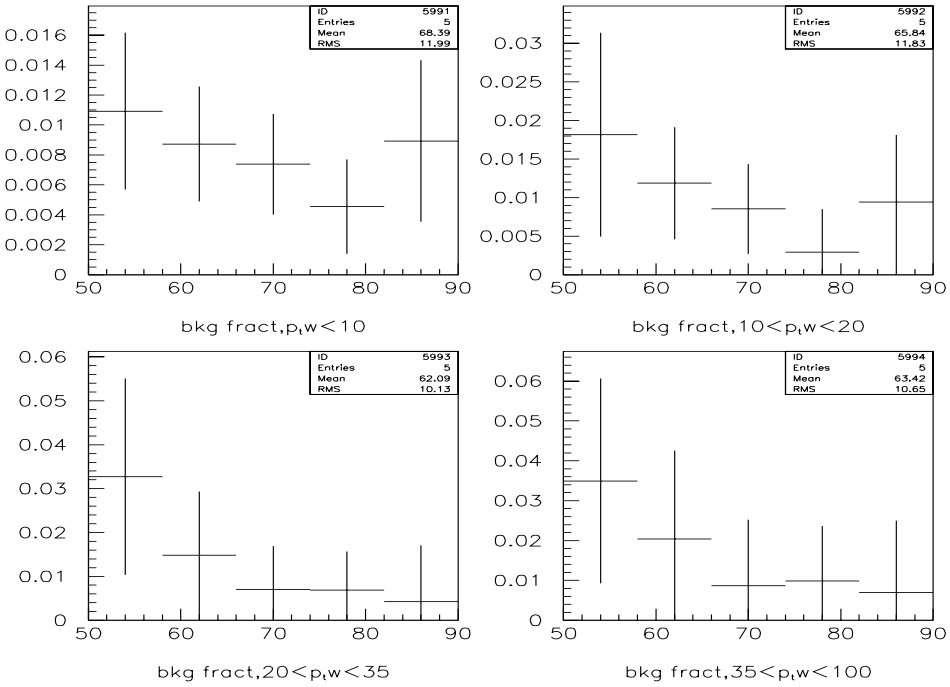

Figure 5.29: QCD background fraction in four p_T(W) bins.

$Z \to ee$

Z events can look like W events if one electron is lost (in the Inter Cryostat Detector (ICD) or in one of the 32 gaps between CC modules) and the resulting energy imbalance fakes large missing E_T. This background can only be estimated using Monte Carlo $Z \to ee$ events where the "lost" electron is actually available at the generator level and only disappears in the subsequent detector simulation.

The number of Z events present in the W sample is calculated by applying

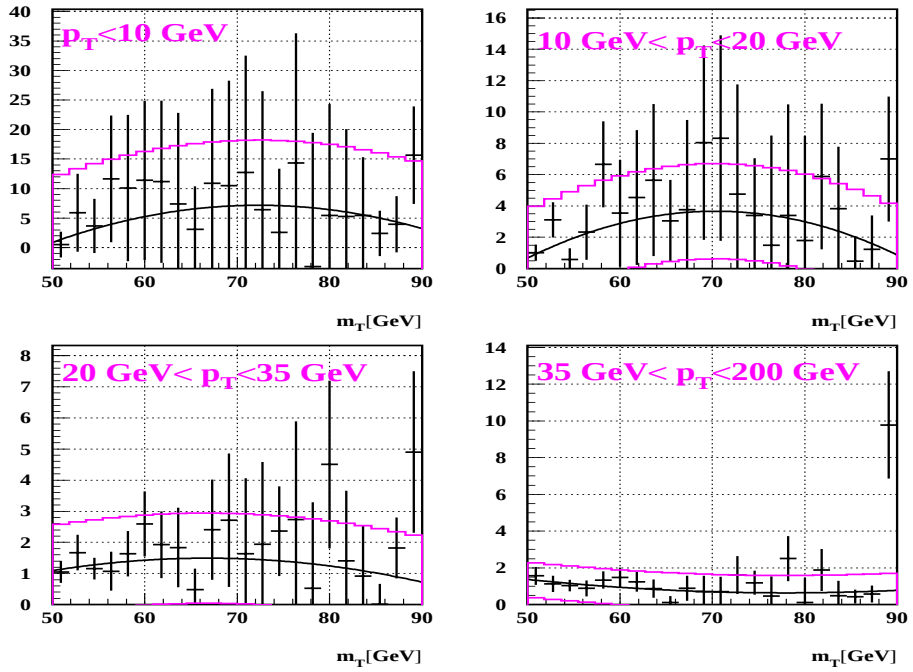

Figure 5.30: Number of QCD background events in four p_T^W bins as a function of m_T. The curves shown are the fits and overall background errors.

the W selection cuts to Herwig+ Showerlibrary $Z \to ee$ events [16] that were overlaid with minimum bias events to model the additional interactions at each beam crossing. To estimate the dependence of this background on the instantaneous luminosity of the event, the overlay was done for two different luminosities. The two luminosities are chosen to be the average for each of two luminosity bins if the data is divided into two bins of roughly equal number of events. The mean luminosities are $3 \times 10^{30} cm^{-2}\mathrm{s}^{-1}$ and $1.4 \times 10^{31}, cm^{-2}\mathrm{s}^{-1}$, respectively. Since no strong luminosity dependence of the background fraction was found ($f_Z^W = 0.0092 \pm 0.0011$ for the low luminosity sample and $f_Z^W = 0.0090 \pm 0.0010$ for the high luminosity sample), the average value for both luminosities is used. The number of Z background events in the W sample is then:

$$N_Z^W = N_{probe} \epsilon_{ele}^W \frac{L_W}{N_{generated}/\sigma_Z} \tag{5.42}$$

[16] Herwig is known to model W/Z + jet events better than other available generators.

- with
  - N_{probe} is the number of Monte Carlo Z events that pass the W selection cuts (including $\not\!\!E_T > 25$ GeV) for a probe electron ($N_{probe} = 2935$ and 2858 for the low and high luminosity sample, respectively);
  - ϵ_{ele}^{W} is the efficiency for a probe electron to pass the tight electron cuts: $\epsilon_{ele}^{W} = 0.6620 \pm 10\%$ (see section 5.4.2);
  - L_W is the measured integrated Luminosity for W bosons in Run 1b: $L_W = (82.4 \pm 4.4)\text{pb}^{-1}$ [69];
  - σ_Z is the measured cross section for Z bosons in Run 1b: $\sigma_Z = (221 \pm 13)$pb [69];
  - $N_{generated}$ is the total number of Monte Carlo events generated (98798);
- The fraction of Z background events is calculated as follows:

$$f_Z^W = \frac{N_Z^W}{N_{DATA}^{tight}} \tag{5.43}$$

- $N_{DATA}^{tight} = 41173$ events is the number of W candidates that pass the final W selection cuts used in this analysis (see section 5.4.1);
- The overall background fraction is $f_Z^W = 0.0091 \pm 0.0013$ for all p_T.

It is known that the efficiency for a probe electron to pass the tight cuts is much higher for Monte Carlo events than for data events since the Herwig+Showerlibrary Monte Carlo does not simulate the effects of tracking very well [66]. For this reason we only apply probe cuts to the Monte Carlo sample instead of tight cuts and correct subsequently by the efficiency for a probe electron to pass tight cuts (ϵ_{ele}^{W}) as measured from data Z events.

The transverse mass distributions (shown in figure 5.31) for the first two p_T-bins are fit with Gaussians, the third one is fit with a double Gaussian, and the

highest p_T-bin is fit with a straight line. The errors of the fits shown are the errors due to the overall normalization of the fits.

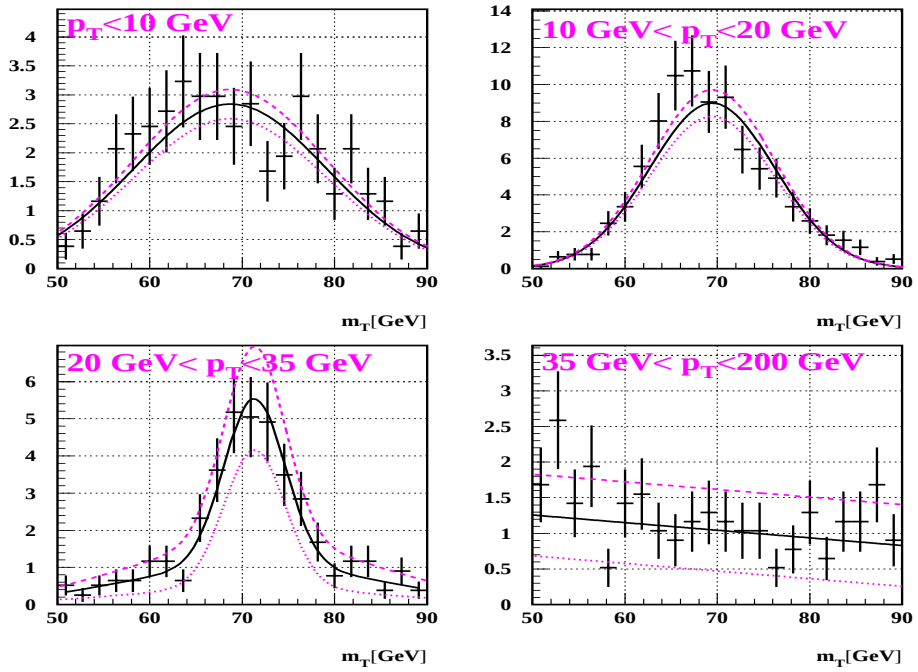

Figure 5.31: Z background as a function of transverse mass in four p_T bins. The curves shown are the fits and overall Z background errors.

Background from $t\bar{t}$ Events

The top background is calculated in a similar way to the Z background from Herwig+Showerlibrary $t\bar{t}$ events:

$$N_{top}^{W} = N_{probe}\epsilon_{ele}^{W}\frac{L_W}{N_{generated}/\sigma_{top}} \tag{5.44}$$

- with
  - N_{probe} is the number of Monte Carlo top events that pass the W selection cuts for a probe electron

- $\epsilon^W_{ele} = 0.6620 \pm 10\%$
- $\sigma_{top} = 5.9 \pm 1.7$pb [76]
- $N_{generated}$=35019

- The fraction of top background events can be calculated as follows:

$$f^W_{top} = \frac{N^W_{top}}{N^{tight}_{DATA}} \tag{5.45}$$

- The overall background fraction is $f^W_{top} = 0.0016 \pm 0.0005$ for all p_T.

In figure 5.32 the number of top background events as a function of transverse mass is shown for each p_T bin. Fits and their errors are included in the plots.

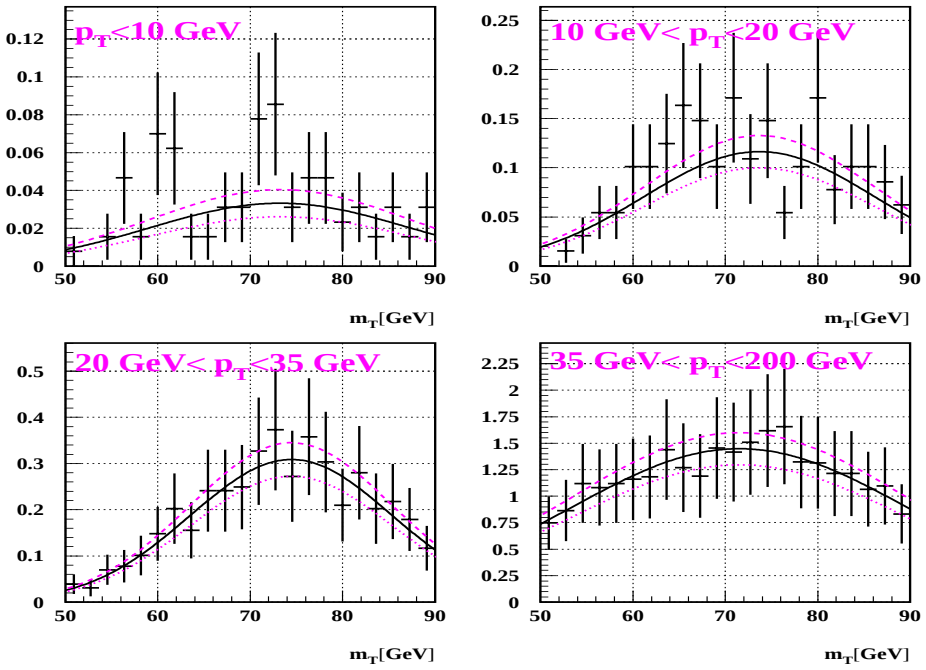

Figure 5.32: Top background as a function of transverse mass in four p_T bins. The curves shown are the fits and overall $t\bar{t}$ background errors.

$W \to \tau\nu$

$W \to \tau$ events where the τ subsequently decays into an electron and two neutrinos are indistinguishable from $W \to e\nu$ events. This background can only be estimated from Monte Carlo simulations. The tau background is calculated using the CMS Monte Carlo: A fraction of events is generated as tau's, decayed electronically and acceptance and fiducial cuts are applied to the decay electron in the same manner as for $W \to e\nu$ events. The acceptance for $W \to \tau\nu \to e\nu\nu$ is reduced by the branching fraction $B(\tau \to e\nu\nu) = 18\%$ [69]. The kinematic acceptance is further reduced by the E_T cut on the electron since the three body decay of the τ leads a very soft electron E_T spectrum compared to that from $W \to e\nu$ events (see figure 5.33). The tau fraction, after these cuts are applied to the CMS Monte Carlo, is $(2.22 \pm 0.21)\%$.

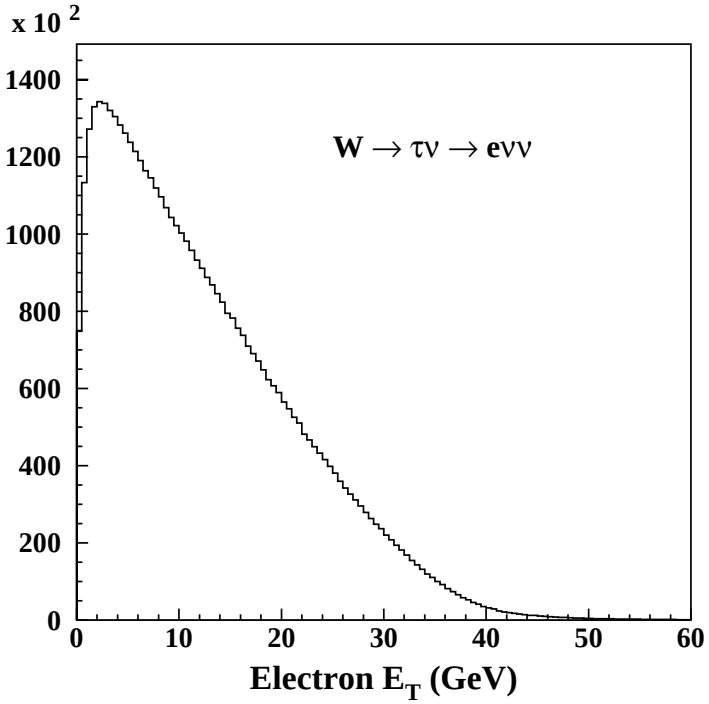

Figure 5.33: Electron E_T spectrum for $W \to \tau\nu \to e\nu\nu$ events (from CMS).

For this analysis, angular $\cos\theta^*$ templates are generated using the CMS Monte

Carlo simulator with a fraction of events being generated as τ's. For the transverse mass spectrum of $W \to \tau\nu$ events see figure 5.34. On average, the three-body decay leads to a smaller transverse mass.

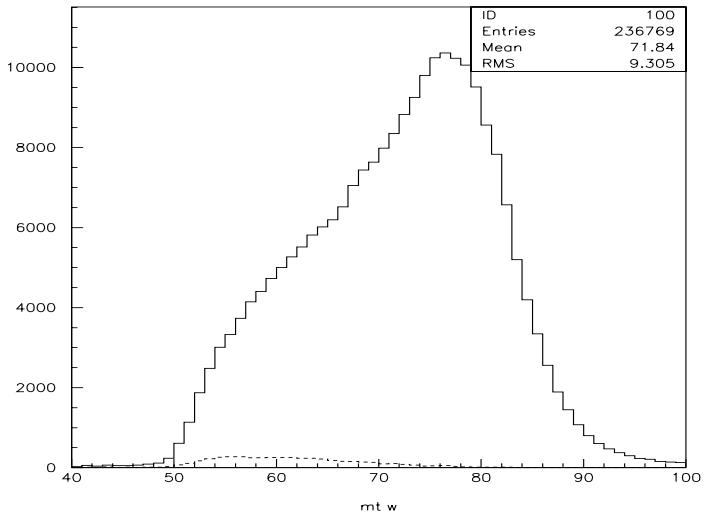

Figure 5.34: Transverse mass distribution for $W \to e\nu$ events (solid) and $W \to \tau\nu \to e\nu\nu$ events (dashed) from CMS.

Table 5.5 summarizes the background fractions for the three dominant backgrounds for the transverse mass range used in this analysis. All backgrounds are rather small due to tight electron identification criteria and the transverse mass cut imposed. In figure 5.35 the transverse mass distributions for W bosons in the four p_T bins are shown including the dominant background (excluding τ's). The background levels are small even at high p_T .

5.4.4 The W p_T Distribution

Since the measurement of α_2 is performed as a function of the transverse momentum of the W boson, it is important to model the p_T right. The measurement of the transverse momentum distribution is described elsewhere [66]. Figure 5.36

p_T	$0 \leq p_T \leq 10$	$10 \leq p_T \leq 20$	$20 \leq p_T \leq 35$	$35 \leq p_T \leq 200$
QCD	$(0.8 \pm 0.1)\%$	$(1.0 \pm 0.1)\%$	$(1.0 \pm 0.1)\%$	$(1.0 \pm 0.1)\%$
Z	$(0.158 \pm 0.02)\%$	$(1.06 \pm 0.13)\%$	$(1.44 \pm 0.2)\%$	$(1.76 \pm 0.22)\%$
top	$(0.0028 \pm 0.0009)\%$	$(0.025 \pm 0.008)\%$	$(0.15 \pm 0.05)\%$	$(2.0 \pm 0.6)\%$

Table 5.5: Summary of background fractions in $m_T^W \in [50, 90]$ in p_T bins. The errors shown are obtained by propagating statistical and systematic errors of all of the variables that enter the background calculations.

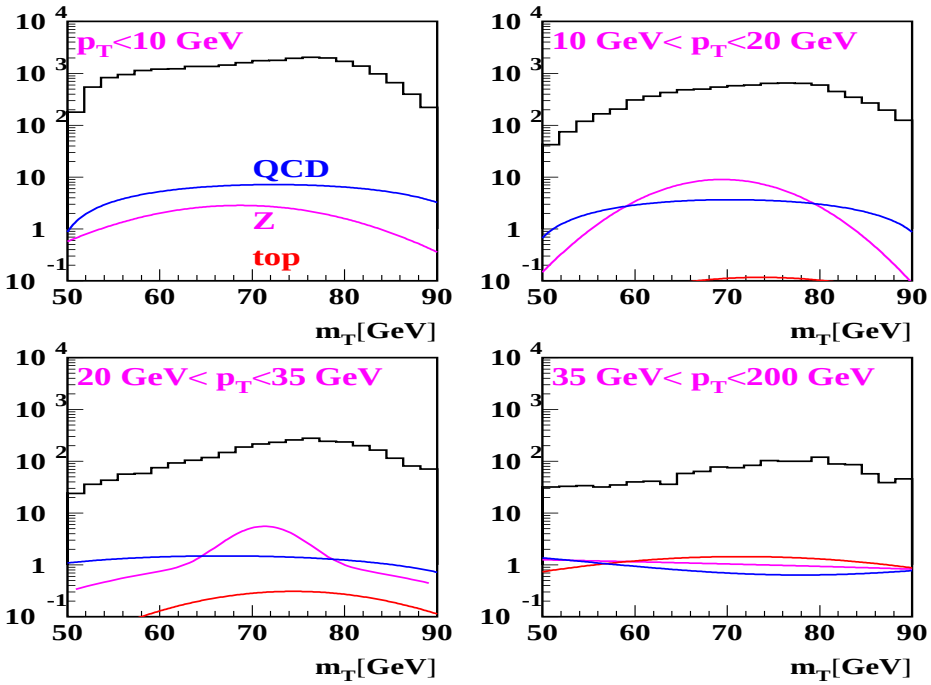

Figure 5.35: Transverse mass spectrum for $W \to e\nu$ candidate events and QCD (black), Z (light grey), and $t\bar{t}$ backgrounds (darker grey) in four p_T bins.

shows the measured transverse momentum distribution, of which all known backgrounds as described in section 5.4.3 have been subtracted. The data, including statistical errors, is compared to the combined theory by Ladinsky an Yuan [60] (resummation at low p_T) and Arnold and Reno [59] ($\mathcal{O}[\alpha_S^2]$ perturbative QCD) as described in section 5.3. The theory has been corrected for detector effects as described in section 5.3. Figure 5.37 shows the same distribution in the p_T range up to 30 GeV. To detect any systematic deviations, the ratio (data-theory)/theory is plotted in figure 5.38. The plots show that the agreement between data and smeared theory is very good and no substantial systematic difference can be detected. The sinusoidal shape in the low p_T region of figure 5.38 results from a slight shift in the peaks of the two compared distributions. The systematic uncertainties due to the recoil model and the backgrounds easily cover this shape.

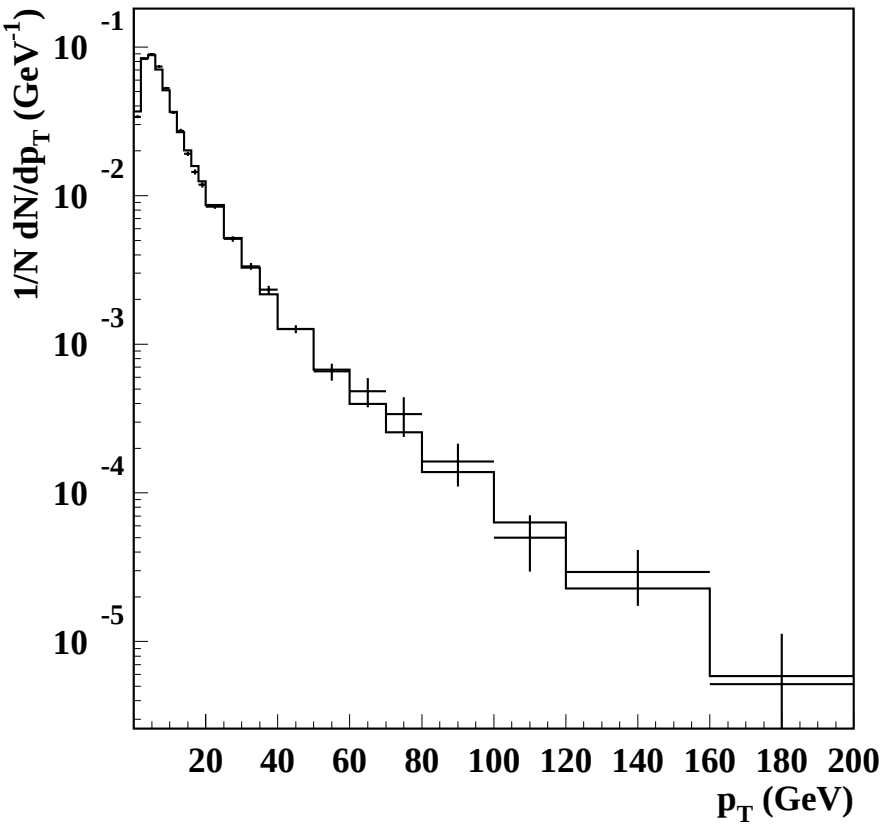

Figure 5.36: Background subtracted transverse momentum distribution for $W \rightarrow e\nu$ events (points with statistical errors) and smeared theory (solid histogram).

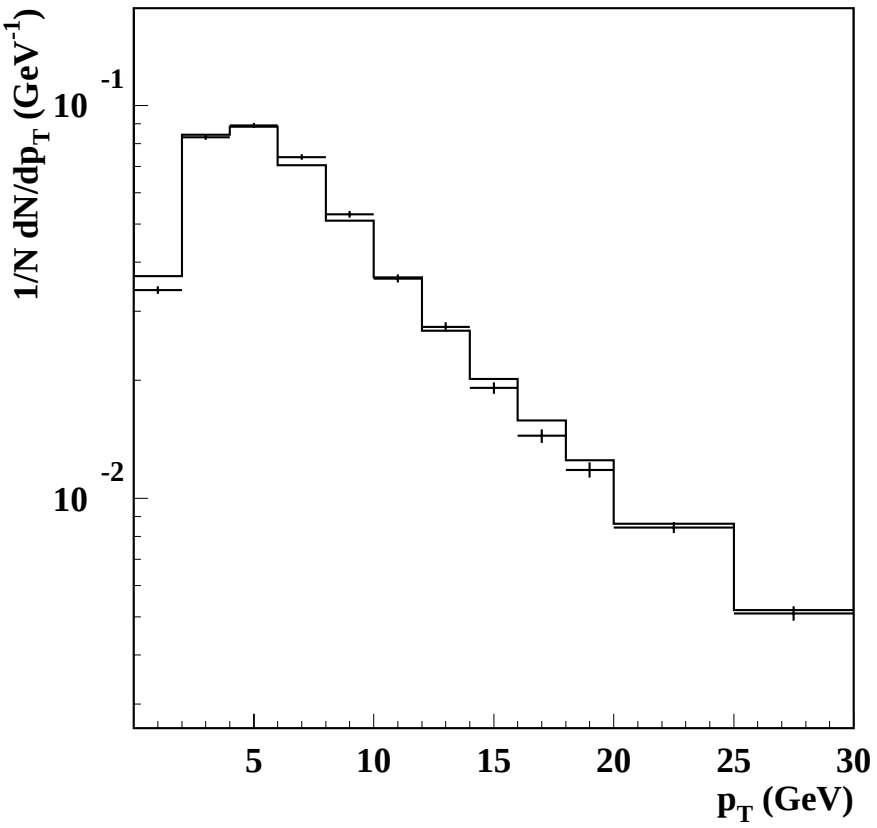

Figure 5.37: Background subtracted transverse momentum distribution for $p_T < 30$ GeV for $W \rightarrow e\nu$ events (points with statistical errors) and smeared theory (solid histogram).

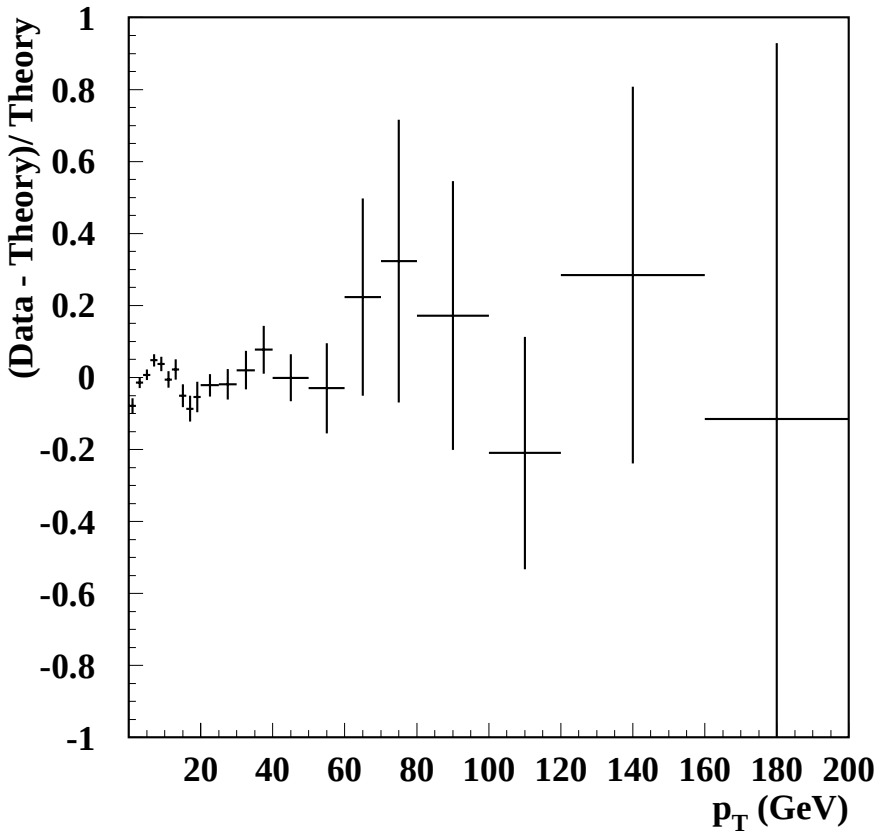

Figure 5.38: (Data-Theory)/Theory for the transverse momentum distribution.

5.4.5 The Measurement of α_2

To obtain the angular distribution for W events from data, the transverse mass distribution has to be inverted according to the Bayesian method described in section 5.2. Figure 5.39 shows the background subtracted transverse mass distributions for the four p_T bins used in this analysis compared to CMS. The χ^2-values per degree of freedom are 1.32, 0.70, 0.55, and 0.90, respectively, in order of increasing p_T. These correspond to a probability of 14%, 85%, 96%, and 60%, respectively, that a larger χ^2 is found.

In Figure 5.40 the angular distributions obtained from data are compared to the Monte Carlo templates that fit best. Also shown for comparison are the templates for $\alpha_2 = 1.0$ and $\alpha_2 = 0.0$. The errors of the points in this Figure are calculated from the errors in α_2 by taking into account the sensitivity of the angular distribution to α_2 in each bin:

$$\delta f_i^2 = (\frac{\partial f}{\partial \alpha})^2 \delta^2 \alpha \tag{5.46}$$

f is the angular distribution here.

In Figure 5.41 the log likelihood distributions for α_2 are shown in the four p_T ranges. To estimate the sensitivity of this experiment, the χ^2 of the α_2 distribution is calculated with respect to the next-to-leading order QCD prediction and with respect to (V-A) theory in the absence of QCD. The χ^2 with respect to the no-QCD prediction is 8.3/4 dof which corresponds to a probability of 8% while the χ^2 with respect to the next-to-leading order QCD prediction is 1.0/4 dof which corresponds to a probability of 91%.

An alternative way to estimate the significance of this measurement makes use of an odds-ratio approach:

$$R = \frac{\prod_i p_i(\alpha_2(NLO\,QCD))}{\prod_i p_i(\alpha_2(no\,QCD))} \tag{5.47}$$

where the product is over p_T-bins, $p_i(NLOQCD)$ is the normalized probability at the predicted value for α_2 for p_T-bin i, $p_i(noQCD)$ is the normalized probability

at the predicted value for (V-A) theory without QCD effects, i.e. at $\alpha_2 = 1.0$. $\log(R) = 0.5$ corresponds then to a 1σ separation. We measure $\log(R) = 2.55$ which corresponds to 2.3σ. The likelihood distributions are shown in Figure 5.42.

The results of this measurement are summarized in Figure 5.43 and table 5.9.[17]

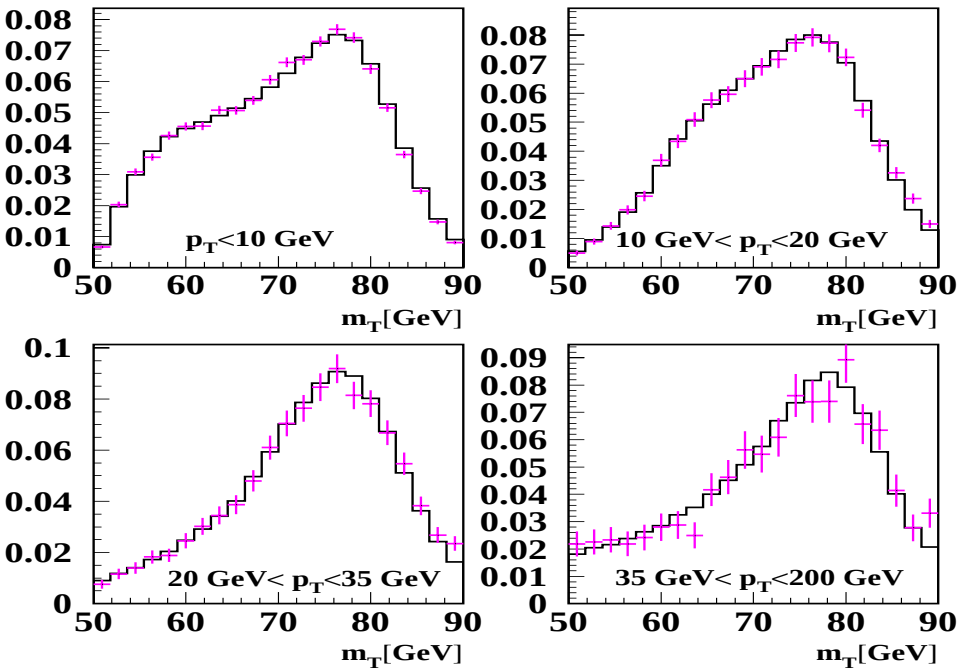

Figure 5.39: Background subtracted transverse mass distribution in four p_T bins compared to CMS.

[17] These errors are very close to the ones obtained with the Monte Carlo Study (see table 5.1).

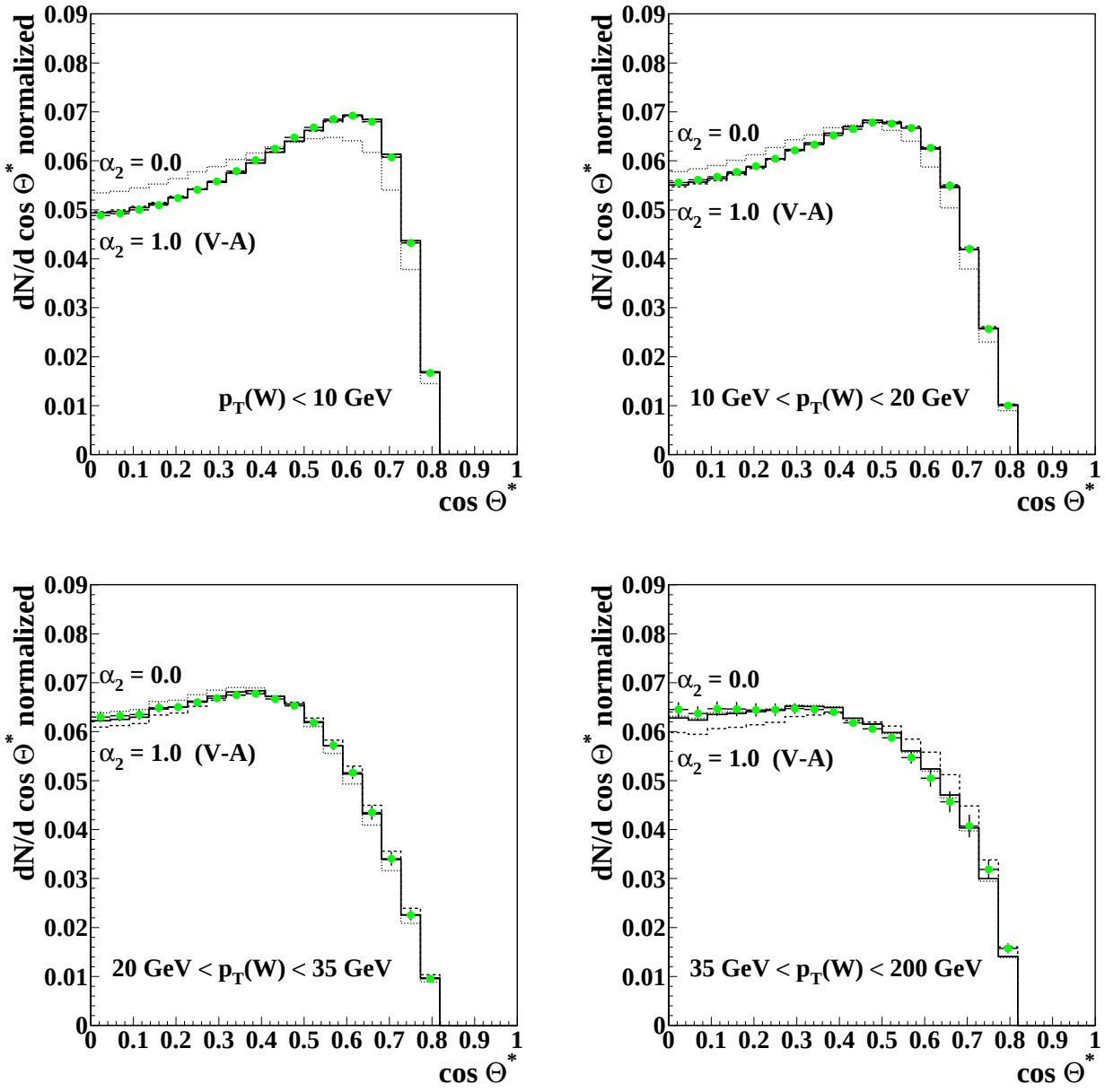

Figure 5.40: Angular distributions for data compared to CMS templates for four different p_T bins. Shown are the templates that fit best (black) and the templates for $\alpha_2 = 1.0$ (dashed) and $\alpha_2 = 0.0$ (dotted).

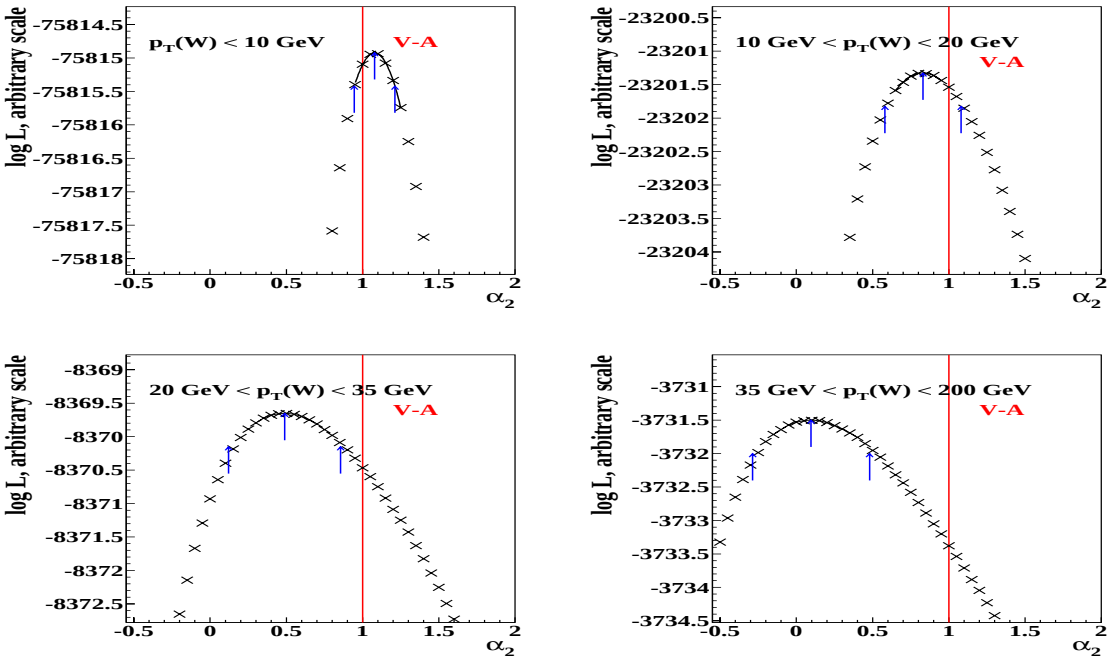

Figure 5.41: Log likelihood functions for four different p_T bins.

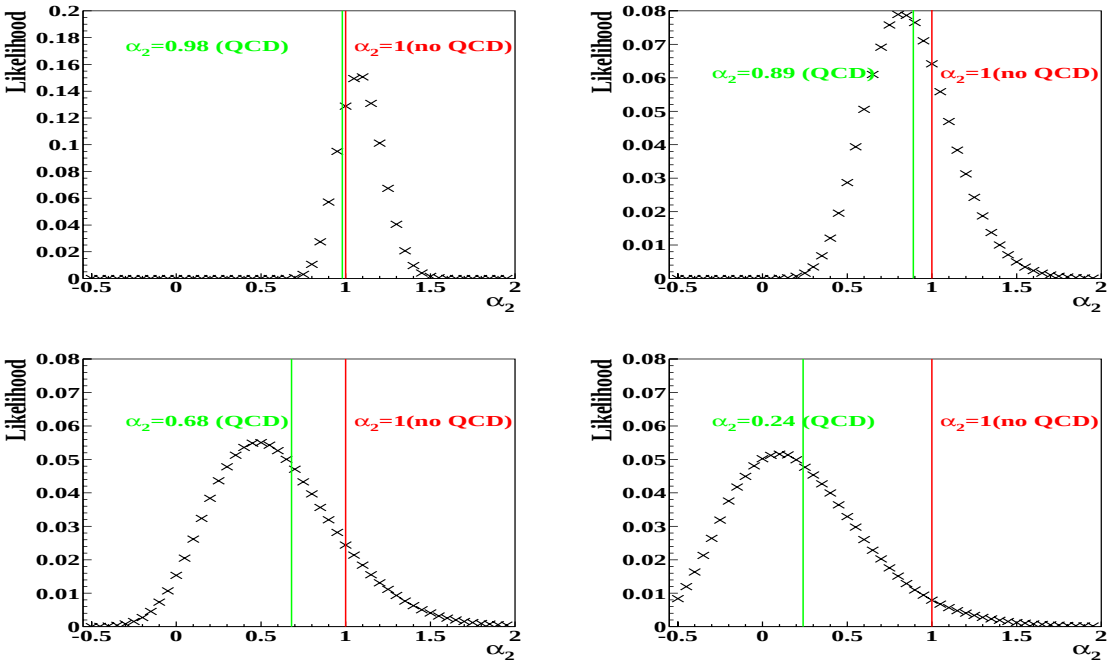

Figure 5.42: Likelihood functions for four different p_T bins. The horizontal lines mark the predictions from the QCD calculation (lighter grey) and from $(V-A)$ theory without QCD (darker grey).

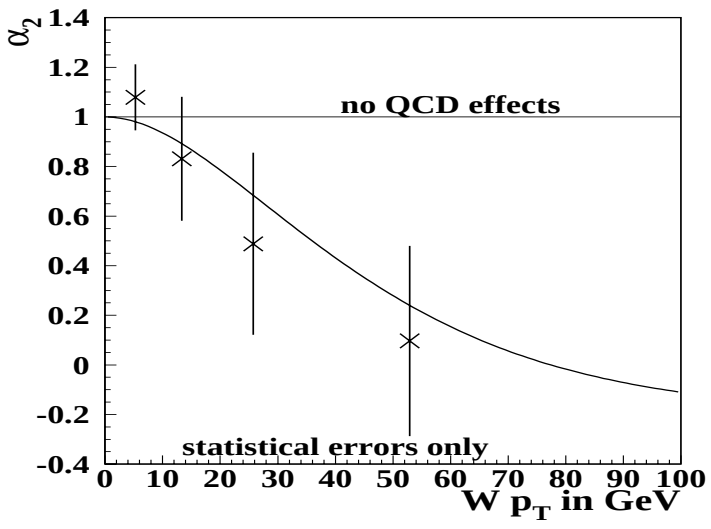

Figure 5.43: Measured α_2 as a function of p_T and its statistical errors.

5.5 Systematic errors

In this section we will discuss the sources of systematic errors for the measurement of α_2 and the estimation of the sizes of these errors. In general, all systematic errors in this analysis are estimated by changing the corresponding parameter by its error (one σ) and rerunning the analysis code. For the uncertainties due to background estimations this implies subtracting backgrounds with shapes and overall rates changed by their errors and rerunning with a modified background subtracted transverse mass distribution. All other systematic errors concern the detector modeling in CMS and are estimated by varying the corresponding Monte Carlo parameter and rerunning the analysis code to extract the varied α_2.

The errors due to uncertainties in the backgrounds are first estimated by redoing the analysis without any background subtraction (See table 5.6). The errors of α_2 obtained this way are upper limits for the true errors due to background subtraction since the uncertainties in the backgrounds are less than 100%.

For the Z background, the transverse mass spectra are fit with heuristic functions (Gaussians for the two lowest p_T bins, a double-Gaussian for the third bin and a straight line for the highest p_T bin). An upper limit for the error on these fit m_T-distributions is obtained by calculating the difference in the number of background events before and after cafix jet corrections were applied to the Herwig Z Monte Carlo sample. The overall Z background after cafix scale corrections is 34% higher than before. The overall normalization of these fits is then varied by this difference and the analysis is repeated for the varied Z background.

The transverse mass spectra for QCD multijet and $t\bar{t}$ background events are also fit with appropriate functions. The errors in the measurement of α_2 due to uncertainties in the background shapes and overall rates are again estimated by varying the fit parameters and the overall rates by their errors and rerunning the analysis code. Table 5.7 lists the errors of α_2 due to the various backgrounds.

Table 5.8 lists the α_2 values obtained when the hadronic scale and resolution parameters in CMS are varied by 1σ. In table 5.9 all sources of systematic errors are listed.

The error due to the choice of α_1 as a function of p_T^W is estimated by fixing α_1 to the value predicted by a theory without QCD effects ($\alpha_1 = 2$) and rerunning the analysis code.

p_T	α_2	$\alpha_{2,no\ backgrounds\ subtracted}$	difference
0-10	1.07 ± 0.13	1.08 ± 0.13	0.01
10-20	0.82 ± 0.25	0.92 ± 0.26	0.10
20-35	0.49 ± 0.37	0.62 ± 0.37	0.13
35-200	0.10 ± 0.37	0.38 ± 0.41	0.28

Table 5.6: Values of α_2 when no backgrounds are subtracted and systematic shifts of α_2 due to background subtraction.

p_T	$\Delta\alpha_2$ for Z	$\Delta\alpha_2$ for Z shape	$\Delta\alpha_2$ for top	$\Delta\alpha_2$ for QCD	$\Delta\alpha_2$ for QCD shape
0-10	± 0.01	± 0.00	± 0.00	± 0.02	± 0.04
10-20	± 0.02	± 0.01	± 0.00	± 0.05	± 0.01
20-35	± 0.02	± 0.01	± 0.00	± 0.09	± 0.03
35-200	± 0.04	± 0.02	± 0.01	± 0.07	± 0.01

Table 5.7: Systematic error due to uncertainties for the separate backgrounds. The errors due to the uncertainties of the overall background rates and the ones due to the errors in the shape parameters are listed separately.

p_T	$\Delta\alpha_2(\alpha_{HAD})$	$\Delta\alpha_2(\beta_{HAD})$	$\Delta\alpha_2(\gamma_{HAD})$	$\Delta\alpha_2(\delta_{HAD})$	$\Delta\alpha_2(S_{rec})$	$\Delta\alpha_2(\alpha_{mb})$
0-10			± 0.02	± 0.02	± 0.01	± 0.02
10-20	± 0.01	± 0.01			± 0.00	± 0.03
20-35	± 0.03	± 0.03			± 0.01	± 0.02
35-200	± 0.04	± 0.02			± 0.05	± 0.05

Table 5.8: Changed α_2 values obtained by rerunning the analysis with Monte Carlo parameters that are varied by 1 σ.

5.5.1 Conclusion on systematic errors

Except for the first p_T bin, the combined systematic errors on α_2 are less than half of the size of the statistical errors. The dominant systematic errors are due to uncertainties in the QCD multijet background, the electromagnetic energy scale, and in the recoil resolution parameters in the Monte Carlo. The estimation of both the QCD background and the hadronic resolution parameters are themselves statistically limited since they are obtained from data.

In the case of the QCD background, the trigger used for events without a missing E_T requirement was heavily prescaled. The hadronic response and resolution are estimated from $Z \to ee$ events of which we only had about 5000 in Run 1.

Both the error due to the QCD background and the one due to the uncertainty in the recoil resolution will be reduced in Run II when much better statistics will be available. For a more detailed discussion on the expected errors for Run II see appendix D.

p_T	$0 \leq p_T \leq 10$	$10 \leq p_T \leq 20$	$20 \leq p_T \leq 35$	$35 \leq p_T \leq 200$
α_2	1.07 ± 0.13	0.82 ± 0.25	0.49 ± 0.37	0.10 ± 0.37
α_2, *predicted*	0.98	0.89	0.68	0.24
mean p_T	5.3	13.3	25.7	52.9
error QCD	± 0.02	± 0.05	± 0.09	± 0.07
error QCD shape	± 0.04	± 0.01	± 0.03	± 0.01
error Z	± 0.01	± 0.02	± 0.02	± 0.04
error Z shape	± 0.00	± 0.01	± 0.01	± 0.02
error top	± 0.00	± 0.00	± 0.00	± 0.02
error α_{EM}	± 0.06	± 0.05	± 0.03	± 0.04
error α_{HAD}		± 0.01	± 0.03	± 0.04
error β_{HAD}		± 0.01	± 0.03	± 0.02
error γ_{HAD}	± 0.02			
error δ_{HAD}	± 0.02			
error S_{rec}	± 0.01	± 0.01	± 0.04	± 0.04
error $\alpha_{minbias}$	± 0.02	± 0.02	± 0.03	± 0.05
error due to α_1	± 0.01	± 0.05	± 0.03	± 0.03
combined systematic error	± 0.08	± 0.09	± 0.12	± 0.12

Table 5.9: Central values for α_2 with statistical and systematic errors.

5.6 Conclusion

We have successfully measured the angular distribution of electrons from W boson decays using Bayesian statistics to extract the lepton angle from the transverse mass of the W boson. The preference for a calculation to next-to-leading order in perturbative QCD is estimated to be about 2 σ. The uncertainties in this measurement are dominated by statistics, the systematic errors are more than a factor of two smaller than the statistical errors.

Bibliography

[1] Particle Data Group, "Review of Particle Physics," European Physical Journal **C3**, 1 (1998).

[2] J.C. Collins, D.E. Soper. *Nucl. Phys. B 193,381 (1981); B213, 545E (1983); J.C. Collins, D.E. Soper, G. Sterman, ibid. B250, 199 (1985)*

[3] C. Balazs and C.-P. Yuan, Phys.Rev. **D56** 5558-5583,1997

[4] I.J.R. Aitchison and A.J.G. Hey, Gauge Theories in Particle Physics, Institute of Physics Publishing, Bristol and Philadelphia, 1993

[5] P. Aurenche, The Standard Model of particle physics, *hep-ph/9712342 (1997)*

[6] R. J. Cashmore, C. M Hawkes, B. W. Lynn, R. G. Stuart , *Z. Phys. C 30, 125 (1986)*

[7] E. Mirkes. *Nuclear Physics, B 387 3 (1992)*

[8] S. Abachi et al., Nucl Instr. Meth. **A338**,185,1994

[9] *Phys. Rev. Lett. 74, 2632 (1995).*

[10] J. Thompson, "Introduction to Colliding Beams at Fermilab," Fermilab Tech. Memo. TM-1909, October 1994.

[11] S. Abachi et al., *Nucl. Instr. and Methods*, **A338, 185**, 1994

[12] D. Green, Fermilab, "The Physics of Particle Detectors", unpublished textbook, Graduate Student Association Summer School, Aug 1997

[13] Design Report, The DØ Experiment at the Fermilab p-$\overline{p}$ Collider, November 1994

[14] S. Snyder *DØ internal note 2500*

[15] A. R. Clark et al., *Nucl. Instr. and Methods*, **A315, 193**, 1992

[16] J. Kadyk, *Nucl. Instr. and Methods*, **A300, 436**, 1991

[17] J. F. Detœuf et al., *Nucl. Instr. and Methods*, **A279, 310-316**, 1989

[18] Y. Ducros et al., *Nucl. Instr. and Methods*, **A277, 401-406**, 1989

[19] "The Central Drift Chamber for the DØ Experiment: Design, Construction and Test", Ties Behnke, Ph.D Thesis, State University of New York at Stony Brook, August 1989 (unpublished).

[20] "Results from a Beam Test of the DØ Forward Drift Chambers", R. Avery et al., IEEE Trans. Nucl. Science (1992).

[21] Hugh Montgomery, private communication

[22] Harry Weerts, private communication

[23] C.Fabjan. Calorimetry in high-energy physics. In: Thomas Ferbel, editor, Experimental Techniques in High Energy Physics, pages 257 - 324. Addison-Wesley, 1987

[24] J. Kotcher, Response of the DØ calorimeter to Cosmic Ray Muons. PhD. thesis, New York University, New York, 1992 (unpublished)

[25] M. Abolins et al., "The level one framework" *DØ internal note 328 revised, DØ internal note 705, 1988.*

[26] M. Abolins et al., *IEEE Trans. Nucl. Sci.*, **36(1):384-389**, 1989

[27] M. Abolins, D. Edmunds, P.Laurens, and B. Pi, *Nucl. Instr. and Methods*, **A289:543-560**, 1990

[28] J. Drinkard, "The DØ Level 1.5 Calorimeter Trigger," *DØ internal note 2274*

[29] R. Genik, "A DSP Based Electromagnetic Trigger for the DØ Detector," in: Procedings of the 1995 IEEE Conference on Real Time Computer Applications in Nuclear, Particle, and Plasma Physics, East Lansing, Michigan (1995)

[30] The Zebra manual is available at: http://consult.cern.ch/writeup/zebra/

[31] "The DØ Upgrade" Fermilab Pub-96/357-E available at: http://higgs.physics.lsa.umich.edu/dzero/d0doc96/d0doc.html

[32] "DØ Technical Design Summary", *DØ internal note 2962*

[33] T. Behnke, "The Central Drift Chamber for te DØ Detector: Design, Construction, and Test." PhD Thesis, State University of New York at Stony Brook, Stony Brook, New York, 1989,(unpublished).

[34] D. Pizzuto, DØ Central Tracking Performance Studies, PhD Thesis, State University of New York at Stony Brook, Stony Brook, New York, 1991(unpublished).

[35] S. Rajagopalan, The dE/dx Capabilities of the DØ tracking system. PhD thesis, Northwestern University, Evanston, Illinois, 1992 (unpublished).

[36] J.W. Bantly, The DØ Forward Drift Chamber performance and Physics Capability in the 1990 FNAL Testbeam Run. PhD thesis, Northwestern University, Evanston, Il, 1992 (unpublished).

[37] P. Grudberg, Measurement of the W and Z Boson Production Cross Sections in $p\overline{p}$ Collisions at $\sqrt{s} = 1.8$ TeV with the DØ Detector, PhD thesis, University of California at Irvine, Irvine, California, 1997 (unpublished).

[38] R. Raja et al., "Reconstruction and Analysis: Tracking Packages, CalorimeterPackages," *DØ internal note 1006 (1990)*

[39] R. Raja, "H-matrix Analysis for top→lepton + jets," *DØ internal note 1192 (1992)*

[40] M. Narain, "Electron Identification in the DØ Detector", in: Proceedings of the American Physical Society Division of Particles and Fields Conference, Fermilab, Batavia, Illinois (1992).

[41] S. Glenn, A Search for Self Interactions of Neutral Electroweak Gauge Bosons. PhD thesis, University of California at Davis, Davis, California, 1996(unpublished).

[42] M. Narain *DØ internal note 2386*

[43] M. Narain, U. Heintz, *DØ internal note 2355*

[44] D. Casey, T. Joffe-Minor, J. Tarazi, *DØ internal note 3124*

[45] J.C. Collins, D.E. Soper. *Phys. Rev. D 16,2219, (1977)*

[46] B. Abbott et al., *Phys. Rev. D 58, 092003 (1998)*

[47] B. Abbott et al., *Phys. Rev. Lett. 80, 3000 (1998).*

[48] *DØ internal note 3198*

[49] TEV 2000, *Fermilab Pub 96/082*

[50] G, Arnison et al.(UA1 collaboration), *Phys.Lett.166B:484,(1986)*

[51] E.Locci. *Proc. 8th European Symp. on Nucleon-Antinucleon Interactions, Thessaloniki,(1986)*

[52] C. Albajar et al.(UA1 collaboration), *Z,Phys. C 44:15,(1989)*

[53] M. I. Martin. *1994, thesis (unpublished)*

[54] E. T. Jaynes, "Probability Theory: The Logic of Science", unpublished available at http://bayes.wustl.edu/etj/prob.html

[55] Eric Flattum, *PhD thesis, Michigan State University, 1996 (unpublished)*

[56] I. Adam, *PhD thesis, Columbia University, 1997 (unpublished), Nevis Report #294*

[57] B. Abbott et al, *Physics Rev. Lett. 80 5498 (1998)*

[58] G. Marchesini et al, *Computer Physics Communications,* **67** *465 (1989)*

[59] P. B. Arnold and M. H. Reno, Nucl. Phys. **B319**, 37 (1989). Erratum, Nucl. Phys. **B330**, 284 (1990).

[60] G. A. Ladinsky and C. P. Yuan, *Phys. Rev. D* **50**, *4239 (1994).*

[61] B. Abbott et al., "Measurement of the Transverse Momentum of Z Boson produced in $p\overline{p}$ Collisions at $\sqrt{s} = 1.8$ TeV" *to be published in Phys.Rev., D*

[62] F. A. Berends and R. Kleiss, Zeit. Phys. **C27** 365(1985)

[63] F. Paige and S. Protopopescu, ISAJET 5.20: A Monte Carlo Event Generator for pp and $\overline{p}p$ Reactions. *BNL-38034 (1996)*

[64] I. Adam et al. *DØ internal note 2298*

[65] U. Heintz, *DØ internal note 2268*

[66] Miguel Mostafá, *DØ internal note 3550*

[67] R. Kehoe, R. Astur, *DØ internal note 2908*

[68] V. Daniel Elvira, *DØ internal note 3139*

[69] Jamal Tarazi, *PhD thesis, University of California, Irvine, Irvine(1997) (unpublished)*

[70] "Measurement of the transverse momentum of dielectron pairs in proton-antiproton collisions ", D. Casey, PhD Thesis, Univ. of Rochester, 1997.

[71] J. Botts *et al.* (CTEQ Collaboration), Phys. Lett. B **304**, 159 (1993); H.L. Lai *et al.* (CTEQ Collaboration), Phys. Rev. D **51**, 4763 (1995); H.L. Lai *et al.* (CTEQ Collaboration), Phys. Rev. D **55**, 1280 (1997).

[72] B. Abbott et al., *hep-ex/9906025, to be published in Phys.Rev., D*

[73] C. Gerber *DØ internal note 3343*

[74] P. Grudberg *DØ internal note 2316*

[75] D. Pušeljić *DØ internal note 2316*

[76] B. Abbott et al., *Phys. Rev. D 60, 012001 (1999)*

[77] P. B. Arnold and R. P. Kauffman, Nucl. Phys. **B349**, 381 (1991).

Appendix A

The Collins-Soper Frame

The measurement of the decay angle of the charged lepton in the W rest frame gets complicated by the fact that the W rest frame cannot be reconstructed unambiguously since the longitudinal component of the neutrino momentum cannot be measured in a collider detector. In a specific restframe of the W Boson, the Collins-Soper frame, this ambiguity can be hidden in the W mass. For this reason theorists have used this frame in the calculation of helicity amplitudes for vector boson production. The transformation from the laboratory frame to the Collins-Soper frame is done in three steps:

- a rotation around the z-axis so that the p_T^W is oriented along x;
- a boost along z so that the W-boson is at rest with respect to the z-axis;
- a boost along the new x-axis so that the W is completely at rest.

In the Collins-Soper frame, the z-axis bisects the direction of the proton and negative antiproton momentum as we will show in section A.1. For an illustration of the orientation of the axis see figure A.1. Note, that the Collins-Soper frame is a restframe of the W boson, hence the transverse momentum vector, p_T^W, vanishes in

this frame. The p_T^W vector shown in figure A.1 is included for illustrative purposes and is understood to be evaluated in the rotated frame before the final boost along the new x-axis.

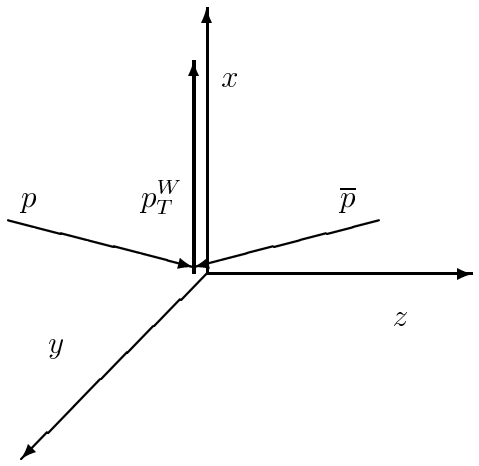

Figure A.1: The Collins-Soper frame: The z axis bisects the proton and negative antiproton momentum. The p_T^W vector shown is evaluated before the final boost along x.

A.0.1 Transformation from Laboratory Frame to CS Frame

In the previous section we have briefly mentioned the three steps in which the transformation from the lab frame to the Collins-Soper frame is performed. Here we show explicitly what the transformation looks like and we prove that the direction of the charged lepton in the Collins-Soper frame is in fact independent of the neutrino momentum. Denote the charged lepton and neutrino four-momenta in

the lab frame as:

$$P^e_{lab} = (E^e,\, p^e_x,\, p^e_y,\, p^e_z) \tag{A.1}$$

and

$$P^\nu_{lab} = (E^\nu,\, p^\nu_x,\, p^\nu_y,\, p^\nu_z) \tag{A.2}$$

The momentum of the W boson in the lab frame is just the sum of the electron and the neutrino momentum:

$$P^W_{lab} = P^e_{lab} + P^\nu_{lab} = (E^e + E^\nu,\, p^e_x + p^\nu_x,\, p^e_y + p^\nu_y,\, p^e_z + p^\nu_z) \tag{A.3}$$

The first step is a rotation by an angle α around the z-axis so that the transverse momentum of the W boson is parallel to the x-axis:

$$\alpha = \cos^{-1}\left(\frac{p^W_x}{\sqrt{p^W_x + p^W_y}}\right) \tag{A.4}$$

In this intermediate frame the momenta are:

$$P^W_{rot} = (E^W_{rot},\, p^W_{x\,rot},\, 0,\, p^W_{z\,rot}) \tag{A.5}$$

$$P^e_{rot} = (E^e_{rot},\, p^e_{x\,rot},\, p^e_{y\,rot},\, p^e_{z\,rot}) \tag{A.6}$$

and

$$P^\nu_{rot} = (E^\nu_{rot},\, p^\nu_{x\,rot},\, -p^e_{y\,rot},\, p^\nu_{z\,rot}) \tag{A.7}$$

The next step is a boost in x direction of the rotated frame. After this boost the momentum of the W boson is:

$$P^W_{z-boosted} = \left(\sqrt{(E^W_{z\,rot})^2 - (p^W_{x\,rot})^2},\, p^W_{x\,rot},\, 0,\, 0\right) \tag{A.8}$$

The boosted electron momentum becomes:

$$P^e_{z-boosted} = \left(\frac{E^e_{rot}E^W_{rot} - p^e_{z\,rot}p^W_{z\,rot}}{\sqrt{(E^W_{rot})^2 - (p^W_{z\,rot})^2}},\, p^e_{x\,rot},\, p^e_{y\,rot},\, \frac{p^e_{z\,rot}E^W_{rot} - E^e_{rot}p^W_{z\,rot}}{\sqrt{(E^W_{rot})^2 - (p^W_{z\,rot})^2}}\right) \tag{A.9}$$

The last step is the boost into the Collins-Soper frame along the x direction, resulting in the W at rest:

$$P^W_{CS} = \left(E^W_{CS},\, 0,\, 0,\, 0\right) = \left(\sqrt{(E^W_{rot})^2 - (p^W_{x\,rot})^2 - (p^W_{z\,rot})^2}, 0, 0, 0\right) \tag{A.10}$$

The lepton momentum vector in the Collins-Soper frame is:

$$\begin{aligned} P^e_{CS} &= (E^e_{CS},\, p^e_{x\,CS},\, p^e_{y\,CS},\, p^e_{z\,CS}) \\ &= \left(\frac{E^e E^W - p^e_x p^W_x - p^e_z p^W_z}{m_W},\, \frac{p^e_x (E^W)^2 - E^e E^W p^W_x - p^e_x (p^W_z)^2 + p^e_z p^W_x p^W_z}{m_W \sqrt{(E^W)^2 - (p^W_z)^2}},\, p^e_y,\, \frac{p^e_z E^W - E^e p^W_z}{\sqrt{(E^W)^2 - (p^e_W)^2}}\right) \end{aligned} \tag{A.11}$$

where all momenta are evaluated in the rotated frame. In equation A.11 the expression for the W mass has been substituted:

$$m_W = \sqrt{(E^W)^2 - (p^W_x)^2 - (p^W_z)^2} \tag{A.12}$$

Please note that for readability the subscript "rot" has been dropped from equation A.11 on. All momenta in the following section are understood to be evaluated in the rotated frame unless denoted otherwise.

A.0.2 Independence from Longitudinal Neutrino Momentum

We have stated that in the Collins-Soper frame the expression for the lepton angle does not explicitly include the longitudinal neutrino momentum. To show that this is true we have to rewrite the transverse momentum of the charged lepton in a form independent of the longitudinal neutrino momentum. The x component of the electron momentum in the Collins-Soper frame is given in equation A.11:

$$P^e_{x\,CS} = \frac{p^e_x (E^W)^2 - E^e E^W p^W_x - p^e_x (p^W_z)^2 + p^e_z p^W_x p^W_z}{m_W \sqrt{(E^W)^2 - (p^W_z)^2}} \tag{A.13}$$

The dependence on p_z^ν comes in through p_z^W and E^W. The denominator can simply be rewritten as:

$$m_W\sqrt{(E^W)^2-(p_z^W)^2} = m_W\sqrt{m_W^2+(p_T^W)^2} \tag{A.14}$$

The numerator can be written as follows:

$$\begin{aligned} & p_x^e(E^W)^2 - E^eE^Wp_x^W - p_x^e(p_z^W)^2 + p_z^ep_x^Wp_z^W \\ & = p_x^e((E^W)^2-(p_x^W)^2-(p_z^W)^2) + p_x^e(p_x^W)^2 - E^eE^Wp_x^W + p_z^ep_x^Wp_z^W \end{aligned} \tag{A.15}$$

This can be rewritten, using A.12 and A.5:

$$= m_W^2p_x^e + p_x^W(p_x^ep_x^W + p_y^ep_y^W + p_z^ep_z^W - E^eE^W) \tag{A.16}$$

With $P^W = P^e + P^\nu$ we get:

$$\begin{aligned} & = m_W^2p_x^e + (p_x^e+p_x^\nu)(p_x^e(p_x^e+p_x^\nu) \\ & +p_y^e(p_y^e+p_y^\nu) + p_z^e(p_z^e+p_z^\nu) - E^e(E^e+E^\nu)) \end{aligned} \tag{A.17}$$

After carrying out the multiplication, this becomes:

$$\begin{aligned} & = m_W^2p_x^e + (p_x^e+p_x^\nu)((p_x^e)^2+(p_y^e)^2+(p_z^e)^2-(E^e)^2) \\ & +(p_x^e+p_x^\nu)(p_x^ep_x^\nu + p_y^ep_y^\nu + p_z^ep_z^\nu - E^eE^\nu) \end{aligned} \tag{A.18}$$

Substituting masses for the electron and W boson, we get

$$= m_W^2p_x^e + (p_x^e+p_x^\nu)m_e^2 - (p_x^e+p_x^\nu)\frac{m_W^2}{2} = m_W^2p_x^e - (p_x^e+p_x^\nu)\frac{m_W^2}{2} \tag{A.19}$$

Using A.13 and A.14, the x component of the charged lepton in the Collins-Soper frame finally becomes:

$$p_{x\,CS}^e = \frac{m_W(p_x^e-p_x^\nu)}{2\sqrt{m_W^2+(p_T^W)^2}} \tag{A.20}$$

To calculate the polar angle θ^*, the expression for the z component of the electron momentum in the Collins-Soper frame is needed. It can easily be obtained with the help of the following expression for any restframe of the W:

$$E_{W\,at\,rest}^e = E_{W\,at\,rest}^\nu = \frac{m_W}{2} \tag{A.21}$$

It follows that

$$(p^e_{x\,CS})^2 + (p^e_{y\,CS})^2 + (p^e_{z\,CS})^2 = \frac{m_W^2}{4} \tag{A.22}$$

which leads to

$$p^e_{z\,CS} = \pm\sqrt{(\frac{1}{2}m_W)^2 - (p^e_{x\,CS})^2 - (p^e_{y\,CS})^2} \tag{A.23}$$

This can now be rewritten in terms of m_W and the transverse momenta of the electron and the neutrino:

$$p^e_{z\,CS} = \pm\frac{1}{2}\sqrt{m_W^2 - \frac{m_W^2(p^e_x - p^\nu_x)^2}{m_W^2 + (p_T^W)^2} - (p^e_y - p^\nu_y)^2} \tag{A.24}$$

Now we can use A.24 and A.21 to finally express the lepton angle in the Collins-Soper frame:

$$\cos\theta^* = \frac{p^e_{z\,CS}}{E^e_{CS}} = \pm\sqrt{1 - \frac{(p^e_{x\,CS})^2 + (p^e_{y\,CS})^2}{(\frac{1}{2}m_W)^2}} = \pm\sqrt{1 - \left(\frac{p^e_{T\,CS}}{\frac{1}{2}m_W}\right)^2} \tag{A.25}$$

Equation A.25 shows that in the Collins-Soper frame the polar angle $\cos\theta^*$ is not directly dependent on the longitudinal momentum of the neutrino. The dependence is implicitly contained in the W mass which varies from event to event. The ambiguity in reconstructing the restframe of the W boson appears as a sign in the term for the angle $\cos\theta^*$.

A.1 Orientation of the CS frame with respect to the Lab Frame

In the lab frame, the momenta of the proton and antiproton can be written as follows (assuming that the transverse components are negligible):

$$P_{lab} = \frac{1}{\sqrt{2}}(1, 0, 0, 1) \tag{A.26}$$

and

$$\overline{P}_{lab} = \frac{1}{\sqrt{2}}(1, 0, 0, -1) \tag{A.27}$$

After the transformation to the Collins-Soper frame, these become

$$P_{CS} = \frac{E^W - p_z^W}{\sqrt{2} m_W \sqrt{m_W^2 + (p_T^W)^2}} \times (\sqrt{m_W^2 + (p_T^W)^2}, -p_T^W, 0, m_W) \tag{A.28}$$

and

$$\overline{P}_{CS} = \frac{E^W - p_z^W}{\sqrt{2} m_W \sqrt{m_W^2 + (p_T^W)^2}} \times (\sqrt{m_W^2 + (p_T^W)^2}, -p_T^W, 0, -m_W) \tag{A.29}$$

These equations show that the z-axis in the Collins-Soper frame bisects the angle formed by the proton and negative antiproton direction. It should be noted that in the Collins-Soper frame, the proton and antiproton axis are not collinear since the transformation from the lab frame to the Collins-Soper frame involves a boost along the transverse momentum of the W boson.

Appendix B

$p_T - y$ Grids

The differential cross section in Boson p_T and y enters the CMS Monte Carlo as a two dimensional histogram. CMS allows for two different options of how these grids enter the program. It either accepts a single grid for W^--Bosons which then gets reflected in y to produce the CP-transformed grid for W^+-Bosons. The other option is to provide CMS with two separate grids, called the A and the B grid, both for W^-. These two also are swapped in y, so that with this option one ends up with four grids. The A grid corresponds to the case when the quark comes from the proton and the antiquark from the antiproton which is the case 100% of the time for valence-valence and valence-sea interactions and 50% of the time for sea-sea interactions. The remaining 50% of the time (for sea-sea interactions) the quark comes from the antiproton and the antiquark from the proton in which case the B grid is used. Since sea-sea interactions occur only about 20% of the time, the B grid only amounts to 10% of all interactions. The A grid corresponds to a $1 + P\cos\theta^* + \cos^2\theta^*$ decay while the B grid corresponds to $1 - P\cos\theta^* + \cos^2\theta^*$.

This analysis has been done using separate grids as described above because the A and the B grid each correspond to a distinct angular decay distribution. Since the Monte Carlo program chooses the correct sign in front of the $\cos\theta^*$ term

dependent on the polarization of the W, the corresponding p_T-y grid should be chosen. However, we started this analysis using a different theory for the production of W bosons based on a combined calculation for the resummation part and the perturbative part of the W cross section by Arnold and Kauffman [77]. We wanted to start from a grid which is the result of a published calculation and has been used in several DØ publications. That particular calculation did not allow for separate helicity grids and we estimated the error due to choosing only one grid for the total cross section that corresponds to A+B.

The systematic difference between using separate grids and a single combined grid is shown in table B.1. The effect is (except for the first bin) well below the statistical significance of this measurement. Since the final version of this analysis uses separate grids, this study has only historical value. It is good to see, however, that the error due to different p_T-y grid choices is small.

p_T	$0 \leq p_T \leq 10$	$10 \leq p_T \leq 20$	$20 \leq p_T \leq 35$	$35 \leq p_T \leq 200$
$\Delta\alpha_2$	-0.1	-0.06	-0.1	-0.04

Table B.1: Change in the measured α_2 due to using separate grids instead of a single grid. This study is done using the resummation calculation by Ladinsky and Yuan combined with the perturbative calculation by Arnold and Reno.

Appendix C

The Matrix Method

Consider two sets of W selection cuts, one labeled loose[1], the other tight cuts. Efficiencies are calculated with respect to the loose cuts and events that pass loose cuts belong to the parent sample M (for mother). The parent sample can then be divided in two different ways: First,

$$M = P + F \tag{C.1}$$

where P is the number of events that pass the tight set of cuts and F is the number of events that fail. Second,

$$M = R + B \tag{C.2}$$

where R is the number of real $W \to e\nu$ events in the loose sample and B is the number of background events. P can then be written as:

$$P = \epsilon_s R + \epsilon_j B \tag{C.3}$$

[1]Loose here stands for any set of selection criteria less stringent than the tight cuts. It is not identical to the specific definition for a loose electron used in this analysis: In this measurement the criteria for a mother electron are used as the looser superset of events when applying the matrix method.

where ϵ_s is the efficiency of the tight cuts relative to the parent sample for real electrons (measured from $Z \to ee$ events) and ϵ_j is the efficiency for jets passing the tight cuts. In matrix form, including the expression for F, this can be written as:

$$\begin{pmatrix} P \\ F \end{pmatrix} = \begin{pmatrix} \epsilon_s & \epsilon_j \\ 1-\epsilon_s & 1-\epsilon_j \end{pmatrix} \begin{pmatrix} R \\ B \end{pmatrix} \tag{C.4}$$

The number of QCD multijet background events in the tight sample can then be written as:

$$N^W_{QCD} = \epsilon_j B \tag{C.5}$$

and the background fraction is

$$f^W_{QCD} = \frac{\epsilon_j B}{P} \tag{C.6}$$

To express this in terms of the known parameters $M, P, \epsilon_s, \epsilon_j$, the matrix in equation C.4 has to be inverted[2]:

$$\begin{pmatrix} R \\ B \end{pmatrix} = \frac{1}{\epsilon_S - \epsilon_j} \begin{pmatrix} 1-\epsilon_j & -\epsilon_j \\ -(1-\epsilon_s) & \epsilon_s \end{pmatrix} \begin{pmatrix} P \\ M-P \end{pmatrix} \tag{C.7}$$

where the first one of the following additional constraints has been used:

$$M = P + F \qquad\qquad M = R + B \tag{C.8}$$

From equation C.7 the expression for B can be derived:

$$B = \frac{\epsilon_s M - P}{\epsilon_s - \epsilon_j} \tag{C.9}$$

and, using equation C.6, the background fraction becomes

$$f^W_{QCD} = \frac{\epsilon_j}{P} \frac{\epsilon_s M - P}{\epsilon_s - \epsilon_j} \tag{C.10}$$

[2]Since $\epsilon_j \neq \epsilon_s$, the matrix is not singular and can be inverted.

Appendix D

Perspectives for Run II

The measurement of the angular distribution of electrons from W bosons with Run I data is statistically limited. While a calculation that includes QCD effects is preferred over one that does not, this preference is not strong enough to exclude a p_T independent angular parameter α_2. With the next collider run starting in the near future, it is worthwhile looking at the sensitivity of this measurement in Run II. In the following discussion, we estimate the size of statistical and systematic errors for Run II.

D.1 Errors in Run II

The expected statistical errors for Run II are easy to estimate: The statistical errors simply scale like the inverse of the square root of the number of events. We consequently have to calculate the expected number of W boson events under Run II conditions. We get a factor of 57 in W boson statistics which breaks down as follows (see [49]):

$$\frac{N_{W,RunII}}{N_{W,RunI}} = f_{luminosity} \times \ f_{2.0\,\mathrm{TeV}} \times \frac{N_e + N_\mu}{N_e} \times \ \frac{\epsilon_{tracking}}{\epsilon_{no\,tracking}} \qquad \text{(D.1)}$$

where $f_{luminosity} = 20$ indicates the increase in luminosity, $f_{2.0TeV} = 1.2$ indicates the increase in W cross section due to the increase of the center-of-mass energy from 1.8 TeV to 2 TeV, $\frac{N_e+N_\mu}{N_e} = 2$ is the additional statistics gained by including the muon channel, and $\frac{\epsilon_{tracking}}{\epsilon_{no\,tracking}} = \frac{0.95}{0.8}$ is the increase in efficiency due to tracking. The statistical errors of the Run I measurement are scaled by $1/\sqrt{57}$ as shown in figure D.1.

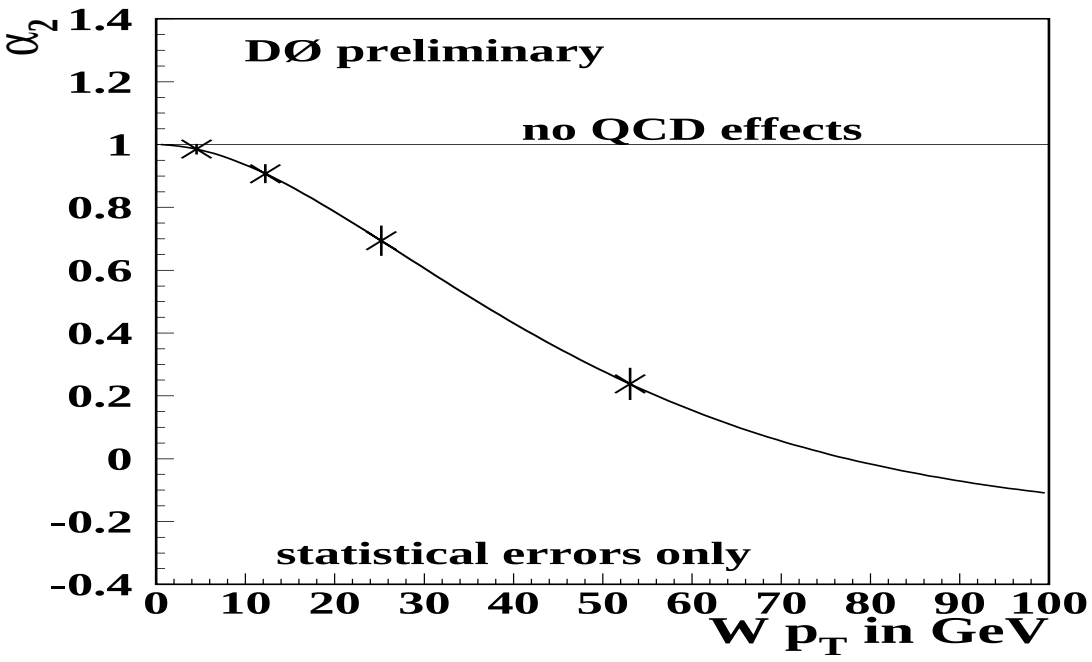

Figure D.1: Estimated sensitivity of α_2 measurement, obtained by scaling statistical errors to Run II conditions.

Since the statistical uncertainties to this measurement become quite small, a further look at systematic errors is necessary. Table D.1 shows a summary of statistical and systematic errors for Run I and Run II. Since the modeling of the hadronic recoil is done from Z data, the error due to the hadronic resolution will up to a point scale with Z statistics. The estimate of this error is done by scaling the number of Z events by a factor of $\sqrt{28.5}$ (the same as for W events but excluding muons). The error on the hadronic response will also improve with

increased Z statistics. Consequently, the largest errors left are the ones due to the QCD multijet background and the electromagnetic scale. It will be of crucial importance for this and other electroweak measurements to better estimate the QCD background. This goal can partially be reached by taking more events with a QCD monitor trigger (as described in section 5.4.3). Of course, it would be best if the QCD background fraction could be reduced even further. At this point it is not obvious to the author how to do this since the current set of electron identification cuts are already very efficient in reducing this background. A Monte Carlo program that correctly models QCD multijet events including a realistic detector model could also help in better estimating the shape of this background. For the low p_T region, the dominant error will be the electromagnetic scale. The author has currently no good estimate by how much this error will be reduced.

D.2 Other Factors

In the current measurement we had to fix α_1 to the value predicted by the QCD calculation since even after summing over both W signs we are slightly sensitive to α_1 due to acceptance effects. Since the central magnet in Run II will allow for sign identification of electrons, α_1 and α_2 could be measured simultaneously eliminating the need for the above assumption for α_1. While this is a nice extension of this measurement, it is not clear at this point by how much it will improve the significance of the measurement of α_2.

In the above estimate of the errors, the binning in p_T^W used for the Run I measurement was kept unchanged. With larger statistics, one would clearly choose a finer binning in p_T^W which would allow for bins with larger mean p_T^W. This would increase the sensitivity in an area where the deviation of the angular distribution due to QCD effects is most pronounced.

The CMS Monte Carlo used in the current analysis treats hadronic jets as

p_T	$0 \leq p_T \leq 10$	$10 \leq p_T \leq 20$	$20 \leq p_T \leq 35$	$35 \leq p_T \leq 200$
mean p_T	5.3	13.3	25.7	52.9
α_2	1.07 ± 0.13	0.82 ± 0.25	0.49 ± 0.37	0.10 ± 0.37
α_2, *predicted*	0.98	0.89	0.68	0.24
stat. errors Run II, e	± 0.024	± 0.047	± 0.069	± 0.069
stat. err. Run II, e+μ	± 0.017	± 0.033	± 0.049	± 0.049
total syst error	± 0.08	± 0.09	± 0.12	± 0.12
error QCD	± 0.02	± 0.05	± 0.09	± 0.07
error QCD shape	± 0.04	± 0.01	± 0.03	± 0.01
error Z	± 0.01	± 0.02	± 0.02	± 0.04
error Z shape	± 0.00	± 0.01	± 0.01	± 0.02
error top	± 0.00	± 0.00	± 0.00	± 0.02
error α_{EM}	± 0.06	± 0.05	± 0.03	± 0.04
error had response	± 0.03	± 0.01	± 0.04	± 0.04
error had. resolution	± 0.02	± 0.02	± 0.04	± 0.05
error had. res. Run II	± 0.004	± 0.004	± 0.008	± 0.009

Table D.1: Central values and statistical errors for α_2 and systematic errors due to backgrounds and the hadronic energy scale and resolution.

point particles and the hadronic recoil is treated as a single jet. This is clearly a simplification of the true processes involved and a real next-to-leading order event generator would be useful.

In addition to the experimental improvements discussed thus far, this measurement will be sensitivity to W production models. These models have to be constrained by independent measurements.

To summarize this discussion, in Run II the measurement of the angular distribution of electrons from W boson decays will be systematically limited. While the recoil response and resolution will improve with increased Z statistics, the estimate of the QCD background fraction and shape becomes a limiting factor. It is not clear at this point by how much the other dominant error, the error due to the uncertainty of the electromagnetic scale, will be reduced in Run II. Other improvements not quantified here are expected from a finer binning in p_T and sign identification of electrons.